POLYTOPIC DIAZINE LIGANDS AND THEIR COORDINATION CHEMISTRY

STEWART R. PARSONS

Polytopic Diazine Ligands and their Coordination Chemistry.

By

Stewart R. Parsons, B. Sc.(Honours)

A thesis submitted to the

School of Graduate Studies

in partial fulfillment of the

requirements for the degree of

Master of Science

Department of Chemistry

Memorial University of Newfoundland

St. John's Newfoundland Canada

Your file Votre référence
ISBN: 0-612-99102-4
Our file Notre référence
ISBN: 0-612-99102-4

Abstract

This thesis describes the ligands and related complexes synthesized in an attempt to generate homonuclear high nuclearity metal clusters from a family of related ligands. Self-assembly processes are the intellectual basis of the work and exploration of the magnetic properties of the complexes the ultimate reason for the research.

Chapter 1 deals with the underlying theoretical and historical principles, it includes a brief introduction to the study of polytopic diazine ligands, and their self-assembly forming clusters. Chapter 1 continues with a discussion of the magnetism of metal clusters, including the different types of magnetic interactions possible and a discussion of molecular magnetism.

Chapter 2 contains general experimental details and background theory on AC/DC SQUID magnetometry and Mössbauer spectroscopy. It briefly discusses the theory of the general ligand syntheses, and continues to specifically describe the preparation of the individual ligands.

Chapter 3 discusses the results of the ligand synthesis, beginning with the general properties they all share and then specific ligand properties. Chapter 3 ends with the discussion of, and experimental details of, a number of ligands whose synthesis were unsuccessful but would have been of interest to obtain.

Chapter 4 deals with the inorganic coordination chemistry of these ligands, identification of the complexes formed and a discussion of their magnetic properties. The magnetic discussion deals with the consequences the structural features of the clusters have on the magnetic properties observed and the structure of the cluster formed. Due to

the paucity of X-ray data, the majority of the structural details of the ligands and complexes are inferred mainly from spectral data.

The Appendices include brief background theory behind the modeling of magnetic exchange behavior in metal clusters (Appendix A), crystal structure data (Appendix B), and χ_M vs. T data (Appendix C).

Acknowledgements

I would like to thank my supervisor Dr. Laurence K. Thompson for the opportunity to perform this research and all of the help he has given me in my association with his research group. I would also like to thank my supervisory committee members, Dr. C. Robert Lucas and Dr. Paris E. Georghiou for help and guidance.

Thanks to Marion Baggs and Dr. Gregory for EI mass spectral data, Linda Windsor for help in running MALDI-TOF mass spectral data, David Miller for crystallographic data workup and Dr. Robert MacDonald for data collection. Thanks also to Dr. William Reiff, for the Mössbauer and ESR data collection and workup.

Thanks again to Dr. Thompson for the funding which made my work with him possible, also thanks to Memorial University School of Graduate Studies, and the Chemistry Department of MUN for their financial support. Much of the equipment used in the course of this research was available due to NSERC instrument grants.

Thanks to the members of the Thompson Research group who I have had the pleasure of working with over the years, including Zhiqiang Xu, Dr. Craig Matthews, Dr. Virginie Niel, Dr. Hilde Grove, Rosemarie Harvey, Louise Dawe, Vicki Milway, Steve DeGrace, Tareque Abedin, Tim Kelly, Liang Zhao, Erik Krupica, and all the others too numerous to mention.

Finally thanks to my wife Crystal, and my parents Sam and Natalie, for their unceasing encouragement and love throughout my entire university career.

Table of Contents

Abstract i

Acknowledgements iii

List of Tables vi

List of Figures vi

List of Schemes xi

List of Ligands xii

List of Abbreviations xiv

Chapter 1. Introduction 1

1.1. Polytopic Diazine Based Ligands 1

1.2. Self-Assembly of Molecular Grids 6

1.3. Large Metallic Assemblies 12

1.4. Magnetism 14

Chapter 2. Experimental 24

2.1. Physical Measurements and General Comments 24

2.1.1. AC/DC SQUID Magnetometry 28

2.1.2. Mössbauer Spectroscopy 30

2.2. Ligand Syntheses 34

2.2.1. Extending Known Ligands 34

2.2.2. Adding "Pockets" Through Doubling the Ligand 35

2.2.3. Spacer Approach to Extending Ligands 38

2.3. Ligand Experimental 42

2.3.1. Linear Ligands 42

2.3.2. Non-Linear Ligands Incorporating Linear Metal-Binding Arrays 47

Chapter 3. Ligand Discussion 49

3.1. General Comments on Ligands 49

3.1.1. Keto-Enol Tautomerization 49

3.1.2. Flexibility of Ligands 50

3.2. Ligand Results and Discussion 51

3.3. Attempted Ligand Synthesis 59

Chapter 4. Complex Synthesis and Discussion 66

4.1. General Comments on Spectral Information 66

4.2. Complex Syntheses 67

4.3. Complex Discussion 70

[(di-OAOP)Ni(H_2O)$_{2.5}$]$_n$ (**1**) 70

[(di-OAOP)Cu_2(BF_4)$_2$(H_2O)$_5$] (**2**) 89

[(Cl2POAP)$_6$Fe(II)$_8$Fe(III)](ClO_4)$_8$·23H_2O (**3**) 93

[(P2OAP)$_4$$Ni_4$]·12$H_2O$ (**4**) 110

Chapter 5. Conclusions 117

Appendix A. Modeling Magnetic Exchange 119

Appendix B. Crystal Structural Data 122

Appendix C. χ_M vs. Temperature Data 124

References 127

List of Tables

Table 1. Selected bond lengths (Å) and angles (°) for **3**.....95

List of Figures

Fig. 1. Basic form of the open chain 1,2-diazine ligands.....1

Fig. 2. POAP showing most common metal binding modes.....2

Fig. 3. Schematic representation of a [2×2] square grid. Note the parallel arrangement of ligands in two groups above and below the metals.....3

Fig. 4. 2POAP as a "doubling" of one of the pyridine moieties of POAP resulting in an additional metal binding pocket.....3

Fig. 5. Ligand 3,6-bis-6-methyl-(2-pyridyl)pyridazine.....4

Fig. 6. Ligand 6,6'-bis[2-(6-methylpyridyl)]-3,3'-bipyridazine.....4

Fig. 7. [3×3] grid using the 6,6'-bis[2-(6-methylpyridyl)]-3,3'-bipyridazine ligand and Ag.....4

Fig. 8. An example of a three-stranded trinuclear helicate.....10

Fig. 9. Cl2POAP[70] showing metal-binding mode, emphasizing five-membered rings.....11

Fig. 10. The possible metal-binding modes of the ligand 2PAOP. A non-linear array of metals would occur, caused by incorporation of two adjacent six-membered rings.11

Fig. 11. 2-hydroxypyridine derivatives, showing their variety of potential binding modes.....12

Fig. 12. $Co_{24}(\mu_3\text{-}OH)_{14}(\mu_2\text{-}OH)_4(\mu_3\text{-}OMe)_2(\mu_3\text{-}Cl)_2(mph)_{22}$.....13

Fig. 13. Induced magnetization in a paramagnet.....17

Fig. 14. Induced magnetization in a molecular magnet..... 17

Fig. 15. A typical hysteresis curve showing the coercive field and remnant magnetization. 19

Fig. 16. The first SMM $[Mn_{12}O_{12}(MeCO_2)_{16}(H_2O)_4]\cdot 2MeCO_2H\cdot 4H_2O$ (Large circles represent Mn cations, small circles represent O). 20

Fig. 17. Transitions between energy states in a Mössbauer experiment. 31

Fig. 18. Diagrammatic representation of a Mössbauer experiment. When resonance occurs photons are detected at No. 2 and fewer at No. 1 as some of the radiation is absorbed. 32

Fig. 19. General Schiff-base-type linkage scheme..... 34

Fig. 20. Comparison of POAP (showing metal binding modes) and the general ligand form..... 35

Fig. 21. Tritopic coordination mode for 2POAP. Note the ligand symmetry. 36

Fig. 22. Some structural isomers of [2×2] grids based on POAP. 36

Fig. 23. Extended derivative of POAP through incorporation of a spacer into the ligand's design. 38

Fig. 24. Extended POAP-type ligand showing possible coordination mode in a grid. 40

Fig. 25. Crystal structure of $(POAP\text{-}H)_4Fe_2Ni_2(NO_3)_6\cdot CH_3OH\cdot 5H_2O$; additional solvent molecules and nitrate anions are bound to the iron centres. 41

Fig. 26. Tautomerization in diazine-based ligands. 49

Fig. 27. Conformational flexibility of diazine-based ligands. 50

Fig. 28. Comparison of P2OAP ligand's grid-type binding mode with that of the ideal case for grid formation. 52

Fig. 29. Crystal structure of picolinic hydrazide methyl pyruvate adduct. 53

Fig. 30. Potential metal binding modes of 2POAN, emphasizing chelate ring size formed on coordination of metal cations. 54

Fig. 31. 2POAO showing potential metal binding modes and potential bridging of terminal primary alcohol moieties. 55

Fig. 32. Portion of di-OAOP ligand showing possible metal binding pockets, emphasizing the size of chelate rings formed, potential bridging of the phenolic oxygen and incomplete coordination sphere of one bound metal. 57

Fig. 33. The ligand 2PAOP and Sakamoto's ligand showing potential metal binding sites. 58

Fig. 34. A potential [4×4] grid-forming ligand showing potential metal binding modes. 59

Fig. 35. 2PzOAP showing potential metal binding mode. 61

Fig. 36. μ (μ_{BM}) vs. Temperature (K) for **1**. (DC Field = 0.1T) 71

Fig. 37. **1** Polymeric Chains. 72

Fig. 38. Stacking of polymeric nickel chains in **1** forming 2D sheets along the directions indicated. 73

Fig. 39. Schematic representation of the coupling interaction of the zigzag double chain of $Ni(OH)(NO_3)H_2O$. 74

Fig. 40. Antiferromagnetic coupling of 2D sheets with ferromagnetic coupling between chains within a sheet. 76

Fig. 41. Variable temperature data (μ) at low temperatures as a function of external field. 77

Fig. 42. Magnetization data at low temperature as a function of external field. 78

Fig. 43. Hysteresis of the magnetization for **1** measured at 2 K. 79

Fig. 44. AC susceptibility of **1** (DC field = 0 T, Amplitude = 3.5 Oe, Frequency = 100 Hz). 80

Fig. 45. Cooling under zero-field conditions and 100 Oe. 81

Fig. 46. Magnetization vs. field for **1** at 2 K. 82

Fig. 47. Magnetization vs. field for **1** at 2 K in the low field region. 83

Fig. 48. $\delta M/\delta H$ vs. Field (Oe) at 2 K for **1**. 84

Fig. 49. Variable temperature data for **1** to T = 35 K. The solid line represents the best fit. 86

Fig. 50. Variable temperature data for **1** to T = 16 K. Note the deviation of the experimental data from the theoretical data. 87

Fig. 51. Proposed structure of **2**. 90

Fig. 52. Magnetic profile of **2** (H = 1000 Oe). 92

Fig. 53. Crystal structure of **3**. 94

Fig. 54. [Fe_9 (μ-O)$_{12}$] core structure of **3**. 94

Fig. 55. Iron-alkoxo moiety of a single molecule seen along the xy-plane of **3**, illustrating ring "puckering". 97

Fig. 56. Layers of grid molecules (core shown only) stacked in the 'z' direction. 98

Fig. 57. Points of close contact between adjacent grids of a single layer of **3**. 99

Fig. 58. Points of close contact between adjacent grids of **3**. 100

Fig. 59. Mössbauer spectra of **3** at 293 K. 101

Fig. 60. Mössbauer spectra of **3** at 77.3 K. 102

Fig. 61. Mössbauer spectra for **3** at 77.3, 14.5, 10.0, 8.5, and 4.2K. 103

Fig. 62. X-Band ESR spectrum of **3** taken at 300 K. 104

Fig. 63. Variable temperature magnetic profile of **3** (H = 0.1T). 106

Fig. 64. Electronic configuration of Fe(II) and Fe(III) 107

Fig. 65. Magnetization vs. Field for **3** at 10 K. 108

Fig. 66. Magnetization vs. Field for **3** at 2 K. 109

Fig. 67. Schematic of a fully occupied molecular "pin-wheel", metal-ligand moiety only. 111

Fig. 68. Synthesis of and structure of $[(POAP)Fe(III)(NO_3)_2(H_2O)_2]$. 112

Fig. 69. Proposed structure of 4 showing Ni(II) binding mode of P2OAP. 113

Fig. 70. Variable temperature magnetic data for **4**. The solid line represents the best fit data to the parameters given in the text. 113

Fig. 71. Electron configurations of octahedral and square planar d^8 cations. 114

Fig. 72. Exchange diagram for **4**. 115

List of Schemes

Scheme 1. Synthesis of P2OAP. 42

Scheme 2. Synthesis of POMeO. 44

Scheme 3. Synthesis of 2POAN 45

Scheme 4. Synthesis of 2POAO. 46

Scheme 5. Synthesis of di-OAOP. 47

Scheme 6. Synthesis of 2PAOP. 48

Scheme 7. Attempted synthesis of potential [4×4] grid forming ligand. 60

Scheme 8. Attempted synthesis of 2PzOAP. 63

List of Ligands

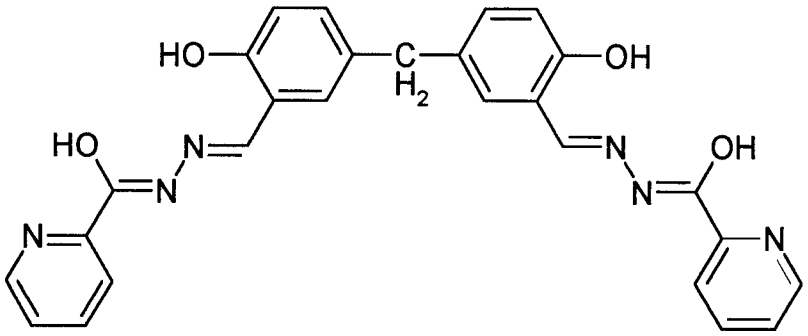

di-OAOP

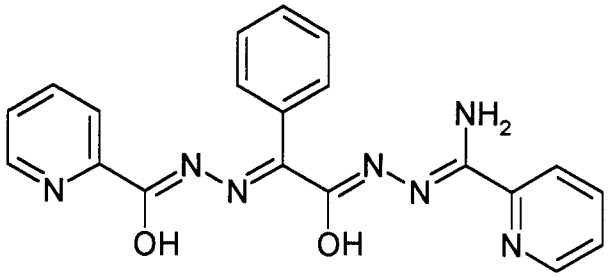

P2OAP

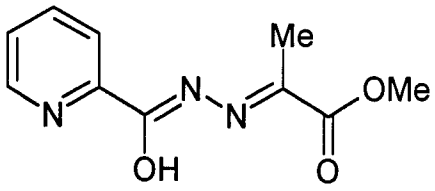

POMeO

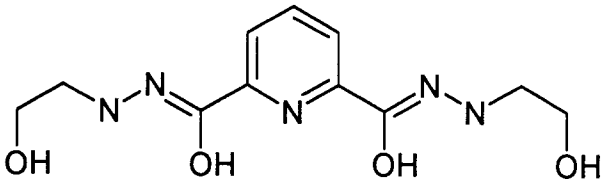

2POAO

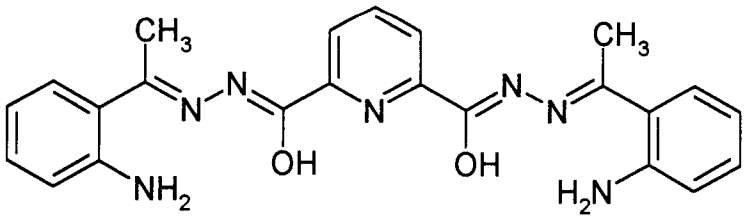

2POAN

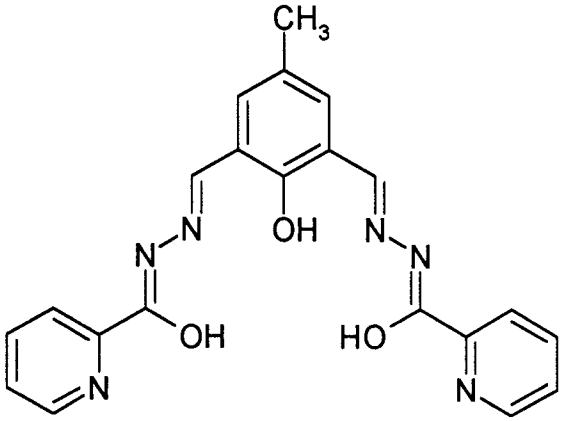

2PAOP

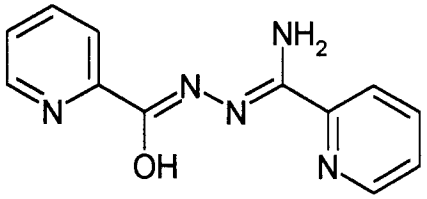

POAP

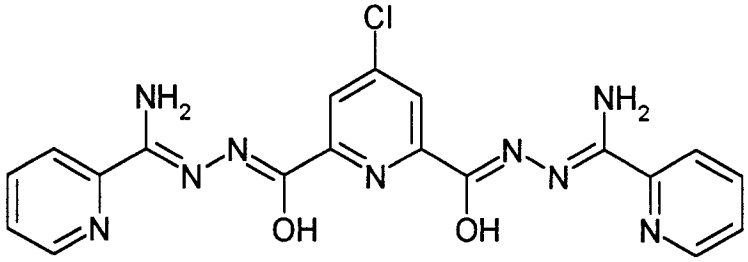

Cl2POAP

List of Abbreviations

B	Bulk magnetic dipole
ESR	Electron spin resonance
ES-MS	Electrospray mass spectrometry
g	Landé splitting factor
H	External magnetic field
H_{ex}	Hamiltonian
H_C	Coercive field
I	Intensity of the magnetization
J	Exchange integral
k	Boltzman constant
M	Molar magnetization
N	Avagadro's number
P	Magnetic permeability
R	Residual factor
S	Cluster spin quantum number
s	Local spin quantum number
STM	Scanning tunneling microscopy
SQUID	Superconducting quantum interference device
T_C	Critical temperature
α	N-N torsional angle in diazine based ligands
β	Electronic Bohr magneton

β/β'	C-N-N bending angle in diazine based ligands
ΔE_Q	Quadrupole splitting
μ	Magnetic moment
μ_{SO}	Spin-only magnetic moment
μ_B	Bohr magneton
μ''	Out-of-phase moment component
θ	Curie-Weiss or Weiss-like correction factor
Ψ	Heitler-London wavefunction
ρ	Fractional paramagnetic impurity
κ	Magnetic susceptibility per unit volume
$\omega(S')$	Degeneracy of spin state S'
χ	Magnetic susceptibility
χ_{2D}	2D sheet susceptibility
χ_{FC}	Ferromagnetic chain susceptibility
χ_g	Gram susceptibility
χ_m	Molar susceptibility
χ''	Out-of-phase susceptibility component

Chapter 1. Introduction

1.1. Polytopic Diazine Based Ligands

Heteroatom bridging ligands containing hydrazide linkages which are capable of binding two metals per ligand have been extensively investigated.[1-4] Generally, these are of the basic type shown in Fig. 1, in which X and X' can be a number of groups such as NH_2, OH, SH and others, and the R and R' groups are most commonly pyridine or pyrazine rings. In contrast to heterocyclic ring systems, in which the diazine (N-N) moiety is rigidly fixed,[5] in open-chain systems the N-N single bond is not constrained by a ring and is free to rotate.

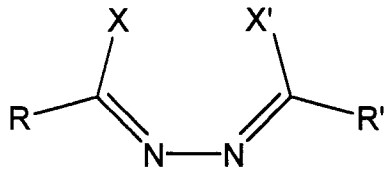

Fig. 1. Basic form of the open chain 1,2-diazine ligands.

With rotation possible about the N-N bond and a variety of donor groups depending on the identities of R/R' and X/X', the coordinative possibilities are wide as this family of ligands has a number of possible coordination modes[6] including several mono- and di-nucleating coordination modes.[7-11] Ligands in this group have been found to form mononuclear,[11-14] dinuclear,[15] trinuclear[16] and tetranuclear[17] complexes, for instance with copper(II), although they are also able to complex a large range of transition metals.

Interestingly, there is a linear relationship between the exchange integral (J) in the Hamiltonian expression (for instance for a $Cu(II)_2$ dimer $H_{ex} = -2JS_1 \cdot S_2$) and the rotation

angle of the N-N bond, when the diazine moiety is acting as a bridge. Over a 105° range, ferromagnetic coupling is observed at angles < 80°, and antiferromagnetic coupling at angles > 80°.[18,19,20] This only serves to demonstrate the wide variety of coordination modes and interactions available to this type of ligand.

One such ditopic ligand is POAP in which X is a hydroxy group, X' a primary amine, and R and R' are both pyridine rings (see Fig. 2). POAP is well known for its ability to form a variety of complexes, most commonly with the metals arranged in a square tetranuclear orientation[3] (see Fig. 3) although trigonal bipyramidal[21] and rectangular tetranuclear[3] configurations have been reported as well. Generally the coordination to metals is of the type shown in Fig. 2, with bridging occurring through the oxygen rather than through the N-N diazine moiety itself.

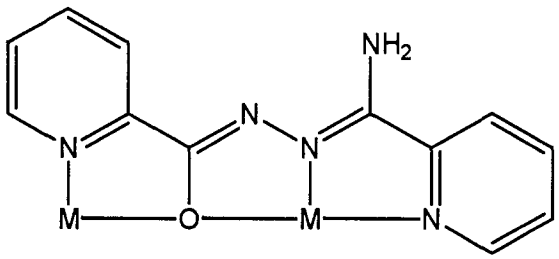

Fig. 2. POAP showing most common metal binding modes.

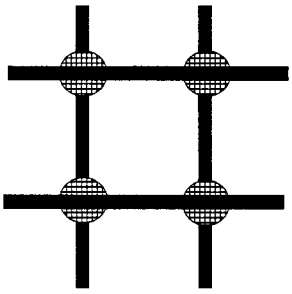

Fig. 3. Schematic representation of a [2×2] square grid. Note the parallel arrangement of ligands in two groups above and below the metals.

From the development of the ligand 2POAP, it has been demonstrated that the size of the grid can be extended from a [2×2] square grid to [3×3] square grid through the systematic addition of a third metal binding pocket in the contiguous array of metal binding sites.[22] This extension was accomplished through the incorporation of a central 2,6-disubstituted pyridine in place of the monosubstituted picolinic group. Thus, repeating the structure of the normal POAP ligand about this pyridine moiety leads to the tritopic symmetrical ligand 2POAP pictured in Fig. 4, capable of forming [3×3] grids.[22,23]

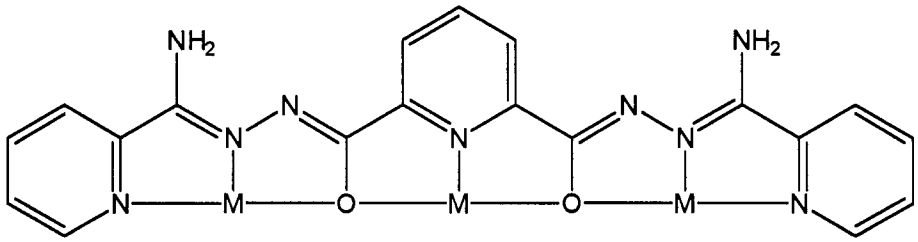

Fig. 4. 2POAP as a "doubling" of one of the pyridine moieties of POAP resulting in an additional metal binding pocket.

The work of Jean-Marie Lehn[24] has also demonstrated the possibility of accessing larger grids through designing rigid linear *n*-topic ligands capable of forming an [*n*×*n*]

grid based on n^2 tetrahedrally-coordinated metal ions, such as Ag, and $2n$ ligands. The ligand 3,6-bis(2-pyridyl)pyridazine, a di-topic ligand, was found to form [2×2] square grids while extending the ligand to the tri-topic 6,6'-bis[2-(6-methylpyridyl)]-3,3'-bipyridazine allowed the formation of [3×3] square grids (see Fig. 5, Fig. 6 and Fig. 7).

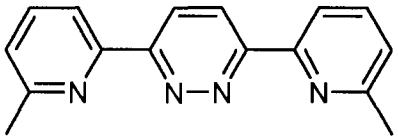

Fig. 5. Ligand 3,6-bis-6-methyl-(2-pyridyl)pyridazine.

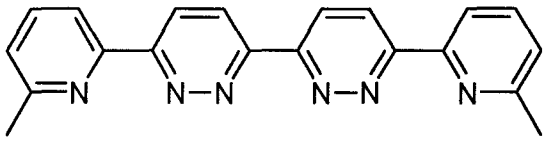

Fig. 6. Ligand 6,6'-bis[2-(6-methylpyridyl)]-3,3'-bipyridazine.

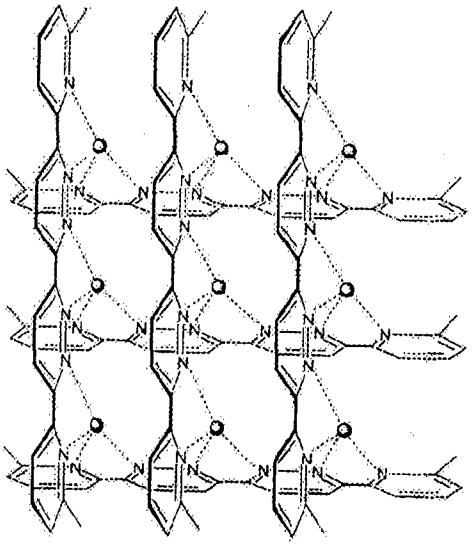

Fig. 7. [3×3] grid using the 6,6'-bis[2-(6-methylpyridyl)]-3,3'-bipyridazine ligand and Ag.

A [4×4] grid (identified using NMR and ES-MS techniques[25]) has also been synthesized using a ligand designed from a similar approach with four metal-binding pockets and Pb.

These ligands are similar to the polytopic diazine-based ligands of this work, differing however in that they are closed-chain 1,2-diazine based-ligands, the 1,2-diazine moiety being part of a pyridazine group. The closed-chain nature of this group has the result of limiting the conformational flexibility of the ligand as rotation about the N-N bond is not possible, reducing the number of conformational degrees of freedom. On the other hand, this lack of flexibility ensures that the ligands are in the correct conformation for the ligand to bind a metal cation as they would need to, in order to form a molecular grid.

1.2. Self-Assembly of Molecular Grids[26]

Self-assembly reactions are useful tools for the synthesis of supramolecular materials, and the design of ligands incorporating specific information in the form of appropriately placed coordination pockets can lead to single high nuclearity complexes in high yield. Arranging the pockets in the form of a contiguous linear array will often lead to the formation of molecular grids, with the possibility of significant magnetic exchange between adjacent paramagnetic metal centres if an appropriate bridging group is incorporated between the metal binding pockets.

The spontaneous formation of organized molecular architectures utilizing the self-assembly of ligands with metal cations involves a variety of processes. These processes include the successive molecular recognition processes between the various components, which are the interactions that cause the high degree of selectivity observed in self-assembly processes. This selectivity depends on the stereoelectronic molecular information, or intrinsic information, encoded in the components, and the external conditions under which the reading, recognition and the expression of this information in the final supramolecular structure occurs.

Thus, the formation of the final structure occurs as a result of specific interactions between the covalent organic ligand strands and the metal ions. Metal cations are systematically used since they offer a variety of properties, such as (i) coordination geometries and stereochemical preferences depending on their size, charge and electronic structure, as well as (ii) a variety of binding strength and kinetic stability, and (iii) different binding affinities for different binding units expressed in the ligand. Therefore

the final magnetic and spectroscopic properties observed in the product will depend on the choice of metals. The choice of metal ion should be made such that its intrinsic information closely matches the binding possibilities of the organic ligand to ensure the assemblies give predictable and well-defined products. The use of organic synthesis methods allows a wide variety of organic strands to be prepared so therefore there is an almost unlimited capacity to produce ligands with suitable and complementary information.

A number of concepts have arisen from the study of the self-assembly of molecular species. Among these are: (a) Molecular recognition, involving the selective interaction of two or more components of the system; (b) Self-organization involving the system's ability to spontaneously generate well-defined supramolecular architectures from the complementary components under a given set of conditions; (c) Self-assembly, which corresponds to a single step of the self-organization procedure and; (d) Supramolecular programming, which involves the design of ligands with certain structural information which is intended to complement the coordination requirements of the metal cations. In this way, the controlled formation of complex molecular geometries can occur through addition of a suitably designed ligand and the corresponding metal cation. Self-assembly processes, therefore, arise from the processing of information built into the organic ligands by the algorithm of the structural and electronic coordination preferences of the metal cations.[26] Through the careful choice of conditions and through the design of the ligand, the ultimate geometry of the cluster can be influenced or even controlled.

Since self-assembly processes involve mixing the precursors to the complex, the ligands and metal cations, and allowing the interactions between ligand and metal cations to assemble the final complex in a highly selective, high yielding reaction, they are of great interest since large complex structures may be formed from relatively simple precursors in a single experimental step, without a large degree of outside manipulation.

The recognition processes between metal cation and ligand are impressive in their scope, involving the organization of a large number of components towards the formation of a single structure. For instance, in the case of the formation of a [3×3] grid the combination of six ligands and nine metal cations involves the formation of 54 new bonds between 15 components in one concerted interaction. Some systems have demonstrated recognition of molecular components to the degree of being able to differentiate between two similar closely related ligands. For instance, Lehn[27] has reported a system which shows a preferential assembly of [2×3] rectangular grids in 90% yield in a solution consisting of a suitable metal cation and a mixture of di- and tritopic ligands. The formation of separate [2×2] and [3×3] grids only occurred with 8% and 2% yield respectively, as determined by NMR. Had there been no special recognition processes and therefore no preference for products of one configuration over another, the statistical distribution of products would be 48% [2×3], 36% [2×2], and 16% [3×3].

The formation of [3×3] grids which display interesting magnetic properties is still relatively rare, especially when considered next to the wealth of [2×2] M_4 square grids described in the literature.[3,28-41] Note that while complexes with square arrangements

of metals can be considered as [2×2] grids, they and their magnetism are quite well studied.[42]

In a molecular grid, for instance a [3×3],[22,23] the nine metals form an approximate plane. Each ligand is parallel to others in the group, with spacings of about 3.5-4.0 Å, but the two groups of ligands are perpendicular to each other. The metal cations composing the grid occupy three different coordination environments, depending on whether they occupy the corner, apical, or central coordination pocket provided by the ligands (Fig. 4).

In order to promote the formation of grid-type complexes the ligands involved must have certain features which predispose them to adopt the conformation which they will have in a grid complex.

In a grid complex the ligands line up roughly parallel to each other, and so the ligands must incorporate this feature in their design in order to allow them to align in a linear parallel fashion. The presence of three aromatic rings in highly conjugated ligands like 2POAP would allow for significant π-stacking, which is considered to be an important driving force for these ligands to align parallel to one another. In cases in which the interactions responsible for the parallel orientation of the ligands are weak or non-existent, and the ligand has the flexibility to form a helix, the competing reaction is often the formation of a helicate.[43] A helicate is a discrete supramolecular complex constituted by one or more covalent strands wrapped about and coordinated to a series of at least two ions which define the helical axis (see Fig. 8).

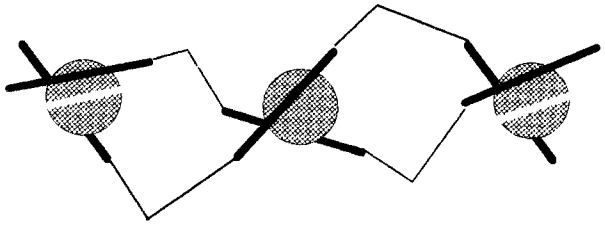

Fig. 8. An example of a three-stranded trinuclear helicate.

In order to form a [3×3] grid consisting of nine octahedrally-coordinated metals and six ligands, the ligand should possess three "pockets" each of which contains three metal binding groups, in order that the coordination requirements of the metals are completely satisfied. The greater the match between the required binding geometry and hardness/softness of the metals and the available donors offered, the greater the tendency towards the formation of the intended cluster.

In order to encourage effective communication of the spin states of the adjacent metals, an appropriate group capable of mediating orbital overlap should bridge the metals. Oxygen is a very useful bridge as it readily complexes a wide variety of metals and is well known to form bridges between metals. Although this is not a general requirement of grid formation, we are interested in the formation of magnetically interesting grids, and therefore this feature must be considered.

The metallic grid is roughly planar and the metals are in a linear arrangement, although there is usually some "puckering" of the plane described by the metals. In order for the ligand to accommodate this it must form an array series of five-membered chelate rings on coordination to the metals (see Fig. 9) thus encouraging the metals to bind in a roughly linear contiguous array. Formation of other size rings, for instance six-

membered rings, will result in a non-linear array. For instance in Fig. 10, the presence of two six-membered rings results in an array of rings which will cause a "bend" in the array of metals. Smaller rings than 5-membered and larger than 6-membered will be strained and not have as strong a binding interaction as the five-membered ring case.

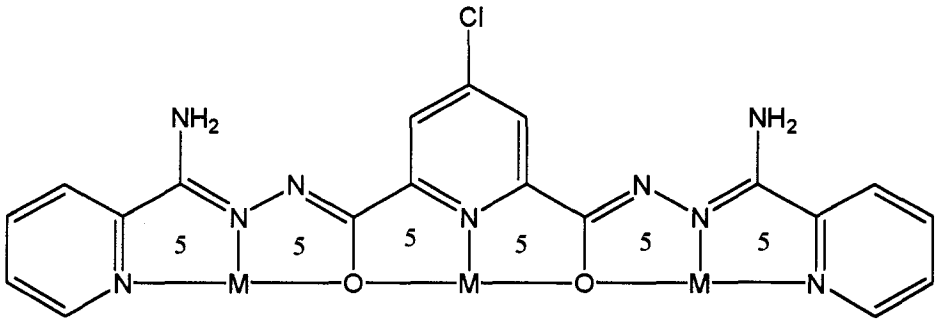

Fig. 9. Cl2POAP[70] showing metal-binding mode, emphasizing five-membered rings.

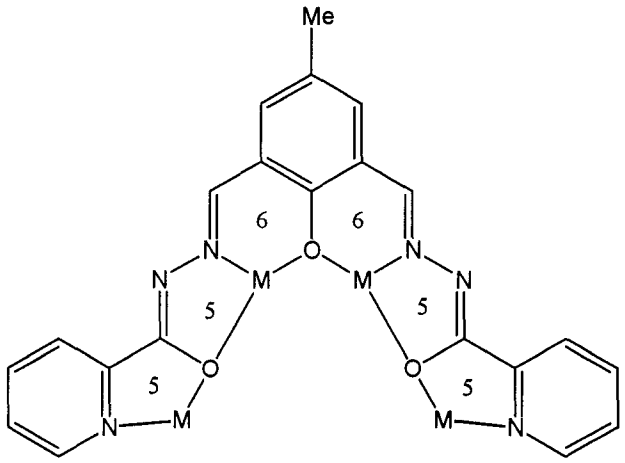

Fig. 10. The possible metal-binding modes of the ligand 2PAOP. A non-linear array of metals would occur, caused by incorporation of two adjacent six-membered rings.

1.3. Large Metal Assemblies

In contrast to the use of polyfunctional, polytopic ligands with well-defined coordination pockets, another common approach takes advantage of the desire of metal ions under the correct conditions to assemble into a cluster. This occurs readily with simple bidentate ligands which, while not fully satisfying the coordination requirements of a single metal cause the metal to fill its vacant coordination sites through using spare donor fragments from a neighboring subunit as the overall cluster forms.

Parsons and Winpenny[44] have worked in this area using derivatives of 2-pyridone, 2-hydroxypyridine (see Fig. 11) and moderate oxidation state metals such as copper and chromium to form clusters involving as many as 24 metal cations, for instance with the ligand mph in which the R group of the ligand below is Cl (see Fig. 12).

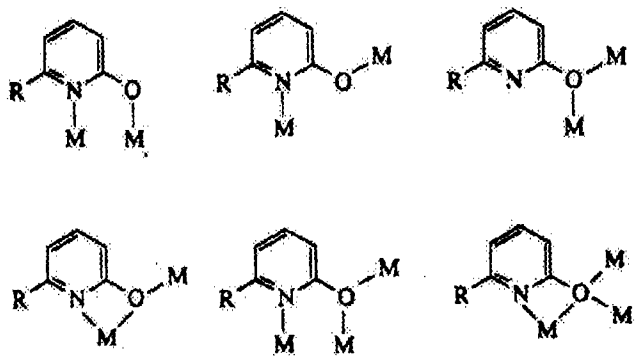

Fig. 11. 2-hydroxypyridine derivatives, showing their variety of potential binding modes.

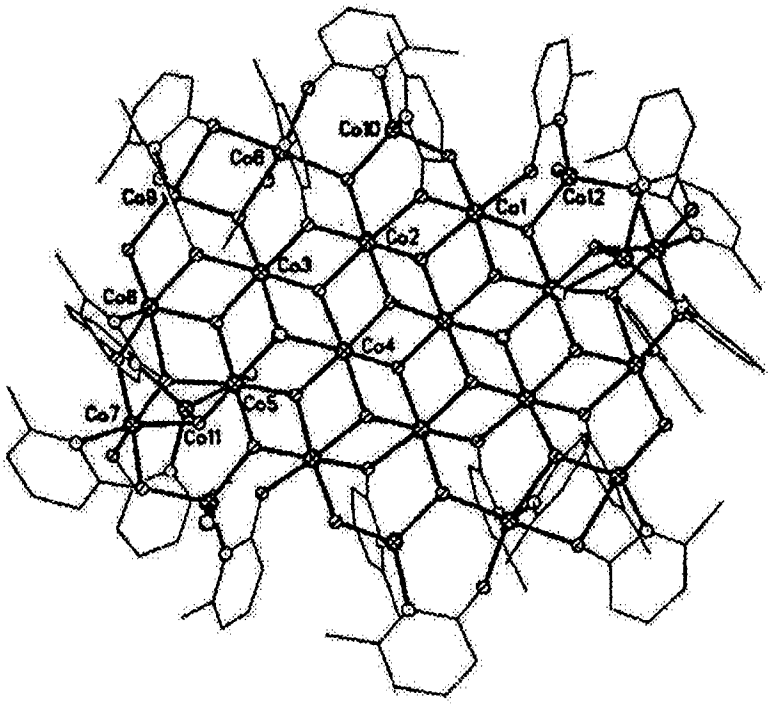

Fig. 12. $Co_{24}(\mu_3\text{-}OH)_{14}(\mu_2\text{-}OH)_4(\mu_3\text{-}OMe)_2(\mu_3\text{-}Cl)_2(mph)_{22}$.

The formation of carboxylate clusters of manganese using these techniques has also been well studied[45] and large clusters of as many as 154 manganese cations have been synthesized.[46] There is a subtle balance of the coordination algorithms of the metals and the encoded molecular information in the form of the coordination environments offered by the ligands. This balance leads to the formation of molecular cluster species rather than polymeric entities.

In principle the use of pre-designed polytopic, polyfunctional ligands with well-defined and appropriately separated coordination pockets may have a better chance of control over the outcome of a self-assembly process to produce a cluster with a predefined nuclearity.

1.4. Magnetism

All substances possess magnetic properties by virtue of their having electrons. In an external magnetic field, H, the magnetic field inside a material will differ from the external field. This magnetic induction, B, is the density of the magnetic lines of force within the material and is related to H by the following[47]:

$$B = H + \Delta H \quad (1)$$

$$B = H + 4\pi I \quad (2)$$

$$P = 1 + 4\pi\kappa \quad (3)$$

In these equations ΔH is the difference between the external and internal fields, I is the intensity of the magnetization of the substance, or magnetic moment per unit volume, P is the magnetic permeability of the substance and κ is the magnetic susceptibility per unit volume. Magnetic susceptibility is more conveniently expressed in terms of gram (χ_g) or molar (χ_m) susceptibility, as it is easier to determine the mass and/or number of moles of a sample than to measure its volume. These properties are related through the following equations:

$$\chi_g = \kappa/d \quad (4)$$

$$\chi_m = \chi_g M \quad (5)$$

where d is the density of the material and M is its molar mass.

There are two possible situations since the magnetic permeability may be either positive or negative. If $P < 1$ then $\kappa < 0$ and $\chi < 0$. In this case the magnetic flux inside the material is opposite to that of the applied field and the sample will be repelled by the

external field. This phenomenon, a property of paired electron spin, is called diamagnetism and is present in all materials. This diamagnetic contribution to the overall susceptibility must be corrected in magnetic investigations, most commonly by using diamagnetic susceptibility constants which account for the diamagnetism introduced. Should $P > 1$ then $\kappa > 0$ and $\chi > 0$. In this case the magnetic flux inside the material is aligned with the external magnetic field and the material is attracted by the field. This is a property inherent to unpaired electrons and is known as paramagnetism.

Paramagnetism can be subdivided into two further types of magnetism depending on how adjacent paramagnetic centers interact with one another. Systems which show this interaction of adjacent paramagnetic centers are known as magnetically concentrated systems, as opposed to magnetically dilute systems which do not show this behavior. Coupling of adjacent paramagnetic centers will lead to either ferromagnetism or antiferromagnetism. In ferromagnetic systems, the individual paramagnetic moments align in parallel with one another forming magnetic domains which increase the bulk paramagnetism observed. In these systems $P >> 1$ and χ_g is much greater than that for an uncoupled paramagnet. In addition this interaction varies with both applied field and temperature, resulting in a variation of χ_g with temperature and applied field. In antiferromagnetically coupled-systems the individual paramagnetic moments pair, aligning antiparallel with one another thus removing the net paramagnetism of the pair. This causes χ_g to be lowered, with the system approaching diamagnetism in strongly coupled systems. This type of coupling is independent of the applied field strength but is temperature dependent. For antiferromagnetic systems, χ_g is therefore field-independent

but varies with temperature. Coupling between paramagnetic centers can occur intramolecularly, such as between adjacent paramagnetic metals in clusters, or intermolecular between adjacent molecules, transmitted through the crystal lattice.

In addition, a third type of collective magnetic interaction is ferrimagnetism, in which net magnetic ordering occurs. This ordering, however, differs from ferromagnetism in that ions of differing moments are present and though they order with opposed spins (i.e. antiferromagnetically) because of the different magnitude of the individual spin moments, there is incomplete cancellation and a residual moment remains.

Finally, metamagnetism combines antiferromagnetic and ferromagnetic interactions. This type of behavior can be identified by taking advantage of the field independence of the antiferromagnetic coupling. By altering the field, the intensity of what may initially appear to be solely antiferromagnetic coupling will be altered as the ferromagnetic component is affected. This allows the system to be identified as a metamagnet since normally antiferromagnetic coupling will have no field dependence.

Molecular magnetism is a term used to describe systems which are molecular in nature yet show magnetic properties similar to those of bulk magnets. These properties include a spontaneous magnetization below a certain temperature characteristic to the compound and a hysteresis effect in the magnetization. The property of having a hysteresis of the magnetization has come to be the defining feature of a molecular magnet. The first two examples of this type of compound were reported in 1986.[48,49]

In a "normal" paramagnet when an external magnetic field, H, is applied, a bulk magnetic dipole, B, is induced in the material as the external field causes molecular dipoles to align parallel to the external field. When the external magnetic field is removed, the induced field quickly dissipates as the molecular dipoles randomize and cancel out the bulk moment (Fig. 13).

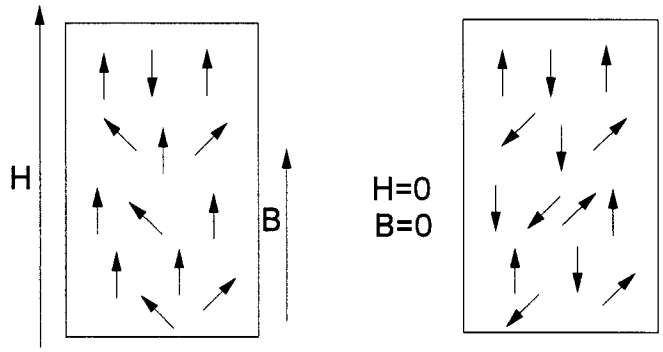

Fig. 13. Induced magnetization in a paramagnet.

In a molecular magnet when the external field is removed it responds similarly to a bulk magnet, when the external field is applied an induced field forms in the material, and as the external field is removed the induced field remains (see Fig. 14).

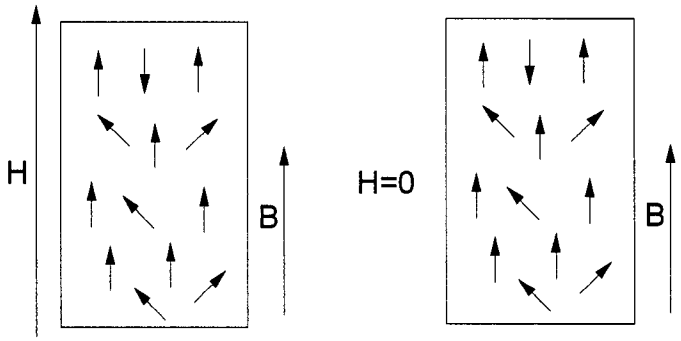

Fig. 14. Induced magnetization in a molecular magnet.

There are a number of parameters which are used to describe the hysteretic profile of the molecular magnet. The remnant magnetization is the strength of the remaining induced field when the external field has been removed. The coercive field is the strength of the external field which must be applied opposite to the induced field in order to force the magnetization to return to zero, overcoming the energy barrier to the reorganization of the molecules dipoles. A final parameter is the critical temperature T_c, the temperature below which the compound in question displays the properties of a molecular magnet, i.e. a hysteresis of the magnetization. In order to obtain a commercially-useful system, T_c should be as high as possible, near room temperature, in order to avoid the need to use cryogenic techniques to achieve the temperatures at which these systems are magnets. Promising work has been done using systems similar to the Prussian-blue phases in obtaining room temperature molecule based magnets, although final structural characterization has proven difficult due to inherent difficulty in characterizing the structure of the phases.[50]

In cases where the hysteretic effect is used to store information, as in magnetic recording media, the remnant magnetization can be thought of as the strength of the stored signal, the larger the remnant magnetization the more easily a domain with a "bit" of information is distinguished from a domain which is not encoded, or from detector noise. The coercive field represents the resistance of the stored signal to erasure, either accidental or intentional. In order to be useful for storing information, these should both be large such that the stored data is easily read as well as stable.

A typical hysteresis curve is shown in Fig. 15 indicating the remnant magnetization and coercive field values.

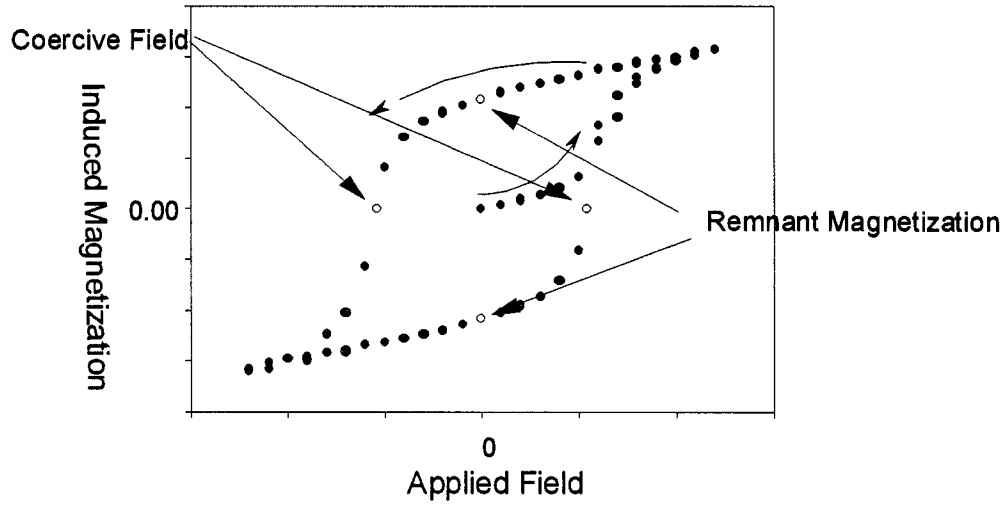

Fig. 15. A typical hysteresis curve showing the coercive field and remnant magnetization.

There are three situations for molecular magnets which arise as a result of the degree of cooperativity between adjacent magnetic dipoles. In the first case the molecules are electrically neutral and there is little interaction between them. That is, they are independent of one another and have only weak van der Waals interactions between molecules. In the second case the molecules are charged and insulated from one another by counteranions, and again there are only weak interactions. In the third case the molecules have strong interactions between them. This is achieved by direct bonding either covalently or hydrogen bonding interactions, or through-space magnetic exchange such as strong coupling of magnetic dipoles in adjacent molecules.

In the first two cases these materials are often called single molecule magnets, since the lack of intermolecular magnetic cooperativity means that the bulk magnetic

properties observed are a result of molecular properties alone. The hysteresis observed is a result of hysteresis of the magnetization at a molecular level and quantum effects are observed in the bulk magnetization.

The first single-molecule magnet (SMM) identified was a manganese carboxylate cluster, $[Mn_{12}O_{12}(MeCO_2)_{16}(H_2O)_4]\cdot 2MeCO_2H\cdot 4H_2O$, synthesized by Gatteschi *et. al.* in 1991[51] (Fig. 16). After a magnetic field was applied at 2 K, two months later the magnetization was still 40% of the saturation value, clearly showing a memory effect.

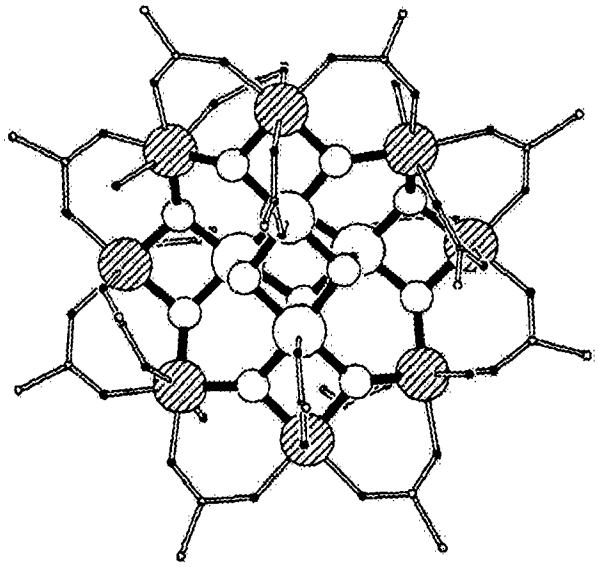

Fig. 16. The first SMM $[Mn_{12}O_{12}(MeCO_2)_{16}(H_2O)_4]\cdot 2MeCO_2H\cdot 4H_2O$ (Large circles represent Mn cations, small circles represent O).

The individual molecules of single molecule magnets are the sole source of the bulk hysteresis, involving no cooperative effects between molecules. Therefore the individual metal clusters show the same magnetic properties as the bulk compound. Consequently, the observed hysteresis effect is observable in the individual molecules

which make up the material. Thus it should be theoretically possible to store information on a single molecule, giving storage media with an incredible information density. There is also the potential to allow tuning of these materials' magnetic properties, through altering the structure of the ligands involved and through this the interaction of these ligands with the metals, as well as the interactions between the metals.

The technology currently exists in the field of scanning tunneling electron microscopy (STM) to observe and address individual molecules on a surface, and it has been demonstrated that controlled deposition and removal of molecular grids on surfaces is possible using these quite simple techniques.[52] Therefore, the basic technology of the single molecule memory storage device appears to be attainable, and developing a promising system to test the technology should allow further investigations in this area.

Another interesting consequence of the molecular origin of the hysteresis in single molecule magnets is that there are clear quantum effects observed in the bulk magnetization. These take the form of a stepped magnetization, rather than the smooth curve seen in "normal" magnetic systems. The existing techniques used to explore bulk magnetic effects can therefore be used to observe the quantum effects of the magnetization of single molecules without any modifications for these systems. These systems can therefore be used to investigate quantum effects using the well-developed and simple macroscopic techniques available to the magnetochemist. In principle, these quantum effects could also be used to develop new classes of computers in which quantum coherence is used to store and process information by taking advantage of the different stable quantum states which can be induced with an applied field. Quantum

coherence is a term used to describe systems which are able to exist in more than one state simultaneously (superposition). Until a measurement is made the system is coherent and all possibilities are both true and false. Once a measurement is made, the wave function collapses and the state is determined. Any interaction can be considered a measurement, which is why coherence is such a delicate property to maintain.

To design molecular magnets, a number of features should be included in the final structure of the compound. One should attempt to obtain the largest possible total spin in the ground state, and in order to attain this one should seek to design metal clusters with as many magnetically interacting metals as possible, as well as having primarily ferromagnetic interactions between them. The cluster should have a highly populated magnetic ground state at relatively high temperatures, in order that these magnetic properties will be appreciable and observable at higher temperatures. Finally, the cluster should display a strong anisotropy of the magnetic ground state. This anisotropy is the source of the hysteresis effect, an energy barrier to the reorganization of the magnetic dipoles of the component molecules, and arises from the axial zero-field splitting of the metal ion, e.g. Mn, and should be negative.

The synthesis of large molecular grids presents a potential route to developing materials which may behave as molecular magnets, and perhaps even single molecule magnets. In molecular grids, the metals can be quite close together and may have strong magnetic interactions between adjacent metals depending on ligand design. This fulfills one requirement which gives the potential for molecular magnetic behavior to arise.

Another reason for the choice of metal grids to probe this area is that the properties of the ligands which encourage grid formation appear to hold as the targeted grid size is increased. This is a quality which is not seen in the formation of large clusters using coordinatively flexible ligands, since the interactions between the components of the system are too subtle to be predicted and designing ligands to form large clusters with a predetermined geometry is not possible.

Chapter 2. Experimental

2.1. Physical Measurements and General Comments

Materials

Commercially available solvents and chemicals were used without further purification.

Elemental Analysis

CHN analyses were carried out by Canadian Microanalytical Services, Delta, British Columbia, Canada. Transition metal analyses were carried out using atomic absorption on a Varian SpectrAA-55 in absorbance mode. Samples were digested in concentrated nitric acid and diluted to the appropriate volume with deionized water.

Spectroscopy

Infrared spectra were recorded on a Mattson Polaris FT-IR spectrometer as Nujol mulls pressed between KBr disks.

Electronic transmittance spectra were recorded in the solid state as Nujol mulls using a Cary 5E spectrometer.

NMR spectra were recorded on a General Electric 300 MHz NMR spectrometer at room temperature.

Mass Spectrometry

Mass spectra were run on a VG Micromass 7070HS by Ms. Marion Baggs and Dr. Brian Gregory. MALDI-TOF MS were run by Ms. Linda Windsor on an Applied Biosystems DE-RP equipped with a reflectron, delayed ion extraction and high performance nitrogen laser (337 nm). A CHCA matrix was used and samples were

dissolved in a 1:1 mixture of deionized water and acetonitrile. Calibration was achieved through the use of a commercially available calibration mixture for the range 500 – 6000 M/Z.

Magnetic Measurements

Room temperature magnetic moments were recorded using the Faraday method on a homemade magnetometer comprising a Mettler 4432 microbalance and a Cahn 0.8 T permanent magnet equipped with Faraday pole caps. Variable temperature and magnetization measurements were made on a Quantum design MPMS5S SQUID magnetometer with samples contained in gelatin or aluminum capsules inside a drinking straw. Background correction for the sample holder were applied. Diamagnetic corrections were estimated from Pascal's constants.[47]

Mössbauer Spectroscopy

The Mössbauer spectra were determined by Dr. William Reiff at Northeastern University, Boston, using a conventional constant acceleration spectrometer operated in multichannel scaling mode. The γ-ray source consisted of a fresh 120 mCi sample of Co^{57} in a rhodium metal matrix that was maintained at ambient temperature. The spectrometer was calibrated using a 6-micron thick natural abundance iron foil. Isomer shifts are reported relative to the center of the magnetic hyperfine pattern of the latter foil taken as zero velocity. The line widths of the inner-most pair of $\Delta M_I = \pm 1$ transitions of the latter Zeeman pattern were reproducibly determined to be 0.214 mm/s. Sample temperature variation was achieved using a standard exchange gas liquid helium cryostat (Cryo Industries of America, Inc.) with temperature measurement and control based on

silicon diode thermometry in conjunction with a 10 μA excitation source (Lakeshore Cryotronics, Inc.). The spectra were initially fitted to unconstrained Lorentzians using the program ORIGIN (Micro Software, Inc.)

ESR Spectroscopy

Xband ESR spectra were recorded with a Bruker ESR spectrometer by Dr. William Reiff at Northeastern University, Boston.

X-Ray Crystallography

The data for the picolinic hydrazide methyl pyruvate adduct was obtained by Mr. David Miller on a Rigaku AFC6S diffractometer at Memorial University of Newfoundland. The data for $[(Cl2POAP)_6Fe_9](ClO_4)_8 \cdot 23H_2O$ were obtained by Dr. Bob McDonald at the University of Alberta on a Bruker P4/CCD system with graphite monochromated Mo-Kα radiation and a sealed-tube generator.

X-Ray Crystallography Data Collection

$[(Cl2POAP)_6Fe(II)_8Fe(III)](ClO_4)_8 \cdot 23H_2O$ (**3**)

The diffraction intensities of a black prism crystal of **3** were collected with graphite monochromatized Mo Kα X-radiation (rotating anode generator) using a Bruker P4/CCD diffractometer at -80(1) °C to a maximum 2θ value of 52.9°. The data were corrected for Lorentz and polarization effects. The structure was solved by direct methods[53] and expanded using Fourier techniques.[54] Some-non hydrogen atoms were refined anisotropically, while the rest were refined isotropically. Hydrogen atoms were included but not refined. Neutral atom scattering factors[55] and anomalous-dispersion terms[56,57] were taken from the usual sources. All other calculations were performed using

the teXsan[58] crystallographic software package using a PC computer, except for refinement, which was performed using SHELXL-97.[59]

The model contains a very disordered perchlorate which was fixed during refinement. There is also a poorly refined acetonitrile and two disordered methanol molecules in the lattice. The formula was corrected for a total of ten hydrogen atoms which are missing from the lattice methanol and water. While the charge is apparently balanced the occupancy of the perchlorates is not conclusive from the data, and only observations about the molecular cation are presented.

POMeO

The diffraction intensities of a black prism crystal of POMeO were collected with a Rigaku AFC6S diffractometer with graphite monochromated Mo-Kα radiation at 26(1) °C to a maximum 2θ value of 55.2°. Structure refinement of POMeO was carried out in a similar manner to **3**.

2.1.1. AC/DC SQUID Magnetometry

DC susceptibility measurements made on a SQUID magnetometer measure the equilibrium value of magnetization of a sample in a constant (i.e. DC) field. The magnetic moment of the sample is measured producing the DC susceptibility curve. Measurement of the sample involves using a set of superconducting coils and a SQUID detector in order to measure the current induced in the superconducting coils as the sample is moved relative to the coils. Often the applied DC field must be quite large in order to provide a sufficiently large induced moment in the sample.

AC measurements on the other hand involve the use of a relatively small alternating magnetic field in order to probe the ability of magnetic systems to reorganize their moments as a function of alternating field.

At low frequencies, when the measurement is quite similar to DC measurements, as long as the AC field is small the induced AC moment is given by:

$$M_{AC} = (dM/dH)H_{AC} \sin(\omega\tau) \qquad (11)$$

Where: H_{AC} is the amplitude of the driving field
ω is the driving frequency
and $\chi = dM/dH$ being the susceptibility, the slope of the M(H) curve.

Since the measurement is sensitive to the slope of the M(H) curve and not the absolute value of the signal, quite small changes on a large absolute signal can be distinguished. In higher frequency cases, in which there is an energy barrier to the reorganization of the sample's magnetic moment, the magnetization of the sample may lag behind the drive field, an effect which is detectable by the SQUID coils as an out of phase signal. This gives two quantities, the magnitude of the susceptibility, χ, and the

phase shift φ. The more common way of representing these quantities however is to divide the susceptibility into two components; an in-phase, or real, component, χ', and an out-of-phase, or imaginary, component χ''. For the case where χ'' is zero, χ' and χ are the same, and the information is identical to the DC susceptibility.

Hysteretic magnetic systems make the use of AC susceptibility measurements attractive, as there exists an energy barrier to the reorganization of the magnetic moment. As previously mentioned, this resistance to the realignment of the magnetic field will be detected by the SQUID coils as an out of phase signal.

The magnetic properties of the systems can be studied as a function of a number of variables as the intensity and oscillation frequency of the AC field can be varied, in addition to the application of a DC field.

2.1.2. Mössbauer Spectroscopy

Mössbauer Spectroscopy involves using the Mössbauer effect, the phenomenon of recoil-free nuclear resonance fluorescence. It involves the emission or absorption of a γ-ray photon without any loss of energy due to recoil of the nucleus of the target, and without thermal broadening. Discovered by Rudolph Mössbauer in 1957[60] its main feature is the production of monochromatic electromagnetic radiation with a very narrowly defined energy spectrum. This allows it to be used to resolve minute energy differences, such as the interaction between the nucleus and the extra-nuclear electrons.

The Mössbauer effect has been detected in a total of 88 γ-ray transitions of 42 different elements. In theory it is present for all excited-state to ground-state γ-ray transitions, however its low magnitude often precludes detection. So far useful applications have been restricted to roughly a dozen elements, thankfully for our purposes, among them is iron.

Mössbauer spectroscopy involves observing the fluorescence resulting from the absorption and emission of a γ-ray photon. As with the absorption of photons the frequency of the emitted photon will be related to the difference in energy of the two states before and after emission (or absorption).

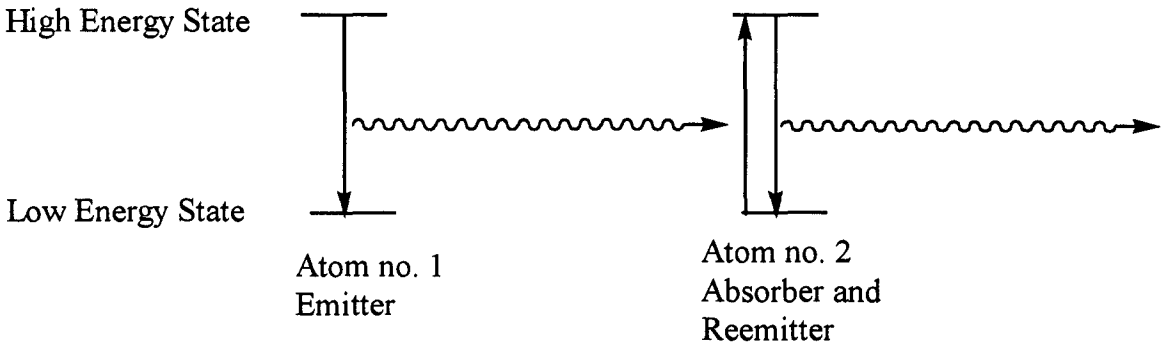

Fig. 17. Transitions between energy states in a Mössbauer experiment.

Since γ-rays are extremely high energy photons, a significant fraction of the energy of transition would be dissipated in recoil were the atoms free to move, and therefore too low in energy to excite nucleus no. 2 (see Fig. 17). This limits the type of sample that may be run since in order to assure recoil-less interactions the samples must be solid, often at low temperatures, with crystalline forces holding the emitting atom firmly in place in order to prevent the recoil.

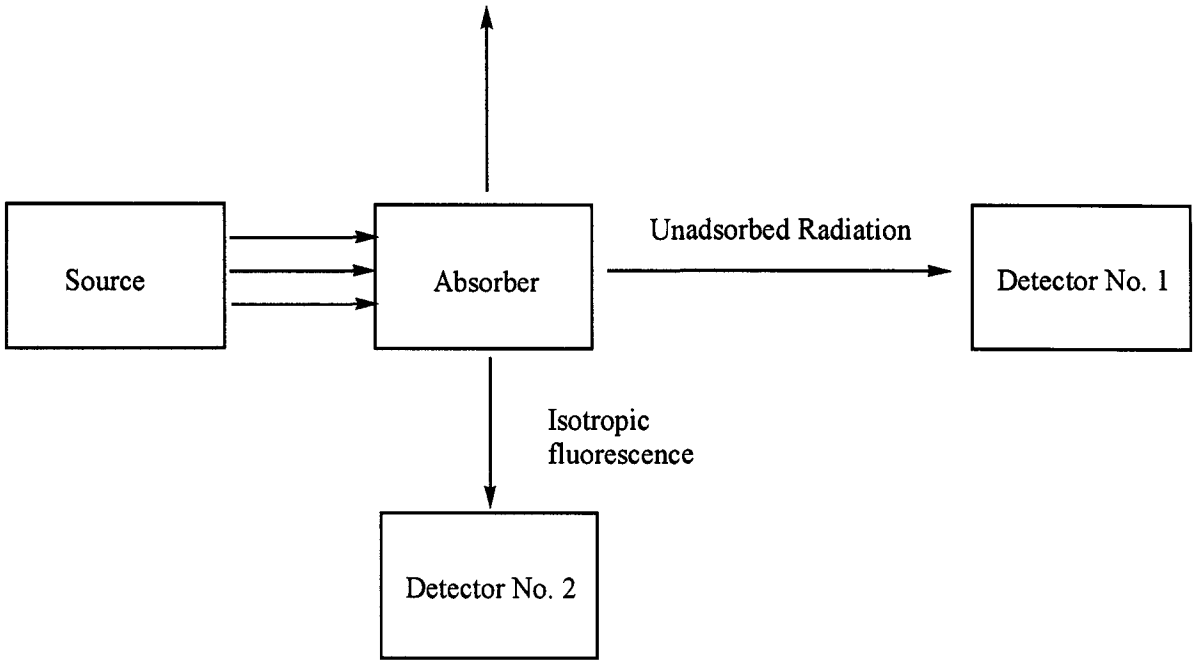

Fig. 18. Diagrammatic representation of a Mössbauer experiment. When resonance occurs photons are detected at No. 2 and fewer at No. 1 as some of the radiation is absorbed.

There are two methods of detecting Mössbauer resonance available (see Fig. 18). With the detector at position No. 1, a decrease in the intensity of the radiation will be observed as some of it is absorbed and reemitted at resonant frequencies in directions other than that of the original beam. With the detector is position No. 2, the isotropic radiation can be measured directly as the absorber is excited by the resonant γ-ray photons and reradiates them.

The nuclear energy levels which are responsible for these transitions will be perturbed slightly by the electron density at the nucleus. This is what allows the Mössbauer effect to serve as a useful probe of the electronic environment about the

nucleus of an atom in a molecule. In order for absorption and the subsequent fluorescence to occur atoms 1 and 2 must be in identical environments, otherwise it will not occur (unless by chance the perturbation of the two different environments is identical). To obtain quantitative measures of the differences between two nuclear environments it is possible to cause absorption and fluorescence in cases where it would not occur by taking advantage of the Doppler effect. This involves increasing or decreasing the frequency of the photon traveling between the emitter and the absorber through moving the emitter or absorber towards or away from one another. This motion causes a Doppler effect in the beam modifying its frequency and allowing its energy to match that of the energy difference in the sample. The motion is measured in millimeters per second (mm/s) and is called the isomer shift (δ), a measure of the difference of the chemical environment of the two nuclei. Values of the isomer shift for Fe(III) (HS) and Fe(II) (HS) are typically in the range ~ 0.5 -0.7 mm/s and ~ 1.3 mm/s respectively, although these values can vary depending on the ligands coordinated.

More powerful from a structural point of view, however, is the quadrupole splitting of the signal (ΔE_Q) which reveals the asymmetry of the electric field surrounding the metal center. The less symmetrical the field about the metal center the larger the value of ΔE_Q.

2.2. Ligand Syntheses

2.2.1. Extending Known Ligands

The ligands in this work were synthesized through a general synthetic route involving generating the necessary contiguous series of five-membered rings as well as the oxygen bridges by taking advantage of Schiff-base type linkages between the carbonyl groups of appropriate precursors. The general scheme is presented in Fig. 19. The only requirement for the groups R, R' and R'' is that they not interfere with the reaction, and in order to form useful ligands with this structural moiety these R groups must have suitable metal binding capacity in order to properly form the coordination "pockets". A wide variety of ligands have been synthesized using this methodology, including POAP[61] (R' = NH_2, R = R'' = pyridine), PzOAP[62] (R' = NH_2, R = pyrazine, R'' = pyridine), POAPz[63] (R' = NH_2, R = pyridine, R'' = pyrazine), and PzOAPz[64] (R' = NH_2, R = pyrazine, R'' = pyrazine).

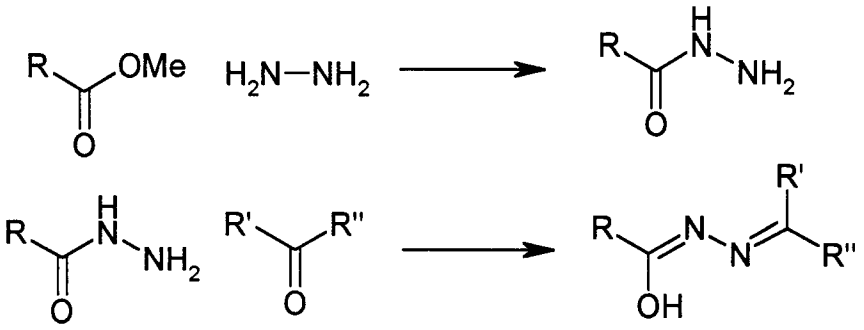

Fig. 19. General Schiff-base-type linkage scheme.

2.2.2. Adding "Pockets" Through Doubling the Ligand

In the case of the ligand POAP, the initial R group is a pyridine ring, the second R' in the final product is a monoamine, and R'' is also a pyridine ring, thus there are two "pockets" capable of binding metal cations. Notice that the right hand pocket is tridentate while the left hand one is bidentate (see Fig. 20).

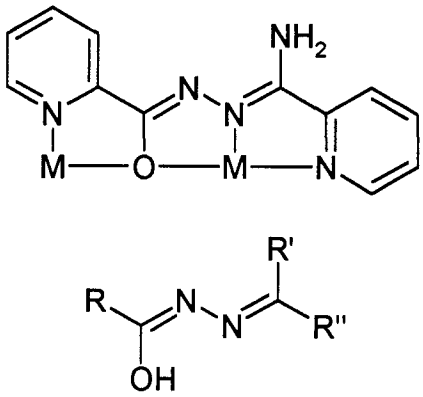

Fig. 20. Comparison of POAP (showing metal binding modes) and the general ligand form.

Extension of the ditopic ligand POAP by effectively doubling the alkoxo-bridging fragment through the use of a 2,6-disubstituted pyridine central unit has been successful in generating the ligand 2POAP whose [3×3] grid forming chemistry has been reported.[22] Using this 2,6-disubstituted precursor, an additional metal binding pocket was added to the ligand POAP and in addition the bidentate metal-binding pocket of the POAP ligand has been "completed" forming a tridentate pocket in its place (see Fig. 21). This has the effect of generating a symmetrical ligand (unlike POAP which has directionality caused by a lack of symmetry).

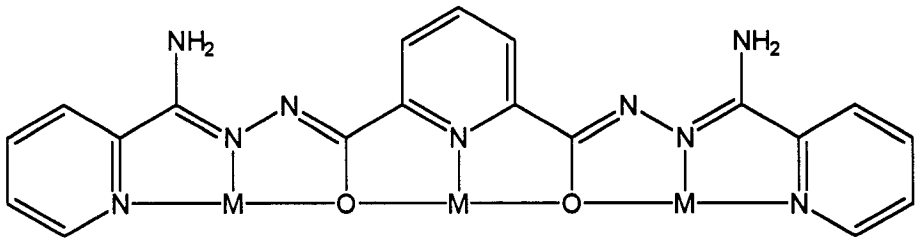

Fig. 21. Tritopic coordination mode for 2POAP. Note the ligand symmetry.

The asymmetry of POAP has implications for any grids formed. In grids formed from ligands which are not symmetrical, there are a variety structural isomers possible in which the ligands align in different directions about the plane described by the metals (see Fig. 22).

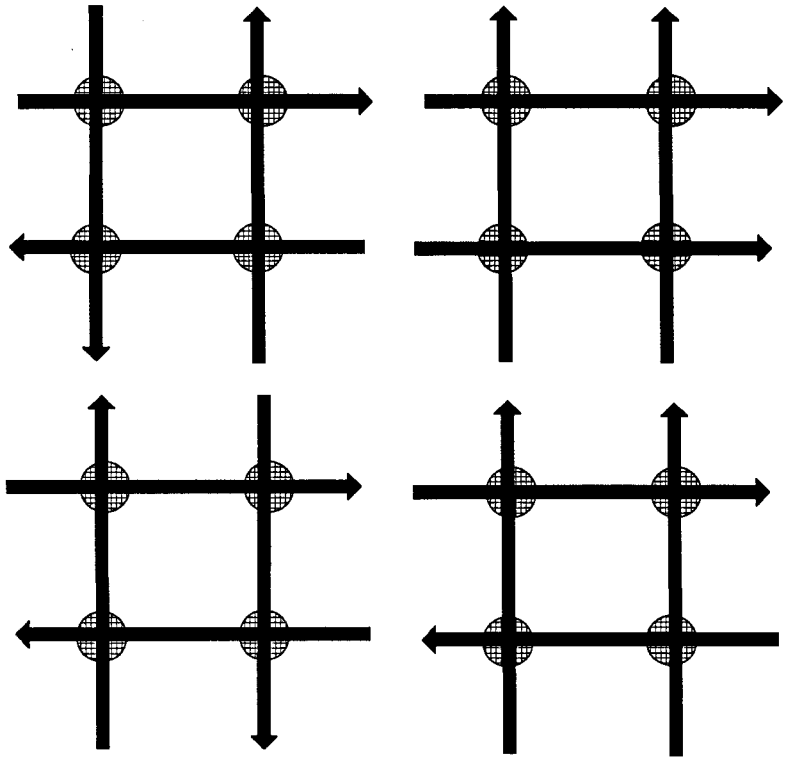

Fig. 22. Some structural isomers of [2×2] grids based on POAP.

Unlike POAP, 2POAP being symmetrical, will form homoleptic [3×3] grids in which there is only one type of ligand coordinating to the metal cations. In addition, since the three metal binding pockets of 2POAP are all tridentate, no additional ligands will be required to satisfy the coordination requirements of nine octahedral metals. Since nine metals coordinated octahedrally require (9×6 =) 54 donors and six 2POAP ligands provide (6×9 =) 54 donors, the match between ligand and cation is perfect.

The extended ligand 2POAP can form [3×3] grids with a variety of metals including Mn(II)[23], Cu(II)[22,65], and Fe(III).[66] Developing ligands with similar metal binding schemes from a variety of precursors should allow the formation of novel ligands which have the potential to form grids similarly to 2POAP.

2.2.3. Spacer Approach to Extending Ligands

A different approach increasing the number of metal binding pockets in a ligand involves the use of a molecular "spacer". This approach focused on the diazine linkage common to these types of ligands. Through introducing the properly designed spacer, the number of binding pockets in the ligand could be expanded while leaving the ends of the ligand unaltered (see Fig. 23).

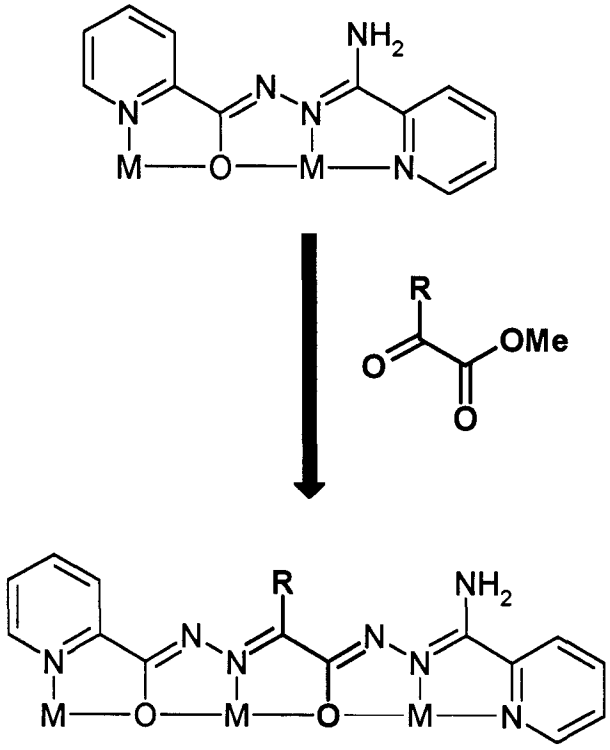

Fig. 23. Extended derivative of POAP through incorporation of a spacer into the ligand's design.

Through the addition of a "spacer molecule", the number of contiguous binding pockets can be increased from two, as in POAP, to three. An appropriate spacer for this purpose must be of the basic form shown in Fig. 23. It must have two adjacent carbonyl

groups, of which one is an ester group. The non-ester carbonyl group must be more reactive to Schiff-base formation with hydrazides than the ester in order that the spacer is orientated properly to allow proper formation and bridging of the new metal binding pocket. Finally, for our purposes, the group R should be non-interactive with the metals since in the grid this group does not participate in bonding.

Since a stabilizing force holding the ligands in the proper positions in the grid complex appears to be π-stacking of the aromatic rings in the ligand, it would be logical to try to counter the increased flexibility of the ligand resulting from its extension by incorporation of a benzene ring as the group R. On the other hand, using a smaller R group, such as a methyl group, might have the advantage of reducing steric congestion between ligands in the parallel arrangement in a grid complex, especially if the benzene analogue does not undergo π-stacking, the size of the benzene group could be disruptive to the interactions the ligands must undergo to build a grid.

Attempts to use methyl pyruvate (R = methyl) for generating precursor ligands was not successful. Methyl pyruvate has been used in the past to combine with hydrazide-based precursors such as thiosemicarbazones[67] in order to form ligands which formed a $L_2Cu(II)_2$ dimer and a polymeric stacked LCu(II) chain.

Unlike 2POAP which completely satisfies the coordination requirements of the 9 metals in a [3×3] grid, forming homoleptic clusters, extended POAP ligands using this "spacer" approach will not, as the extended ligand retains the bidentate metal binding pocket consisting of a pyridine and oxygen donor (see Fig. 24). The consequence of this is that there are only 8×6 = 48 available electron-donating groups, while the metals in a

[3×3] grid will require 9×6 = 54 donors. In a grid formed by this ligand, six additional ligands will be required in order to satisfy the octahedral coordination environment of the metals.

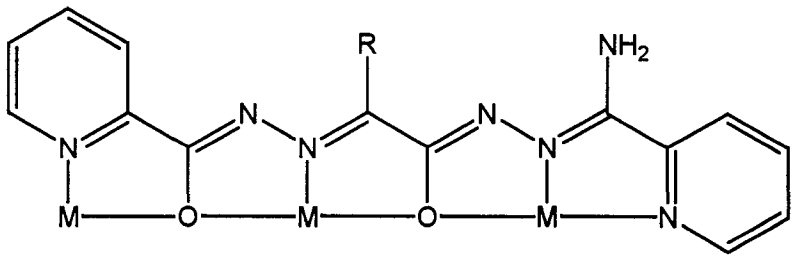

Fig. 24. Extended POAP-type ligand showing possible coordination mode in a grid.

In the [2×2] square grids formed by the ligand POAP, these additional sites are often filled by coordination of solvent molecules, usually water or methanol, or other ligands, e.g. anions with significant donor ability like nitrate and thiocyanate. The match between coordination requirements of the metals and the coordination geometry supplied by the ligand need not be perfect. In cases of homoleptic systems in which there is only one ligand type bound to the metal this non perfect (but close) matching will often be accounted for by distortions of the metals from their ideal bond lengths and angles within the grid.

An example of additional ligands filling metal coordination sites is the complex $[(POAP\text{-}H)_4Fe_2Ni_2(NO_3)_4](NO_3)_2{\cdot}CH_3OH{\cdot}5H_2O$[68] which consists of 4 pentadentate POAP ligands which account for 20 of the 24 coordination sites required by the 4 octahedral metal cations. The remaining 4 sites on the iron cations are filled by solvent and nitrate anions acting as monodentate ligands, binding directly to the metal (see Fig. 25).

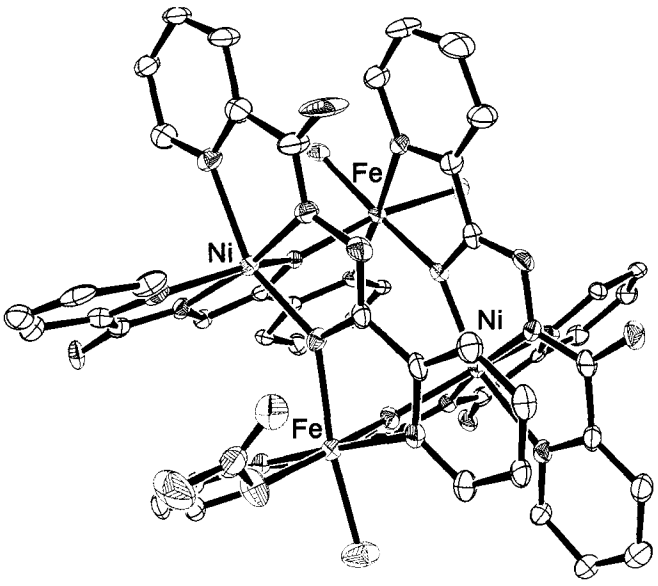

Fig. 25. Crystal structure of $(POAP\text{-}H)_4Fe_2Ni_2(NO_3)_6 \cdot CH_3OH \cdot 5H_2O$; additional solvent molecules and nitrate anions are bound to the iron centres.

2.3. Ligand Experimental

2.3.1. Linear Ligands

P2OAP

P2OAP was synthesized according to Scheme 1.

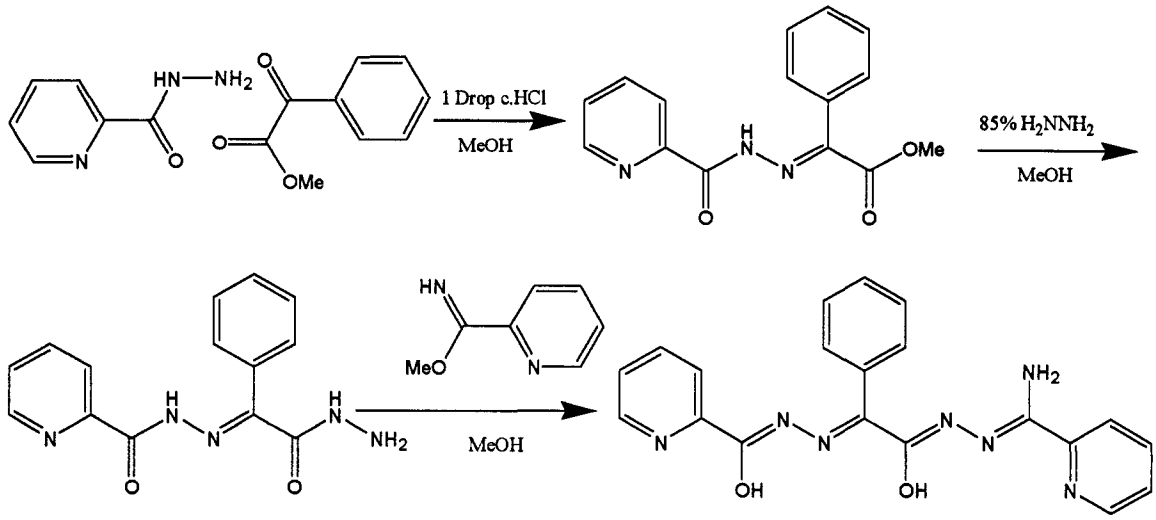

Scheme 1. Synthesis of P2OAP.

Methyl benzoylformate (2.64 g, 0.0161 mol), was dissolved in methanol (100 mL) and picolinic hydrazide[69] (2.01 g, 0.0147 mol) was added. This solution was refluxed for 14 h and produced a white solid which was collected by suction filtration, washing with ice-cold methanol and diethyl ether. (Yield = 3.8 g, (91%); mp 131-134°C; Mass Spectrum M/z 283 (M^+), 224, 167, 105, 79. FT-IR (υ in cm^{-1}) υ(OH) 3282, υ(CO, ester) 1705, υ(CO) 1640, υ(CN) 1587, υ(py) 996. ^{1}H-NMR: (300MHz, D_6-DMSO, 25°C, δ in ppm) δ 8.7 (m, 1H, 1 pos. of py.), δ 8.4 (m, 2H, 2, 3 pos. of py.) δ 7.9 (m, 3H, overlap of 4 pos. of py. and 1,6 pos. of benzene), δ 7.8 (m, 3H, 3, 4, 5 positions of benzene), δ 3.95 (s, 3H, methyl ester)).

The picolinic hydrazide methylbenzoylformate adduct (3.39 g, 0.0120 mol) was suspended with stirring in methanol (100 mL) cooled in an acetone/dry ice bath. Hydrazine hydrate 85% (1.69 g, 0.0447 mol) was added dropwise and the solution stirred overnight producing a white solid collected by suction filtration, washing with cold methanol and diethyl ether. (Yield = 2.1 g, (61.9%); mp 166-167°C M/Z 283 (M^+), 224, 167, 105, 78. FT-IR (υ in cm^{-1}) υ(OH) 3282, υ(CO hydrazide) 1687, υ(CO) 1640, υ(CN) 1587, 1547, υ(py) 996. ^{1}H-NMR: (300MHz, D_6-DMSO, 25°C, δ in ppm) δ 8.7 (m, 1H, 1 pos. of py.), δ 8.2 (m, 2H, 2, 3 pos. of py.) δ 7.7 (m, 3H, overlap of 4 pos. of py. and 1,6 pos. of benzene), δ 7.5 (m, 3H, 3, 4, 5 positions of benzene), δ 4.9 (v. wide, N-H protons)).

A small piece of sodium was dissolved in dry methanol (100 mL) with stirring. Molten 2-cyanopyridine (1.059 g, 0.01017 mol) was added, and the solution was left to stir overnight. The hydrazide of the picolinic hydrazide methylbenzoylformate adduct was added, and the mixture stirred at room temperature for 14 h. The initially colourless solution turned yellow with the formation of a yellow solid. The yellow solid was collected by suction filtration, washed with cold methanol and diethyl ether. (Yield = 1.2 g (30%); mp: 231-234°C; Anal. Calcd. for $C_{20}H_{17}N_7O_2$, C, 62.01; H, 4.42; N, 25.31. Found: C, 62.00; H, 4.35; N, 25.43. Mass Spectrum; M/z 387 (M^+), 368, 291, 263, 250, 224, 163, 119, 105, 78. FT-IR (υ in cm^{-1}) υ(OH) 3296, υ(CO) 1691, υ(CO) 1639, υ(CN) 1561, υ(py) 1002. ^{1}H-NMR (300MHz, D_6-DMSO, 25°C, δ in ppm): δ 8.6 (d, 1H, 1 pos. of py. near -OH), δ 9.5 (d, 1H, 1 pos. of py. near $-NH_2$), δ 8.1 (m, 4H, overlap of pos. 2

and 3 of both py. rings) δ 7.9 (m, 2H, pos. 5 on both py. rings) δ 7.5 (m, 2H, pos. 2 and 6 on benzene ring) δ 7.4(m, 3H, pos. 3,4, and 5 on benzene ring)).

POMeO

The use of methyl pyruvate in place of the methylbenzoylformate for extending the series of metal binding pockets was attempted. To a solution of methyl pyruvate (10.10 g, 0.0989 mol) in methanol (100 mL), picolinic hydrazide (12.19 g, 0.0990 mol) was added and the mixture refluxed for 14 h, forming a colourless solution. On cooling to room temperature a white crystalline solid formed. (Yield 15.9 g (73%); mp: 169-172°C; Mass Spectrum: M/z 221 (M^+), 162, 137, 106, 78. ^{1}H-NMR (300MHz, D_6-DMSO, 25°C, δ in ppm): δ 11.21 (s, 1H, OH), 8.7 (m, 1H pyridine H), 8.4 (m, 1H pyridine H), 8.0 (m, 1H pyridine H), 7.6 (m, 1H pyridine H), 4.0 (s, 3H $-CH_3$), 2.4 (s, 3H $-OCH_3$)). Further reactions were unsuccessful and the synthesis was halted at this point.

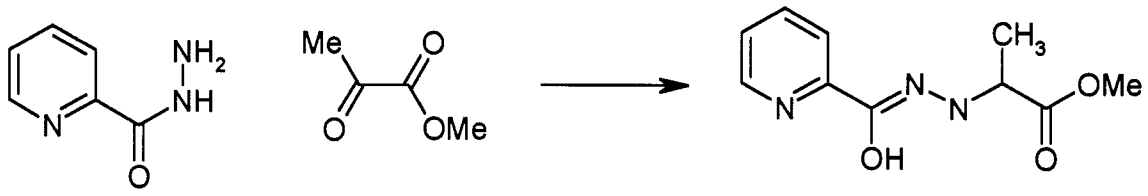

Scheme 2. Synthesis of POMeO.

2POAN

The synthesis of 2POAN is outlined in Scheme 3.

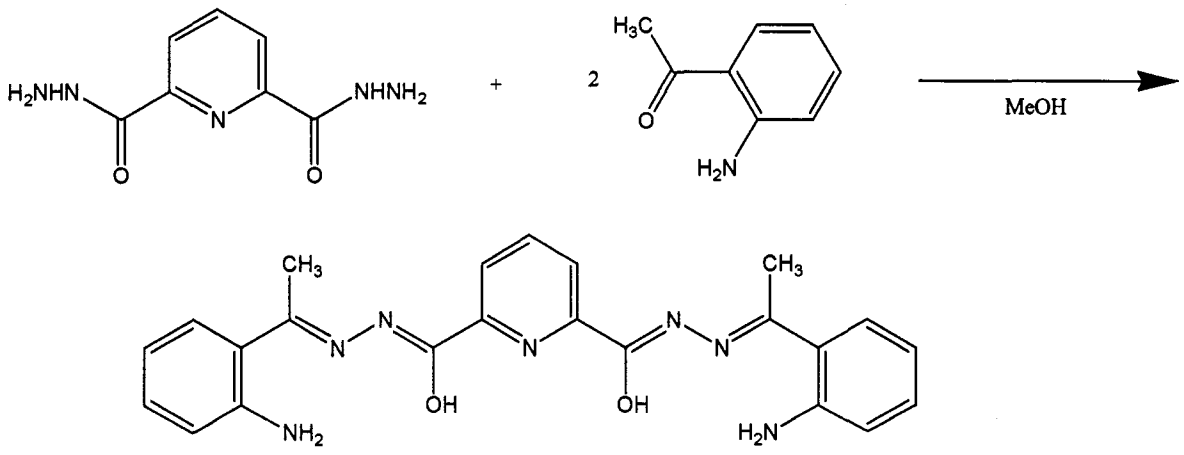

Scheme 3. Synthesis of 2POAN.

2-Aminoacetophenone (3.50 g, 0.0259 mol) was dissolved in methanol (100 mL) and 2,6-pyridine dicarboxylic acid dihydrazide[16] (2.395 g, 0.01228 mol) was added. The mixture was stirred and refluxed for 14 h producing a yellow solid which was collected by suction filtration, and washed with ice cold methanol and diethyl ether (Yield = 4.25 g (80.6%); Anal. Calcd. for $C_{22}H_{23}N_7O_2$, C, 64.32; H, 5.40; N, 22.83. Found: C, 64.01; H, 5.29; N, 22.84. Mass Spectrum; M/z: 429(M^+), 413, 382, 281, 223, 133, 92, 78. FT-IR (υ in cm^{-1}) υ(OH) 3421, $\upsilon(NH_2)$ 3326, 3269, υ(CO) 1688, 1664, υ(CN) 1610, 1557).

2POAO

The synthesis of 2POAO is outlined in Scheme 4.

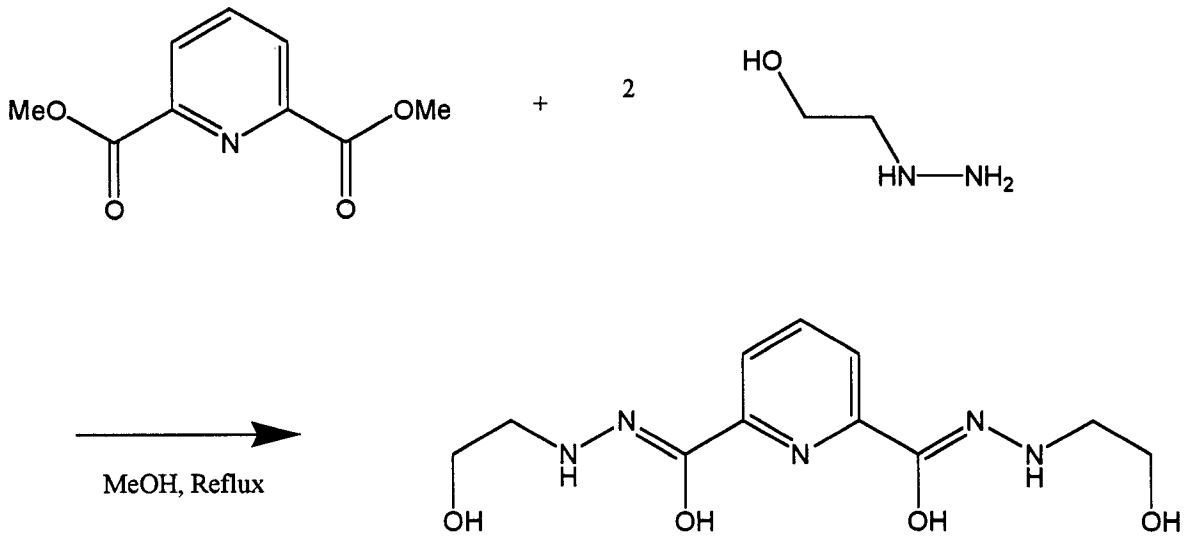

Scheme 4. Synthesis of 2POAO.

Pyridine-2,6-dicarboxylic acid dimethyl ester[16] (2.61 g, 0.0152 mol) was dissolved in methanol (100 mL) and 2-hydroxyethylhydrazine (1.83 g, 0.0240 mol) was added. The solution was refluxed for 14 h during which a yellow solution formed. The product was obtained as an impure hydroscopic yellow solid by removing the solvent and drying the residue under vacuum. (Yield = 2.88 g, (90%); mp: 100-103 °C; Mass Spectrum: M/z 283(M^+), 208 (M^+-NNH(C_2H_2)$_2$OH), 137, 105 (pyCHO-H), 77 (py-2H). FT-IR (υ in cm^{-1}) υ(OH) 3250, υ(CO) 1729, υ(CN) 1666, υ(py) 997. ^{1}H-NMR (300MHz, D_4-MeOD, 25°C, δ in ppm): δ 8.0 (m, 3H aromatic) δ 4.10 (m, 4H, CH_2) δ 3.65 (m, 4H, CH_2)).

Cl2POAP

The synthesis of Cl2POAP has been previously reported.[70]

2.3.2. Non-Linear Ligands Incorporating Linear Metal-Binding Arrays

A variety of ligands were synthesized which deviate from the strict template provided by the 2POAP metal binding geometry.

di-OAOP

The synthesis of di-OAOP is outlined in Scheme 5.

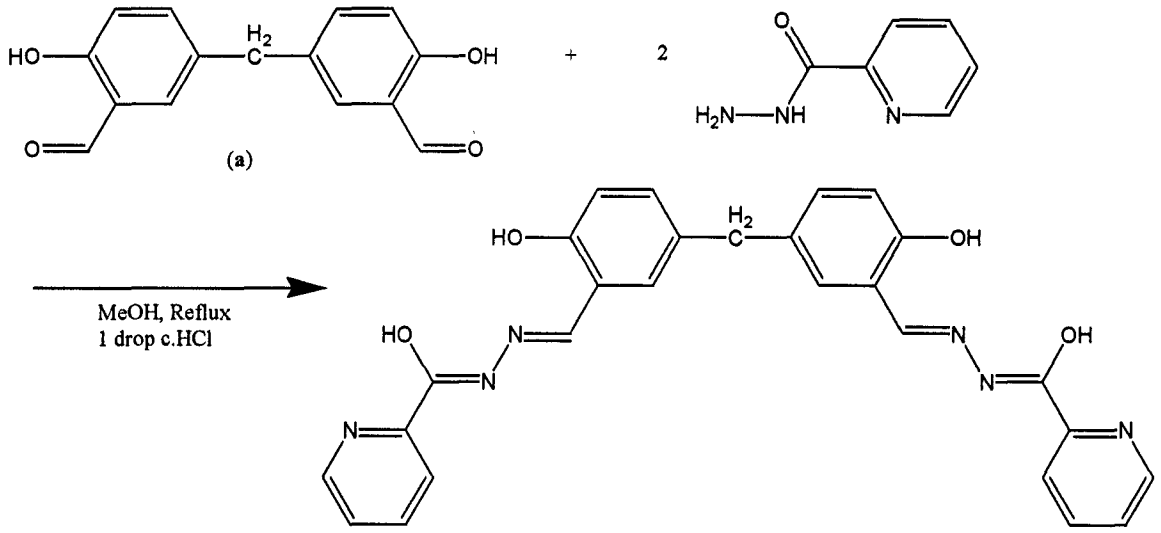

Scheme 5. Synthesis of di-OAOP.

The compound (**a**) (1.31 g, 0.00408 mol), was partially dissolved in methanol (100 mL) with stirring and heating. Picolinic hydrazide[69] (1.176 g, 0.00858 mol) was added in addition to one drop of concentrated HCl, and the mixture refluxed overnight. The yellow solid which formed was collected by suction filtration, washing with ice cold methanol and diethyl ether. (Yield 1.98 g (98.1%); mp: 269-271 °C; Anal. Calcd. for $C_{27}H_{22}N_6O_4$: C, 64.79; H, 5.64; N, 16.79. Found: C, 64.85; H, 4.43; N, 16.56. Mass Spectrum; M/z 494 (M^+), 373 (M^+-NCOH-py), 250 (M+-2×NCOH-py-2H), 78(py). FT-IR (υ in cm^{-1}) υ(OH) 3165, υ(CO) 1661, υ(CN) 1623, υ(CN) 1580, υ(py) 998.)

2PAOP

The synthesis of 2PAOP is outlined in Scheme 6.

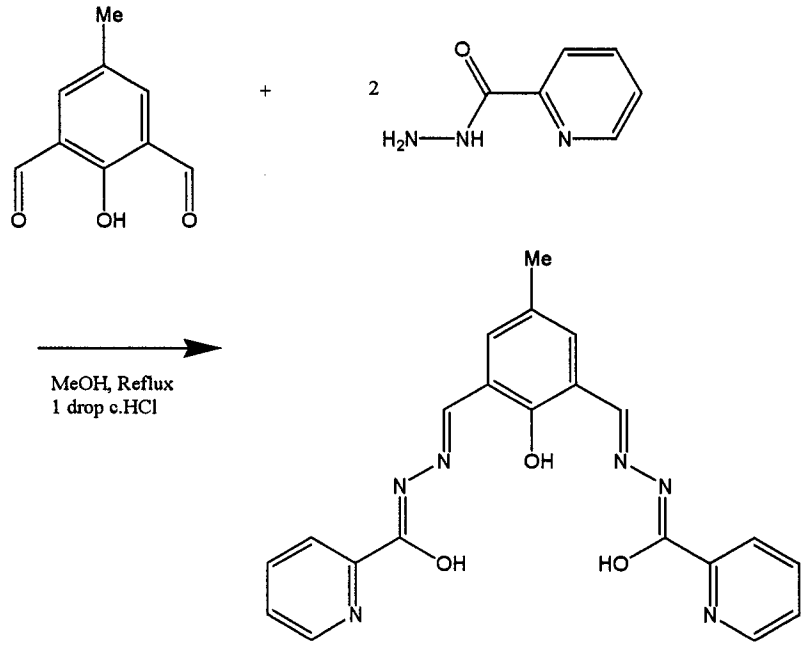

Scheme 6. Synthesis of 2PAOP.

2,6-Diformyl-4-methylphenol (1.02 g, 0.00626 mol) was dissolved in methanol (100 mL) and picolinic hydrazide[69] (1.73 g, 0.0126 mol) and one drop of concentrated HCl was added with stirring. The mixture was refluxed overnight, forming a yellow solution with a small amount of yellow solid. On standing, small orange crystals formed. (Yield = 2.13 g (84.6%); mp >275°C; Anal. Calcd. for $C_{21}H_{18}N_6O_3 \cdot 0.25H_2O$: C, 61.99; H, 4.58; N, 20.65. Found: C, 61.99; H, 4.75; N, 20.02. Mass Spectrum: M/z 402 (M^+), 218 (M^+-NCOH-py), 122, 106, 79 (py). FT-IR (in cm^{-1}) υ(OH) 3246, υ(OH) 3175, υ(CO) 1675, υ(CN) 1616, υ(CN) 1588, υ(py) 996).

Chapter 3. Ligand Discussion

3.1. General Comments on Ligands

3.1.1. Keto-Enol Tautomerization

All of the ligands discussed in this study are capable of undergoing tautomerization as shown in Fig. 26. In the free ligand, the keto form will be the dominant contributor, due to the greater stability of the C=O double bond as compared with the C=N double bond. In complexes, however in which the oxygen serves as a bridge, the enol form is the more stable. In this form the oxygen atom will have greater electron density compared with the keto-form, allowing a greater interaction with the metal. Since this is the form most often seen in complexes, this is the form used to represent the ligands in general.

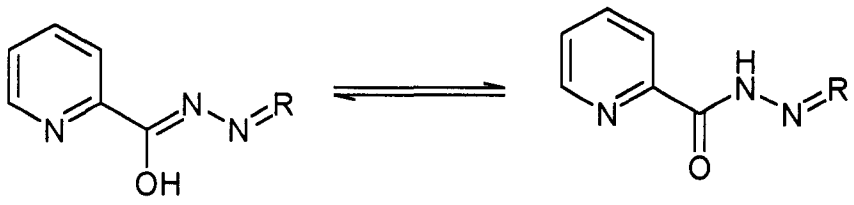

Fig. 26. Tautomerization in diazine-based ligands.

3.1.2. Flexibility of Ligands

All the hydrazide-based ligands show flexibility as a result of the N-N diazine moiety they incorporate. This flexibility leads to a great deal of potential topological variation. Within the diazine N-N moiety there is the potential for rotation about the N-N bond (α in Fig. 27), as well as bending about the C-N-N moiety (β and β' in Fig. 27). These two modes of distortion allow the metal binding pockets which incorporate the diazine linkage the flexibility to distort when complexing metal cations, thereby allowing ligands the flexibility to coordinate to a variety of metal cations of differing sizes.

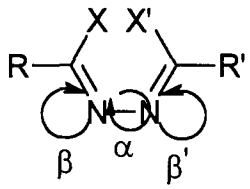

Fig. 27. Conformational flexibility of diazine-based ligands.

Additionally, the R and R' groups are able to rotate about the C-R/R' single bond, allowing for a large topological variation depending on the conformation of the ligand.

3.2. Ligand Discussion

P2OAP

The physical properties of the substance isolated are consistent with the structure proposed for the ligand P2OAP. The elemental analysis is very close to that calculated for the ligand's formula of $C_{20}H_{17}N_7O_2$, and the molecular ion peak at 387 M/z appears at the correct value for the ligand with appropriate degradation fragments. The infrared spectrum shows absorptions corresponding to the two types of CO present and CN (1691, 1639, and 1561 cm^{-1} respectively), which are all typical positions for these groups in this type of diazine-based ligand. The ^1H NMR spectrum, although complex, with exclusively aromatic protons, is consistent with the proposed structure.

The proposed structure of the ligand consists of a linear array of three coordination pockets. Were it to bind to three suitable metals it would form a linear contiguous array of five 5-membered rings, resulting in the metal ions adopting a linear arrangement (Fig. 28).

The three metal binding pockets of P2OAP consist of two tridentate and one bidentate pocket. The presence of the bidentate pocket causes the coordination geometry of this ligand to vary from that of the "model" compound for grid formation namely 2POAP, which consists of three tridentate pockets. In a [3×3] grid, P2OAP will therefore not completely satisfy the coordination requirements of 9 octahedral metals as 2POAP does (see Fig. 28) as 9 octahedral metals require 9×6 = 54 donors, while P2OAP provides only 6×8 = 48 donors. This behavior has been previously observed in the ligand POAP

upon which P2OAP is based on. Remaining sites on the metals not filled by the ligands could be filled by solvent molecules or nucleophilic counteranions such as nitrate.[3]

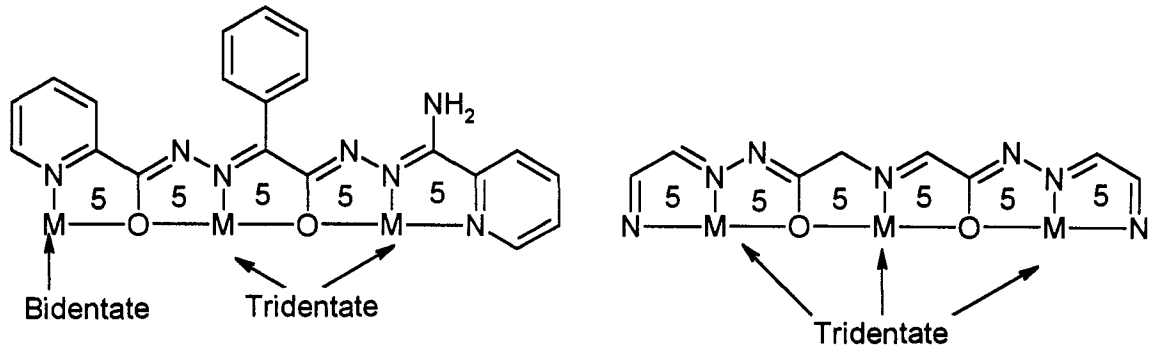

Fig. 28. Comparison of P2OAP ligand's grid-type binding mode with that of the ideal case for grid formation.

POMeO

The physical data are consistent with the structure, the mass spectrum showing the molecular ion peak at 221 M/z, and all protons having been identified in the ^{1}H NMR spectrum.

The X-ray crystal structure of POMeO is illustrated in Fig. 29 and crystallographic details are presented in Appendix B. The structure clearly shows that the ketonic carbonyl of the methyl pyruvate has reacted first in the condensation with the hydrazide as intended. This allows the ester moiety to be free for the intended conversion into another hydrazide. At this point two structural elements of the three planned metal binding pockets have been formed, the central tridentate pocket and the bidentate pocket.

Although the crystal structure indicates the compound is not in the orientation in the solid state necessary for the complexation of metals, the C7-N3 bond is free to rotate due to the keto-enol-like interconversion and were it necessary the proper conformation for the formation of a meal-binding pocket could be easily accessed in solution.

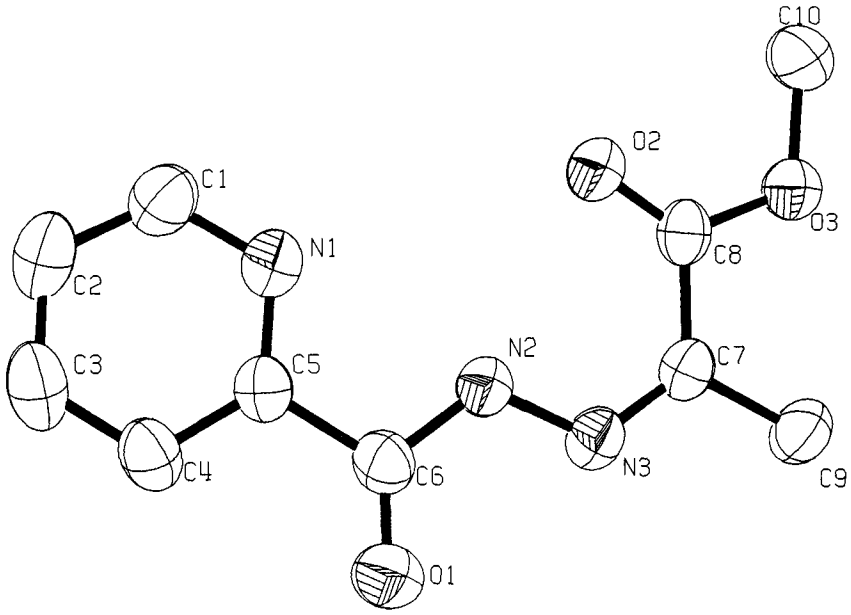

Fig. 29. Crystal structure of picolinic hydrazide methyl pyruvate adduct.

The formation of the hydrazide of the methyl pyruvate adduct presented some synthetic difficulty. The room temperature reaction of POMeO with 85% hydrazine hydrate was undertaken, with no products obtained, and no starting material recoverable. The reaction was repeated with cooling in an ice/water bath, and finally a dry-ice/acetone bath, however no desired results were obtained. Only in the dry-ice/acetone bath was the starting POMeO compound recovered, while at higher temperature it appears that decomposition of the starting material occurs. It seems that the initial hydrazide-based

link formed between the methyl pyruvate and picolinic hydrazide is not stable towards the conversion of the ester into a hydrazide.

2POAN

The physical evidence for the formation of 2POAN is consistent with the structure, with both –OH and $–NH_2$ bands appearing in the infrared spectrum (3421, 2236, and 3269 cm^{-1}) in addition to the typical CO and CN bands (at 1688 and 1664 for CO and 1610 and 1547cm^{-1} for CN). The mass spectrum shows the molecular ion peak at 429 M/z. Unfortunately ^1H NMR data are unavailable as the ligand is too insoluble to be dissolved in sufficient quantities to obtain a spectrum. Elemental analysis agrees with the proposed formula.

The potential binding mode of 2POAN differs from that of the ideal situation offered by 2POAP since although a contiguous series of four 5-membered chelate rings could be formed upon chelation with metal cations, the terminal rings would be six-membered (see Fig. 30). The presence of these six-membered rings, while not preventing the formation of the array of metals may cause a distortion in the coordination geometry of the terminal metals.

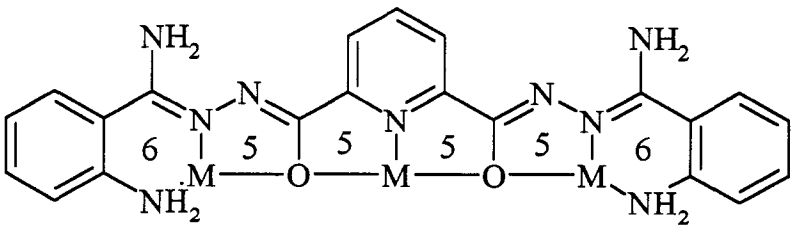

Fig. 30. Potential metal binding modes of 2POAN, emphasizing chelate ring size formed on coordination of metal cations.

2POAO

The physical data for 2POAO are consistent with the structure proposed. The mass spectrum shows the molecular ion peak as well a variety of fragments. The ^{1}H-NMR spectrum clearly shows all protons which are readily identified with the structure of the ligand and the FT-IR spectrum is consistent with the structure showing a very strong wide OH band (3250 cm^{-1}) CO bands (1729 and 1666 cm^{-1}), CN bands (1547 cm^{-1}) and a pyridine band (997 cm^{-1}) all at their typical positions.

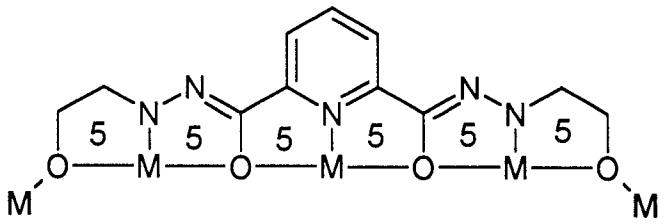

Fig. 31. 2POAO showing potential metal binding modes and potential bridging of terminal primary alcohol moieties.

The structure of 2POAO (Fig. 31) shows the idealized 2POAP-type grid bridging arrangement with the contiguous array of 5-membered chelate rings being formed on complexation of a metal cation. This ligand differs from the 2POAP case however in that the terminating donors of the array are oxygen atoms from primary alcohols, which may possibly bind to further metal cations outside of the cluster that they form through bridging interactions.

When combined with a metal salt, however, no identifiable products were obtained, and the ligand appeared to decompose. The evolution of a gas (N_2) is observed, and the initial dark colour, arising when the metal ion solution and the ligand solution are

mixed fades to that of the free metal ion solution. The metal salts were recovered from these solutions through evaporation, and no complex products were obtained.

di-OAOP

The physical evidence for the identity of this ligand is consistent with the proposed structure. The elemental analysis is consistent and the mass spectrum shows both the molecular ion peak as well as identifiable major fragments. The infrared spectrum shows absorptions corresponding to the CO (1675 cm^{-1}), CN (1623 and 1580 cm^{-1}) and the pyridine breathing mode vibration (997 cm^{-1}), all in their typical positions.

The ligand di-OAOP's design incorporates two identical "wings" each consisting of two metal binding pockets, bridged by an oxygen atom. These "wings" are linked together through a methylene spacer. Since each "wing" is capable of (partly) forming a [2×2] grid, the presence of the linkage between two of these units has the potential to form linkages between grids.

Additionally, while the 2POAP type of metal binding array terminates with a pyridine nitrogen bound to terminal metals, in the di-OAOP ligand a phenolic oxygen is the terminal metal binding moiety. This phenolic oxygen is available to possibly bridge to another metal, raising the potential for interactions between metals on separate adjacent grids mediated by the oxygen (see Fig. 32). In di-OAOP the presence of a six-membered chelate ring may effect the distortion of one of the metal binding pockets.

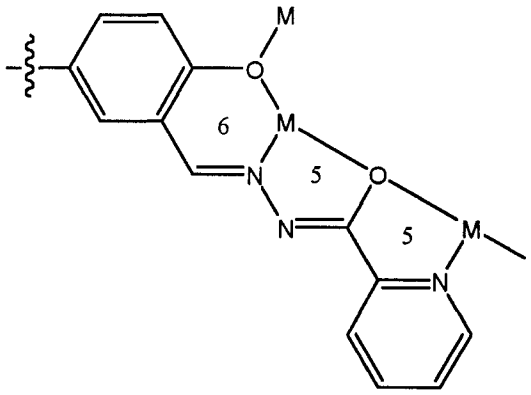

Fig. 32. Portion of di-OAOP ligand showing possible metal binding pockets, emphasizing the size of chelate rings formed, potential bridging of the phenolic oxygen and incomplete coordination sphere of one bound metal.

2PAOP

The physical evidence for the formation of this ligand is consistent with the proposed structure. The elemental analysis is good and the mass spectrum shows the molecular ion peak at 402 M/z in addition to reasonable major fragments. The infrared spectrum shows bands corresponding to the presence of an OH group (at 3246 cm^{-1}) in addition to those typical of CO (at 1675 cm^{-1}), CN (two bands at 1616 and 1588 cm^{-1}) and a pyridine breathing mode at (996 cm^{-1}).

The ligand 2PAOP is quite similar to one prepared by Sakamoto *et. al.*.[71] Their ligand differs from 2PAOP by having benzene rings in place of the pyridine rings present in 2PAOP (Fig. 33).

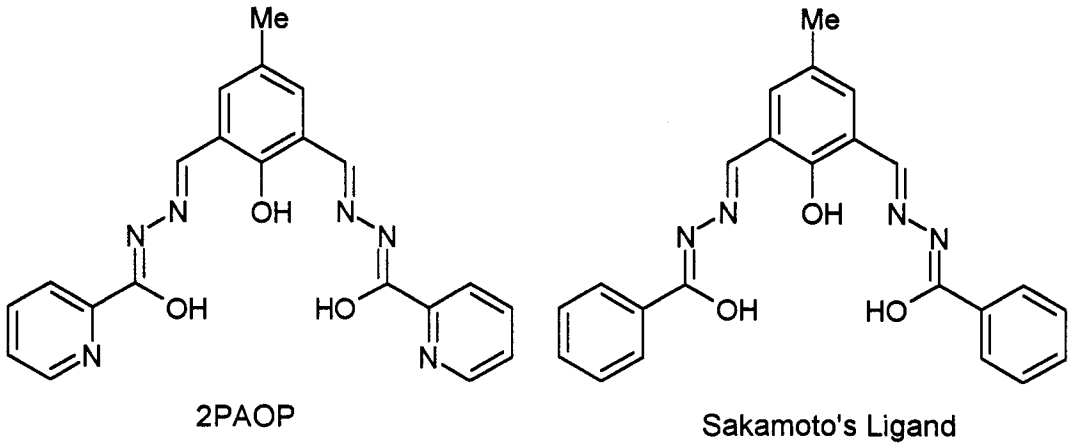

Fig. 33. The ligand 2PAOP and Sakamoto's ligand showing potential metal binding sites.

The presence of the two pyridine rings would add two additional bidentate pockets to the array and the presence of two adjacent fused six-membered chelate rings would result in a bend in the array of metals.

3.3. Attempted Ligand Synthesis

Additional ligands in this class were designed and their syntheses were attempted, but unfortunately the reactions were unsuccessful. The synthetic strategies and reasons for attempting to synthesize them and their complexes will be briefly discussed.

In order to extend the size of the grids from [3×3] to [4×4], a ligand with four contiguous coordination pockets would be required. One potential candidate is shown in Fig. 34. This ligand was designed with a central 2,6-diamino-4-methylphenol moiety which was extended using the "spacer" approach.

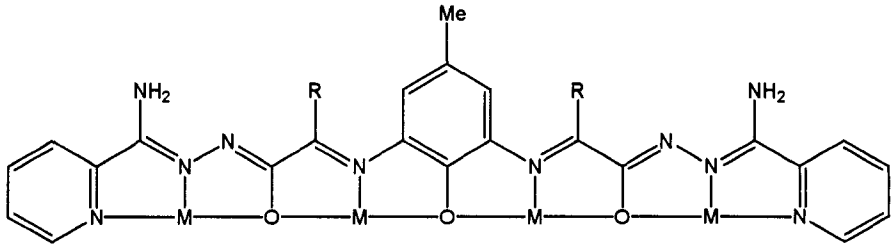

Fig. 34. A potential [4×4] grid-forming ligand showing potential metal binding modes.

Again, choice of the identity of the R group is important; R should not be a donor group in order to prevent interaction with the metals in the grid. Due to the length of the ligand and its flexibility, it would be useful to have an aromatic group for R. This is in order to try to take advantage of π-stacking interactions between rings in adjacent ligands in order to encourage the ligands to form a grid. On the other hand, the steric interactions of a large R group will act to disrupt grid formation either through twisting the ligand out of the linear conformation required for the grid, or through preventing the alignment of adjacent ligands close enough to one another to form a grid. Therefore a smaller group

would perhaps be preferable. Initially methyl pyruvate was utilized to generate the ligand in which R = methyl, according to Scheme 7.

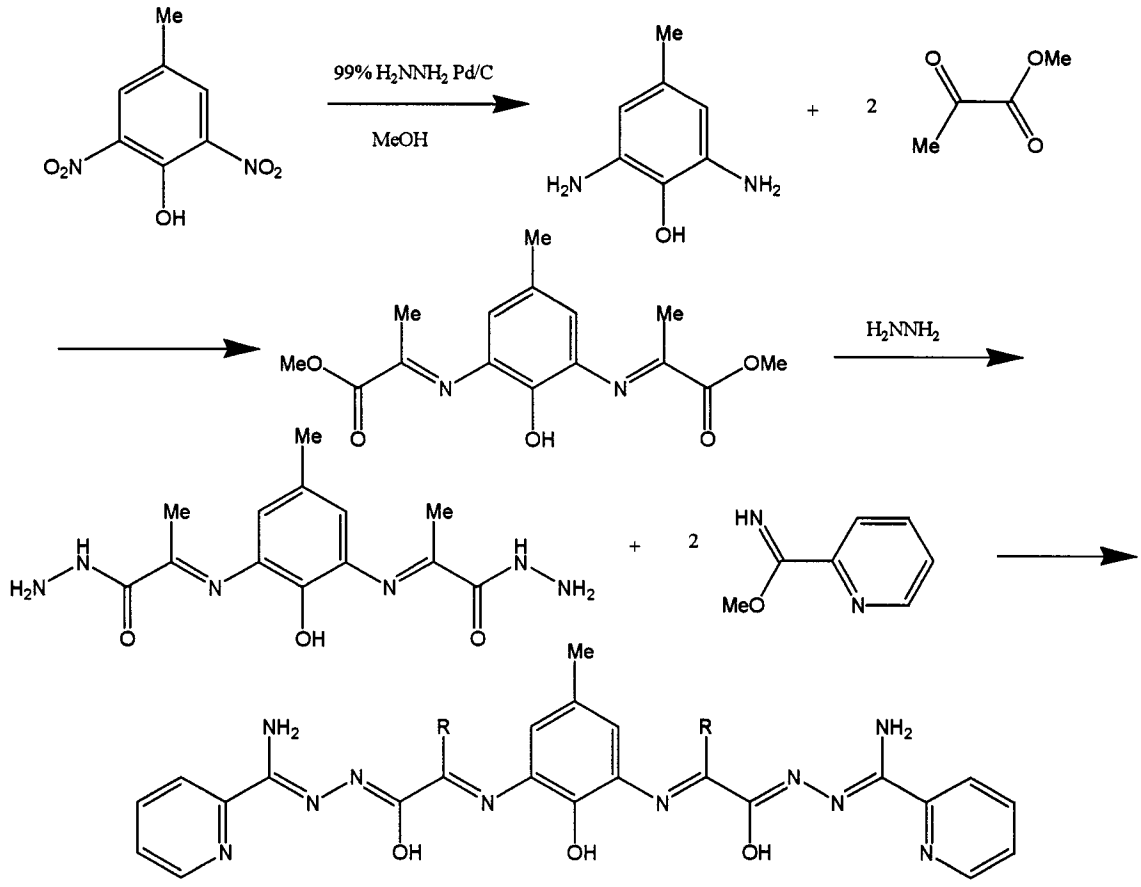

Scheme 7. Attempted synthesis of potential [4×4] grid forming ligand.

2,6-Dinitro-*p*-cresol (12.075 g, 0.060943 mol) was partially dissolved in absolute ethanol (100 mL). Palladium on activated carbon (3.17 g) suspended in absolute ethanol (40 mL) was added and the mixture refluxed under a stream of N_2. Anhydrous hydrazine (11.3 g, 0.352 mol) dissolved in absolute ethanol (25 mL) was added dropwise. The drop rate and temperature were monitored, since the mixture frothed due to hydrogen and nitrogen gases being produced. After refluxing overnight, the hot solution was filtered to

remove the catalyst, and then allowed to cool. The volume was reduced to roughly 25 mL using a rotary evaporator and concentrated hydrochloric acid was added dropwise resulting in the formation of a grey precipitate of the 2,6-*p*-diamino cresol hydrochloride salt (12.4 g, 58.9 mmol; Yield = 65%; Mass Spectrum; M/z 138 (M^+), 93, 36. FT-IR (υ in cm^{-1}) υ(NH) 3582, 3518, υ(OH) 3171). The identity of the 2,6-*p*-diamino cresol hydrochloride salt was confirmed through the appearance of NH_2 bands in the FT-IR spectrum, as well as the molecular ion peak in the mass spectrum.

Further attempts to continue the synthesis by performing a Schiff-base condensation between the aromatic amines of the 2,6-diamino-*p*-cresol and the ketonic carbonyl of the methyl pyruvate were unsuccessful. These attempts included the use of heat, acid catalyst, the 2,6-diamino-*p*-cresol in its protonated, neutral deprotonated and basic forms, and combinations of these conditions, no identifiable products were obtained.

2PzOAP

Another interesting ligand would be the pyrazine analogue of 2POAP, 2PzOAP as shown in Fig. 35.

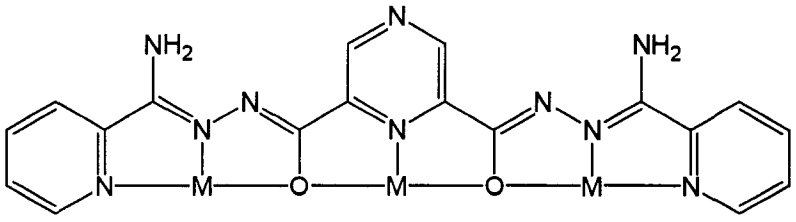

Fig. 35. 2PzOAP showing potential metal binding mode.

It is often quite informative to compare analogous complexes of these types of ligands in which pyridine moieties have been replaced with pyrazine. Often the effect is less a chemical one, in which the ultimate structure of the final complex formed is unchanged, but rather an electronic one in which the altered electronic properties of the pyrazine ring as compared to the pyridine ring may affect the magnetic exchange of the metals in the complex. However the fact that the second N atom on the pyrazine ring is an appropriate electron donor does allow the possibility of another coordination mode in addition to those found in the 2POAP grids. Should a grid be formed from this ligand, this additional donor would be well-situated to allow the potential for intermolecular interactions between adjacent grids, perhaps mediated by additional metal cations or hydrogen bonding interactions with solvent molecules.

The synthetic strategy is outlined in Scheme 8.

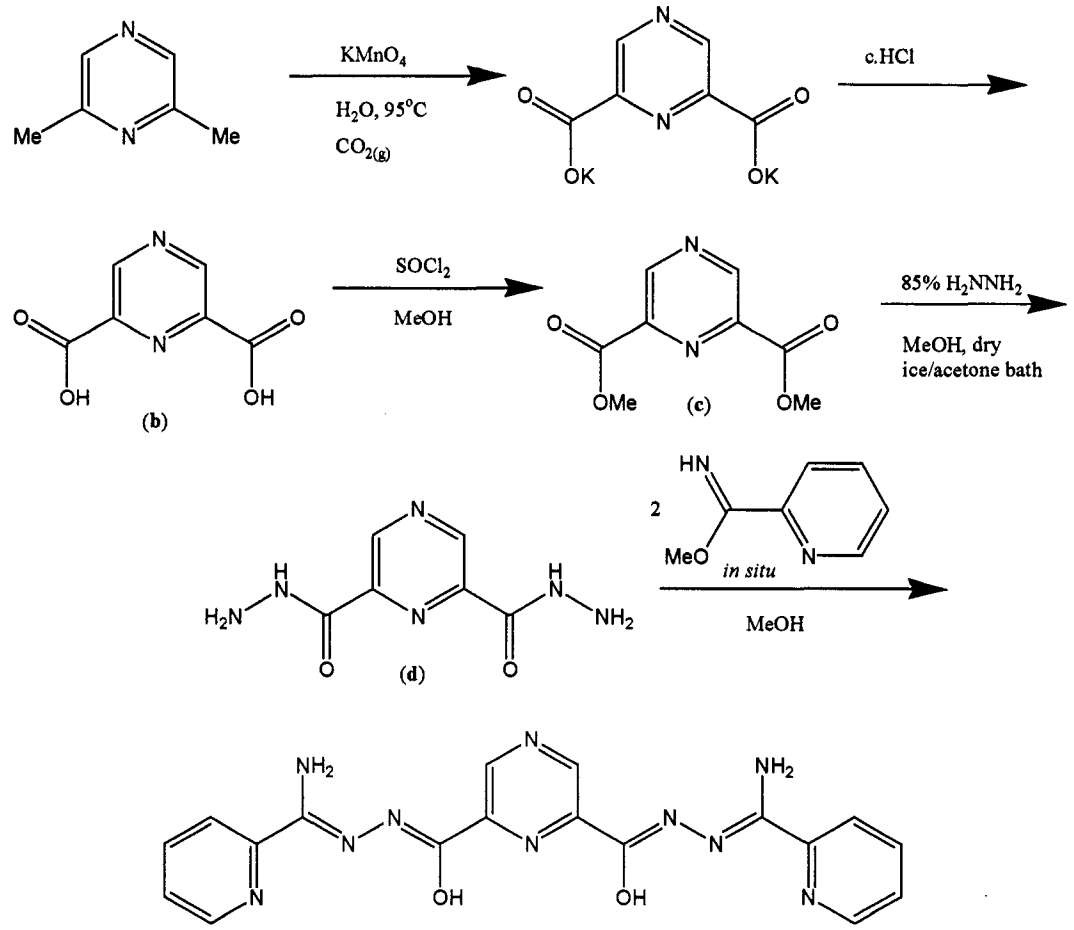

Scheme 8. Attempted synthesis of 2PzOAP.

2,6-Dimethylpyrazine (9.06 g, 0.0838 mol) was dissolved in water (200 mL). Carbon dioxide gas was bubbled through in a constant stream during the course of the reaction. After heating the solution to 85°C, potassium permanganate (26.5 g, 0.168 mol) was added in small amounts, monitoring the temperature such that it was maintained between 90-95°C. After the complete addition of potassium permanganate, the temperature was maintained in the 90-95°C range for a further two h, at which time the solid manganese dioxide was filtered off and the volume of the resulting colourless

solution was reduced to less than 50 mL on a rotary evaporator. Concentrated HCl was added while the flask was cooled in an ice water bath. During the addition of HCl, CO_2 gas was evolved. When the pH was slightly acidic, EtOH was added dropwise with the formation of a white solid. The product (**b**) was collected by suction filtration and washed with cold EtOH. (Yield = 14.8 g (90.7%); mp: >260°C; Mass Spectrum; M/z 168 (M^+), 108, 94, 80. FT-IR (υ in cm^{-1}) υ(CO) 1710. ^{1}H-NMR (300MHz, D_6-DMSO, 25°C, δ in ppm): δ 8.8 (s, 1H, py), 8.4 (s, 1H, py)).

The evidence quite strongly favours the formation of the acid (**b**) from the dimethyl pyrazine; in particular the melting point has changed by a difference of over 200°C compared with the starting material. Furthermore the mass spectrum shows the molecular ion peak for the diacid at 168, and there are no methyl proton resonances in the ^{1}H NMR. Finally, there is the appearance of a CO band in the FT-IR at 1710 cm^{-1}. All these observations are consistent with the product and inconsistent with the dimethyl pyrazine starting material.

2,6-Pyrazine dicarboxylic acid (**b**) (2.78 g, 0.0159 mol) was suspended with stirring in 100 mL of methanol and cooled in an acetone-dry ice bath. Thionyl chloride (6.30 g, 0.0534 mol) was added dropwise at a rate of roughly one drop per second. The mixture was allowed to stir overnight as the bath warmed to room temperature. The insoluble white diester (**c**) was collected by suction filtration (Yield = 2.4 g (90%); mp: >260°C; Mass Spectrum; M/z 197 (MH^+), 184, 124, 87, 43. FT-IR (υ in cm^{-1}) υ(CO) 1731. ^{1}H NMR, insoluble product).

The limited evidence suggests the formation of the dimethyl pyrazine-2,6-dicarboxylate (**c**) from the 2,6-pyrazine dicarboxylic acid. The melting point remains above the upper limit of the melting point apparatus, although one would expect it to be lower than the diacid. The mass spectrum shows the molecular ion peak of the protonated dimethyl pyrazine-2,6-dicarboxylate (**c**) at 197 M/z, and the CO band in the FT-IR has been shifted to higher energy as is the case when acid carbonyl bands are compared with those of the esters. Unfortunately the poor solubility of the product in common solvents prevented the acquisition of an ^{1}H NMR spectrum.

The putative dimethyl pyrazine-2,6-dicarboxylate (**c**) was suspended with stirring in methanol (50 mL) and cooled in an ice-water bath. Hydrazine hydrate (85%) dissolved in methanol (10 mL) was added slowly and the mixture was stirred overnight, allowing the bath to warm to room temperature. The white solid was identified as the dimethyl ester (**c**), indicating that the reaction to produce the corresponding dihydrazide (**d**) was unsuccessful. The attempted synthesis of 2PzOAP was abandoned at this point.

Chapter 4. Complex Synthesis and Discussion

4.1. General Comments on Spectral Information

There are a number of diagnostic regions of the infrared spectrum which are helpful for analysis of the complexes formed with this type of ligand. Since all ligands have a carbonyl oxygen, any changes in the electron density of the carbonyl group(s), for example when it coordinates, will be easily seen as a variation in the characteristic carbonyl stretch in the infrared spectrum. The location of this band in the spectrum of the free ligand varies with the particular ligand used, and usually occurs in the 1600-1800 cm^{-1} region, in the lower range of which the C=N bands of the ligand appear. Upon coordination and bridging of metal cations by the carbonyl group, the distinctive band is shifted to lower energy.

The characteristic ring breathing mode vibration of the pyridine ring which is usually found close to 990 cm^{-1} will be shifted to higher energy when the pyridine nitrogen interacts with a metal. Unfortunately, this band is often obscured by anion absorptions. For instance, perchlorate and tetrafluoroborate anions have strong broad bands in this region, which will completely obscure the diagnostic pyridine band.

4.2. Complex Syntheses

$\underline{(\text{di-OAOP Ni}\cdot 2.5H_2O)_n}$ **(1)**

$Ni(BF_4)_2\cdot 6H_2O$ (1.43 g, 4.19 mmol) was dissolved with stirring in methanol (50 mL). Di-OAOP (0.317 g, 0.641 mmol) was added with ten drops $(t\text{-Bu})_3N$. The mixture was stirred and refluxed for roughly 15 h, during which time the product formed as an insoluble light green powdery solid (Yield = 0.249 g (65%); Anal. Calcd. for $C_{27}H_{20}N_6O_4Ni\cdot 2.5H_2O$: C, 54.36; H, 4.56; N, 14.10. Found: C, 54.43; H, 4.10; N, 13.64. FT-IR (υ in cm^{-1}) υ(CO) 1661, υ(CN) 1623, υ(CN) 1580, υ(py) 997. UV-VIS (λ in nm) 410, 609, 968).

$\underline{\text{di-OAOP } Cu_2(BF_4)_2(H_2O)_5}$ **(2)**

$Cu(BF_4)_2\cdot 6H_2O$ (0.948 g, 4.00 mmol) was dissolved in methanol (50 mL). Di-OAOP (0.335 g, 0.678 mmol) was added forming a green suspension followed by 15 drops of $(t\text{-Bu})_3N$ and the mixture refluxed overnight. The product was collected as an insoluble green solid (Yield = 0.532 g (89%); Anal. Calcd. for $C_{27}H_{20}N_6O_4Cu_2(BF_4)_2(H_2O)_5$: C, 37.31; H, 3.71; N, 9.67; Cu, 14.62. Found: C, 37.33, H, 2.98; N, 9.37; Cu, 16.64. FT-IR (υ in cm^{-1}) υ(CO) 1621, υ(CN) 1579, υ(CN) 1548, $\upsilon(BF_4^-)$ 1017. UV-VIS (λ in nm) 411, 691).

$\underline{[(\text{Cl2POAP})_6\text{Fe(II)}_8\text{Fe(III)}](ClO_4)_8\cdot 23H_2O}$ **(3)**

All reactions and manipulations were carried out in an atmosphere of N_2 gas. Cl2POAP (0.800 g, 1.83 mmol) was suspended in acetonitrile (10 mL) with stirring in a 100 mL round-bottomed flask. $Fe(ClO_4)_2\cdot 6H_2O$ (2.76 g, 7.60 mmol) was dissolved in acetonitrile (40mL) in a second 100 mL round-bottomed flask with stirring. Metallic iron

powder (0.450 g, 8.06mmol) was added and the flask flushed with N_2. When the colour of iron(III) impurities faded to form a colourless solution of iron(II) under the reducing action of the metallic iron, the solution was filtered through a glass U-tube into the flask containing the Cl2POAP. A very dark red solution formed immediately and was heated in a warm water bath to roughly 80°C, with stirring for 2 h and then stirred overnight at room temperature. The solution volume was reduced to roughly 25 mL and 4 mL of chloroform was added. The sealed round-bottomed flask, still under N_2, was allowed to stand at room temperature for a week during which time very dark crystals formed. These were collected by suction filtration and washed with a small amount of ice-cold 50/50 acetonitrile/chloroform solution (Yield = 0.90 g (67%); Anal. Calcd. for $[(C_{19}H_{14}N_9O_2Cl)_6Fe(II)_8Fe(III)](ClO_4)_8 \cdot 23H_2O$: C, 31.64; H, 3.03; N, 17.48; Cl, 11.47. Found: C, 31.65; H, 2.33; N, 17.37; Cl, 11.45. MALDI-TOF MS M/z = 3111 (M^+, $[(Cl2POAP\text{-}3H)_6Fe(II)_8Fe(III)]^{+1}$), 3056 ($[CL2POAP_6\text{-}15H^+Fe_8]$), 1037 ($[(Cl2POAP)2\text{-}8HFe3]^{+1}$). FT-IR ($\upsilon$ in cm^{-1}): υ(NH) 3317, 3164, υ(CO) 1653, υ(CN, m) 1541, $\upsilon(ClO_4^-)$ 1079).

<u>$(P2OAP)_4Ni_4 \cdot 12H_2O$</u> (**4**)

$Ni(BF_4)_2 \cdot 6H_2O$ (0.954 g, 2.803 mmol) was dissolved in methanol (10 mL). P2OAP (0.232 g, 0.599 mmol) was dissolved in dimethyl formamide (10 mL) forming a yellow solution. The two solutions were combined with the immediate formation of a very dark red-orange solution. After allowing the solution to stand overnight, the product formed as a dark red solid. The product was collected by suction filtration, washed with ice-cold methanol and diethyl-ether and dried (Yield = 0.245 g (77%); Anal. Calcd. for

$(C_{20}H_{17}N_7O_2)_4Ni_4 \cdot 12H_2O$: C, 48.03; H, 4.63; N, 19.60; Ni, 11.37; Found: C, 48.10; H, 4.06; N, 19.59; Ni, 12.41. FT-IR (υ in cm^{-1}) υ(NH) 3311, υ(NH) 3284, υ(CO) 1666, υ(CN) 1607, υ(CN) 1536 (py) 1002. UV-VIS (λ in nm) 411, 691).

4.3. Complex Discussion

$[(di\text{-}OAOP)Ni(H_2O)_{2.5}]_n$ (**1**)

The infrared spectrum of the complex is very similar to that of the ligand, showing major absorptions at 1661 cm^{-1} (1661 cm^{-1} in the free ligand) corresponding to the carbonyl, at 1623 cm^{-1}, 1580 cm^{-1} (1623 cm^{-1} and 1580 cm^{-1} in the free ligand) corresponding to the CN bonds, and at 997 cm^{-1} (998 cm^{-1} in the free ligand) indicating an uncoordinated pyridine band. Thus, the indication is that none of these groups are involved in the binding of the ligand to the nickel cation. Very significantly, the lack of the characteristic strong tetrafluoroborate peak at 1055 cm^{-1} shows that this group is absent and the ligand alone acts as an anion. This must occur through proton loss at the phenolic OH group.

The UV-VIS spectrum of **1** shows three bands at 410 nm, 609 nm, and 968 nm, which correspond to spin-allowed transitions from the $^3A_{2g}$ ground state of octahedral Ni(II) to the $^3T_{2g}$, $^3T_{1g}(F)$, and $^3T_{1g}(P)$ levels respectively, which are usually observed in the ranges of 370-525 nm, 500-900 nm, and 770-1400 nm, indicating that the Ni(II) cations are in an octahedral coordination environment.[72]

The profile of magnetic moment versus temperature is striking (Fig. 36), showing a large rise in the magnetic moment, beginning at about 50K to a maximum value approaching 15.5 μ_B at 14K followed by a sharp drop to 3.8 μ_B at 2K. The room temperature magnetic moment of this compound, 3.41 μ_B is high when compared with the spin only value for nickel of 2.83 μ_B, but considering the strongly ferromagnetically-coupled nature of this complex (*vide infra*) is reasonable.

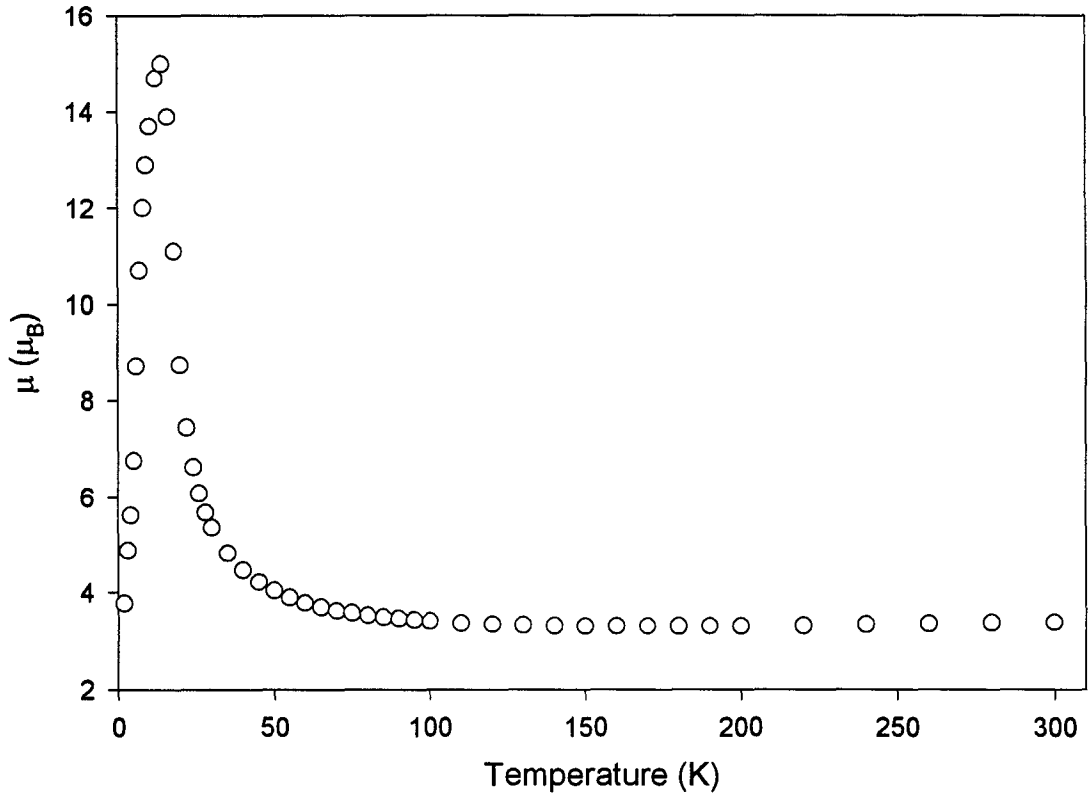

Fig. 36. μ (μ_{BM}) vs. Temperature (K) for **1**. (DC Field = 0.1T)

Proposed Structure

It has been demonstrated that the geometry of the metal cations and bridge can have large consequences for the type and strength of the magnetic interaction between metal cations. Specifically, for nickel cations bridged by phenolic oxygen atoms, it has been demonstrated that at bridging angles of less than 97° ferromagnetic coupling occurs, while at angles greater than 97° antiferromagnetism occurs.[73] Since a phenolic group is present in the ligand and is likely to act as a ligand, it would be logical to propose a

structure in which the ferromagnetic interaction arises from a bridging phenolic interaction with a small Ni-O-Ni angle.

The proposed structure for this compound which fits the physical evidence obtained is of a series of stacked polymeric chains as shown in Fig. 37 and Fig. 38.

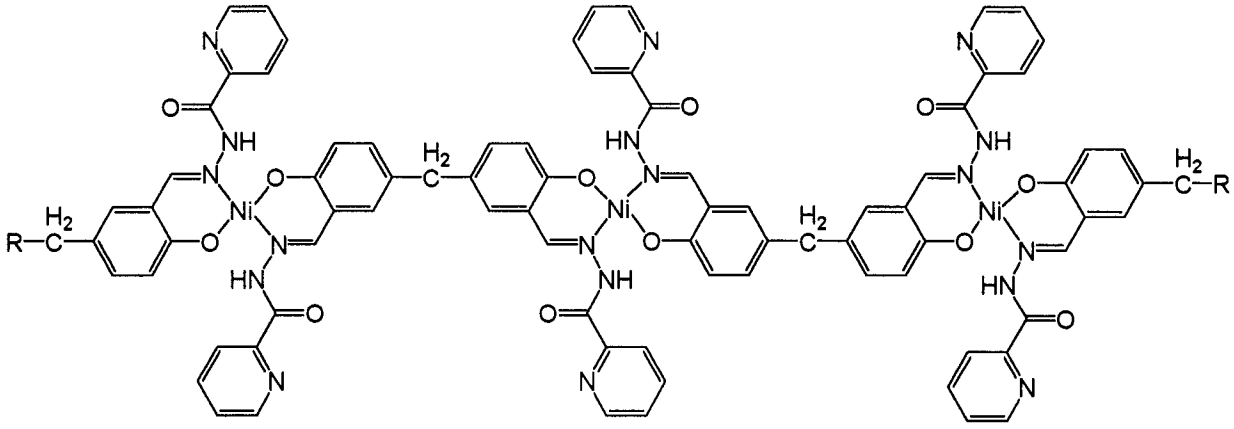

Fig. 37. **1** Polymeric Chains.

In this proposed structure the nickel cations are bound to two ligands with a planar arrangement of two phenolic oxygen atoms, and two nitrogen atoms from the adjacent imine as suggested from the FT-IR spectrum. The carbonyl and pyridine moieties are not involved in bonding since their characteristic infrared bands are unchanged from those of the free ligand.

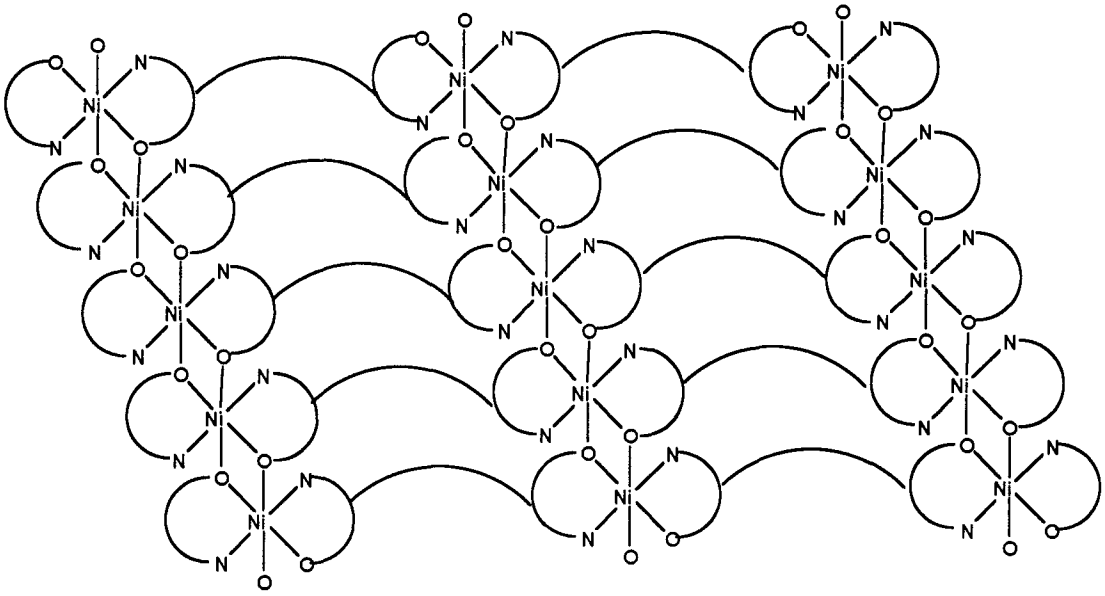

Fig. 38. Stacking of polymeric nickel chains in **1** forming 2D sheets along the directions indicated.

The remaining two positions required to satisfy the coordination geometry of the octahedral nickel cation, as is indicated from the UV-VIS spectrum, could occur through stacking of the polymeric chains forming sheets, such that the nickel cations are bridged by the phenolic oxygen atoms as shown in Fig. 38. The Ni-O-Ni angle in this case would have to be less than 97° in order for a ferromagnetic interaction to occur.

This type of stacking would allow the ordering of a large number of Ni(II) cations through the chain of Ni-O-Ni bonds, necessary in order to explain the large ferromagnetism observed. The magnetic properties of **1** are quite reminiscent of the chain Ni(II) hydroxynitrate systems prepared by Drillon.[74] Drillon's system shows an initial dominant in-chain ferromagnetic interaction with a maximum moment of 8.7 μ_B at 9 K, followed by a drop in moment below this temperature due to either the population of

a non-magnetic ground state or due to single-ion anisotropy. These systems, though displaying similar magnetic properties to **1**, have a maximum value of μ about half of **1**.

Drillon's $Ni(OH)(NO_3)H_2O$ compound consists of an infinite double chain of nickel(II) cations involving two exchange interactions mediated by O bridges. These interactions consist of an along the chain (J2) as well as a cross-chain interaction (J1) in which each nickel cation is coupled with two partners on the adjacent chain (see Fig. 39).

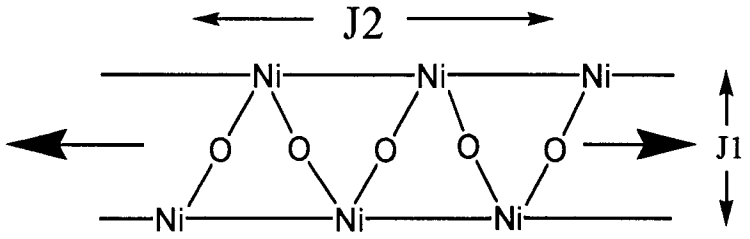

Fig. 39. Schematic representation of the coupling interaction of the zigzag double chain of $Ni(OH)(NO_3)H_2O$.

In the proposed "sheet" model for **1**, the magnetic situation is of single magnetic chains of Ni(II) cations. Although the "chains" are physically linked by the ligands, there will be no ligand-mediated magnetic exchange between them due to the distances involved as well as the lack of a suitable exchange pathway along the ligand. Although the proposed structure is of a 2-D sheet, the magnetic situation is that of isolated chains of Ni(II) cations.

Concern that this compound might represent a type of nickel hydroxide polymer with no involvement by the di-OAOP ligand was eliminated by a repeat of the reaction conditions for preparing **1** but in the absence of the ligand. No product was observed. Furthermore the conditions used to prepare $[Ni(OH)(NO_3)H_2O]$ involve the use of

aqueous 10 M NaOH and higher temperatures (12 h at 95°C) than were involved in the synthesis of **1**.

DC Susceptibility Measurements

As previously mentioned, in the proposed structure, direct spin exchange would be anticipated only along the chains, and not between chains in the sheet arrangement. Therefore a 1-D chain model would seem appropriate.

The gradual rise in moment (per Ni centre) from 3.41 μ_B at 300 K to 15.5 μ_B at 14 K is indicative of quite strong ferromagnetic exchange. Due to the magnitude of the ferromagnetic exchange, it is reasonable to associate this with an interchain ferromagnetic interaction in addition to an intrachain ferromagnetic interaction. The sharp drop in moment below 14 K is indicative of a long range antiferromagnetic exchange term, possibly between the sheets of chains (Fig. 40).

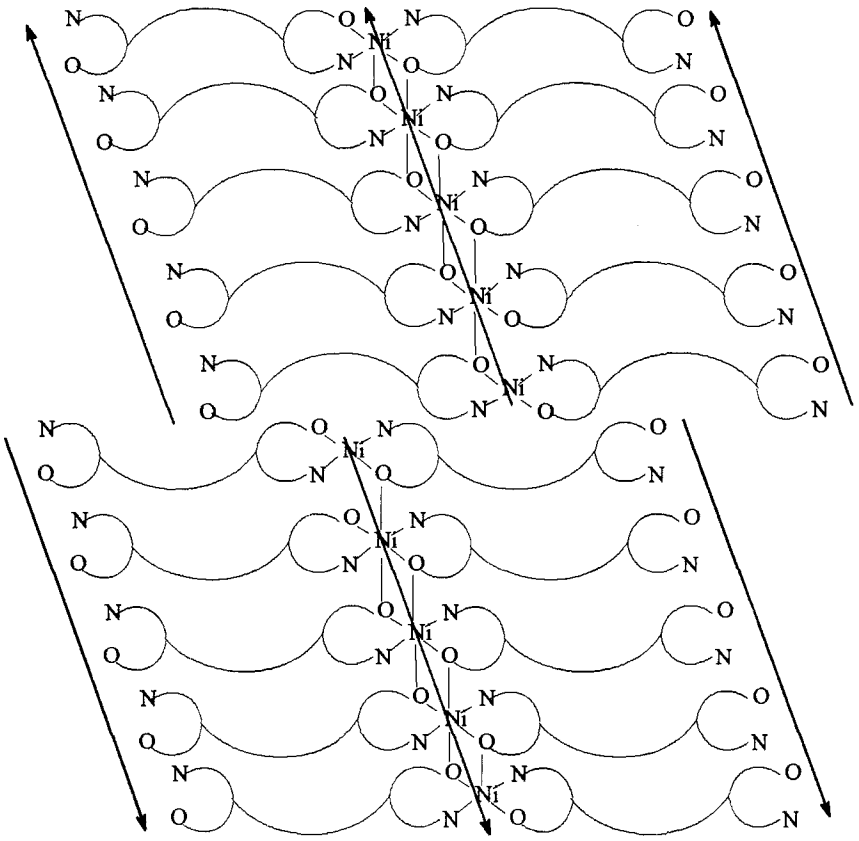

Fig. 40. Antiferromagnetic coupling of 2D sheets with ferromagnetic coupling between chains within a sheet.

This interpretation of **1** as a metamagnet in which two types of interactions, ferromagnetic and antiferromagnetic are present, is supported by a series of magnetic profiles taken at varied field strength. It is well-known that ferromagnetism is a field-dependent interaction, while antiferromagnetism is field independent. With increasing applied field strength in the range 5 to 30K, the maximum in the moment becomes significantly reduced, as seen in Fig. 41. This is a result of the large field prealigning the ferromagnetic chains such that the chain alignment is effectively destroyed. The maximum attained in these profiles of 25 μ_B at lower field strengths corresponds to

roughly 64 nickel centres aligned together forming a single magnetic domain. This allows a very rough estimate of the degree of cooperativity involved in **1**.

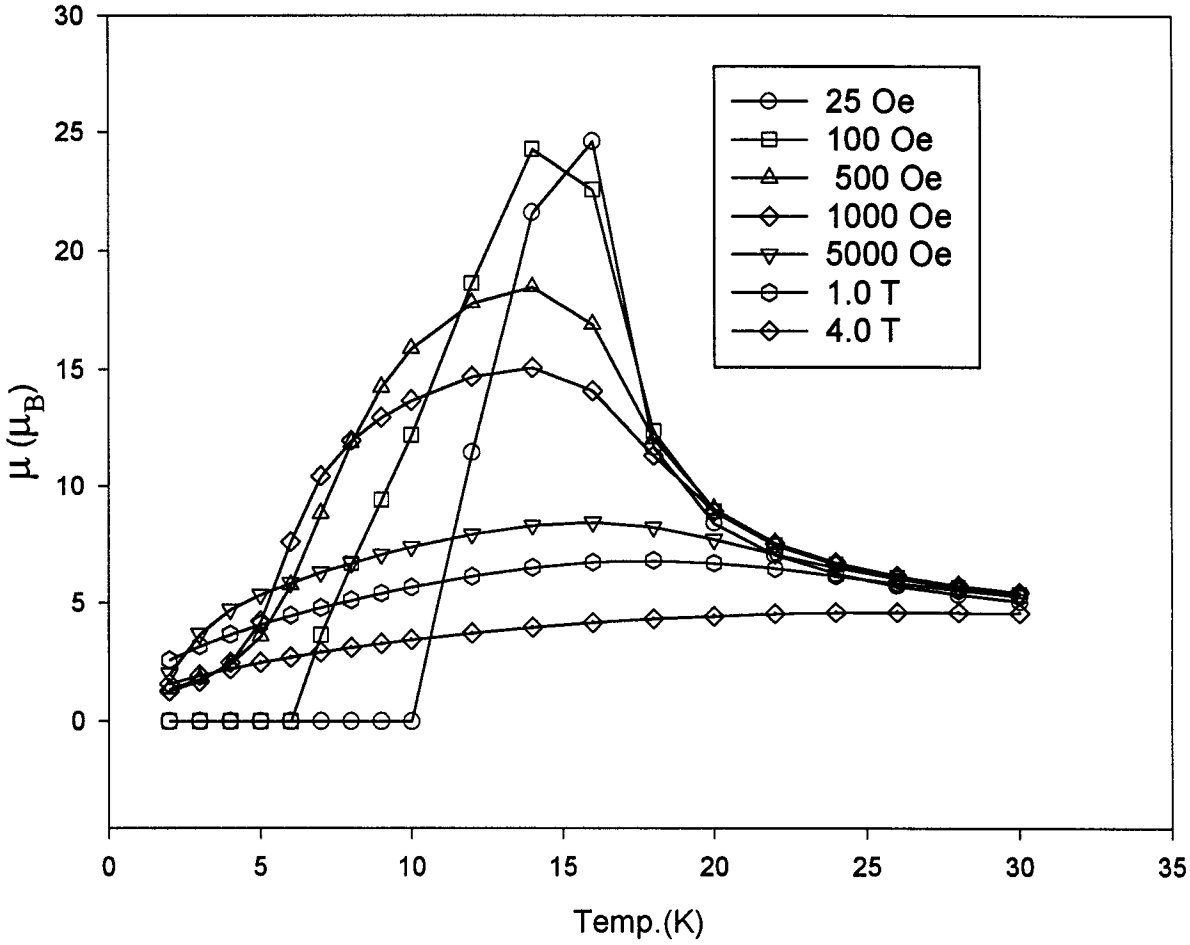

Fig. 41. Variable temperature data (μ) at low temperatures as a function of external field.

Another way of observing this metamagnetic behavior is through the temperature-dependence of the magnetization M at various fields, as shown in Fig. 42. For values of the applied field less than 1 T the M vs. T curves show a maximum at roughly 14 K, revealing an interchain antiferromagnetic coupling. The maximum in M disappears as

the applied field reaches 1 T as the field overcomes the interchain antiferromagnetic interaction and the compound behaves in a ferromagnetic fashion.

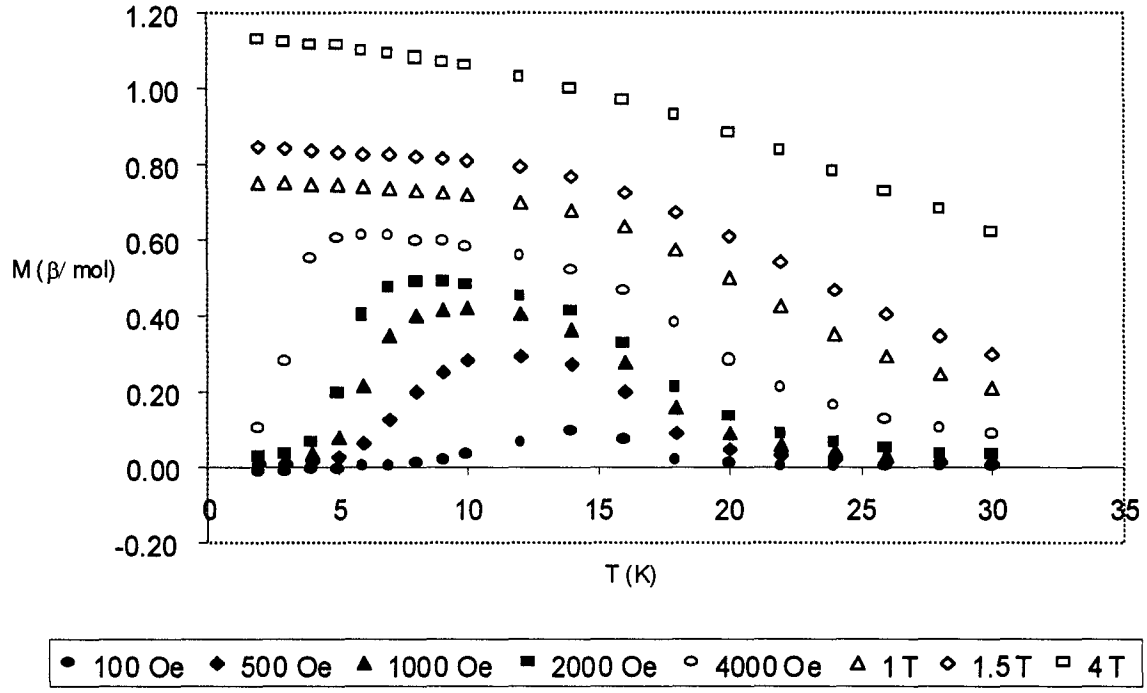

Fig. 42. Magnetization data at low temperature as a function of external field.

A remarkable property of **1** is the strong, well-defined hysteresis that is observed, Fig. 43 shows the hysteretic loop from which one can observe the remnant magnetization of 0.54 Nβ and the coercive field of 0.54 T. Generally magnets with coercive fields $H_C >$ 1000 Oe are considered "hard" magnets, while those with $H_C <$ 1000 Oe are considered "soft" magnets. With **1** having an H_C = 5400 Oe (1 T = 10000 Oe), it is clearly a "hard" magnet.

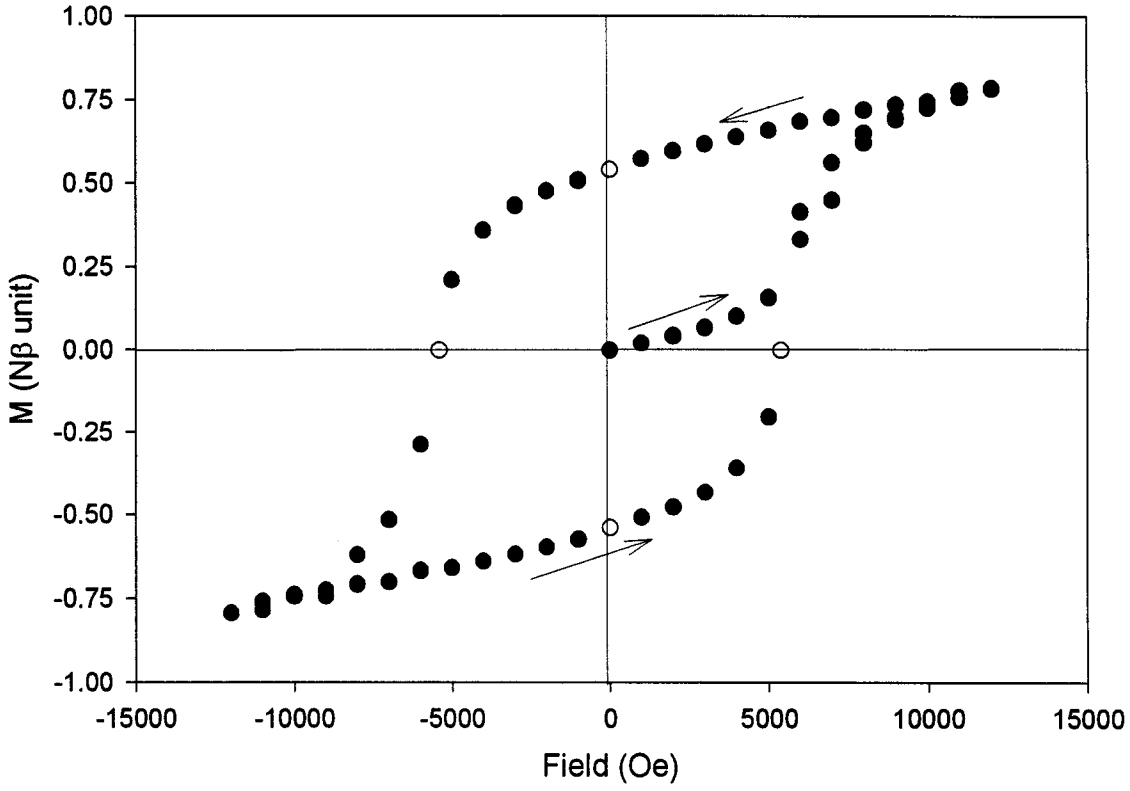

Fig. 43. Hysteresis of the magnetization for **1** measured at 2 K.

AC measurements on **1** show a peak in the out-of-phase signal (μ'') at roughly 14 K, corresponding to the temperature at which we see the beginning of the strong cooperative ferromagnetic interaction (see Fig. 44). This is a result of the barrier to reorganization of the magnetic moment present in a molecular based magnet. This energy barrier to the reorganization of the magnetic moment is the basis of the ability of a magnet to retain a bulk magnetic dipole in the absence of an external field, and therefore its ability to store data.

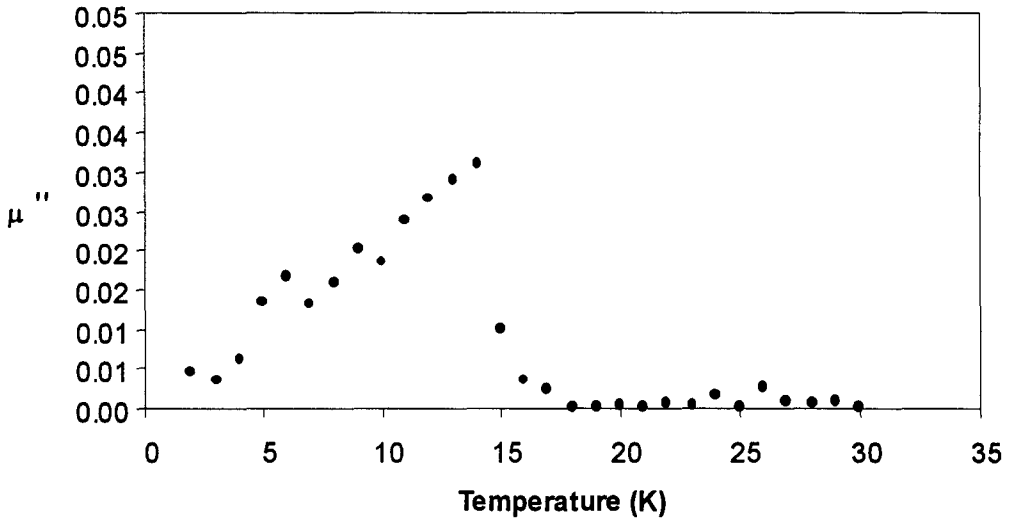

Fig. 44. AC susceptibility of **1** (DC field = 0 T, Amplitude = 3.5 Oe, Frequency = 100 Hz).

The critical temperature of this system, the temperature below which it behaves as a molecular magnet, has been determined through field-cooled, zero-field cooled measurements. These were undertaken through cooling the sample in zero-field conditions to 2 K and returning to 26 K (a point chosen to be above T_C) at which point an external DC field of 100 Oe was applied and the sample cooled to 2 K. Finally the field was switched off and the sample was warmed to 26 K.

Under these conditions a magnetic material will display a spontaneous magnetization at T_C in zero-field, leading to a weak maximum in magnetization as magnetic domains are aligned. In the field-cooled run the magnetization will increase abruptly at T_C reaching a higher plateau at low temperature. Finally as the sample is warmed after the external field is turned off the magnetization will follow the field-

cooled magnetization then return to zero above T_c as thermal energy causes spin randomization. This behavior is observed for **1** (see Fig. 45).

From this data it is easy to observe the critical temperature of 15 K, the point on the zero-field cooled run in which a spontaneous magnetization is observed. This type of spontaneous magnetization is the defining property of a molecular magnet.

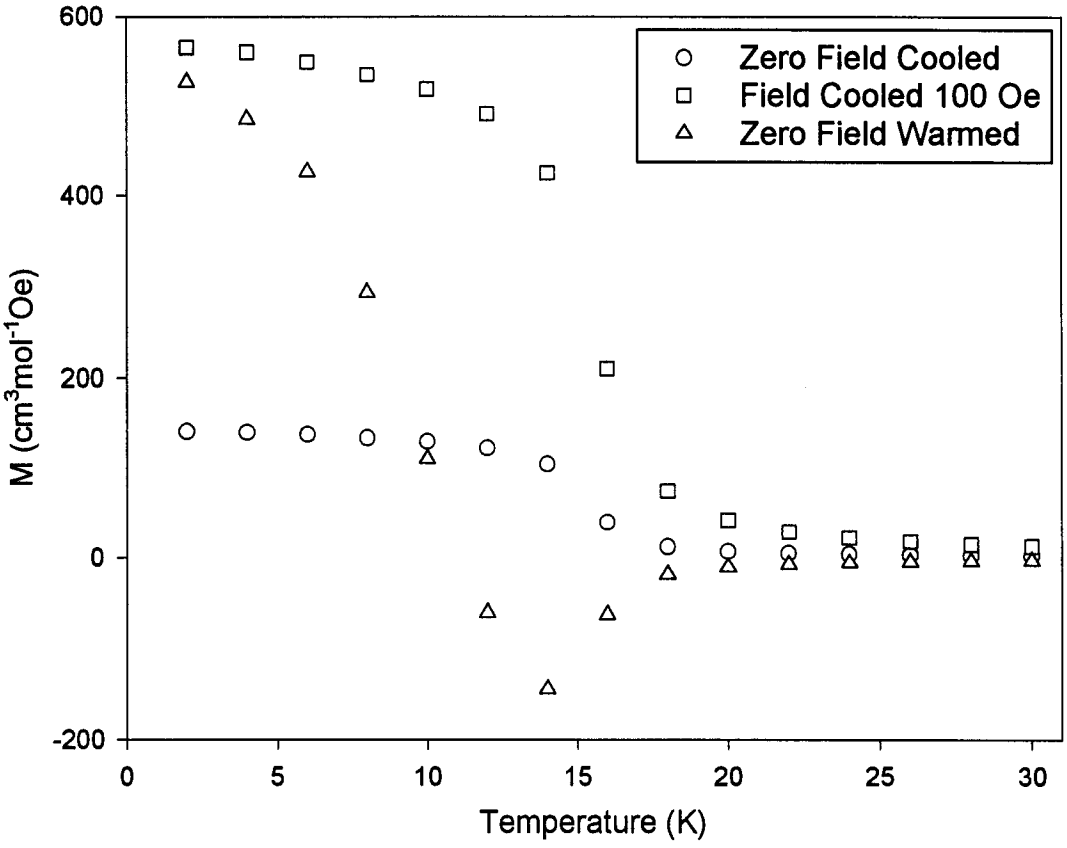

Fig. 45. Cooling under zero-field conditions and 100 Oe.

Magnetization vs. field studies are informative for elucidating the spin states of magnetic systems. Theoretical data plots of various spin states are compared with the data in order to determine which case the data best correspond to (see Fig. 46). In the

case of **1** the data are intermediate between that of S = 2/2 (or S = 1 the combination of two s = ½ electrons) and S = ½, where S is the total electron spin of the system. One would expect a total spin of S = 1 for nickel, were there no antiferromagnetic effect, so this indicates that neither type of magnetic interaction (ferromagnetic and antiferromagnetic) dominates. However in the ground state the antiferromagnetic interaction is significant.

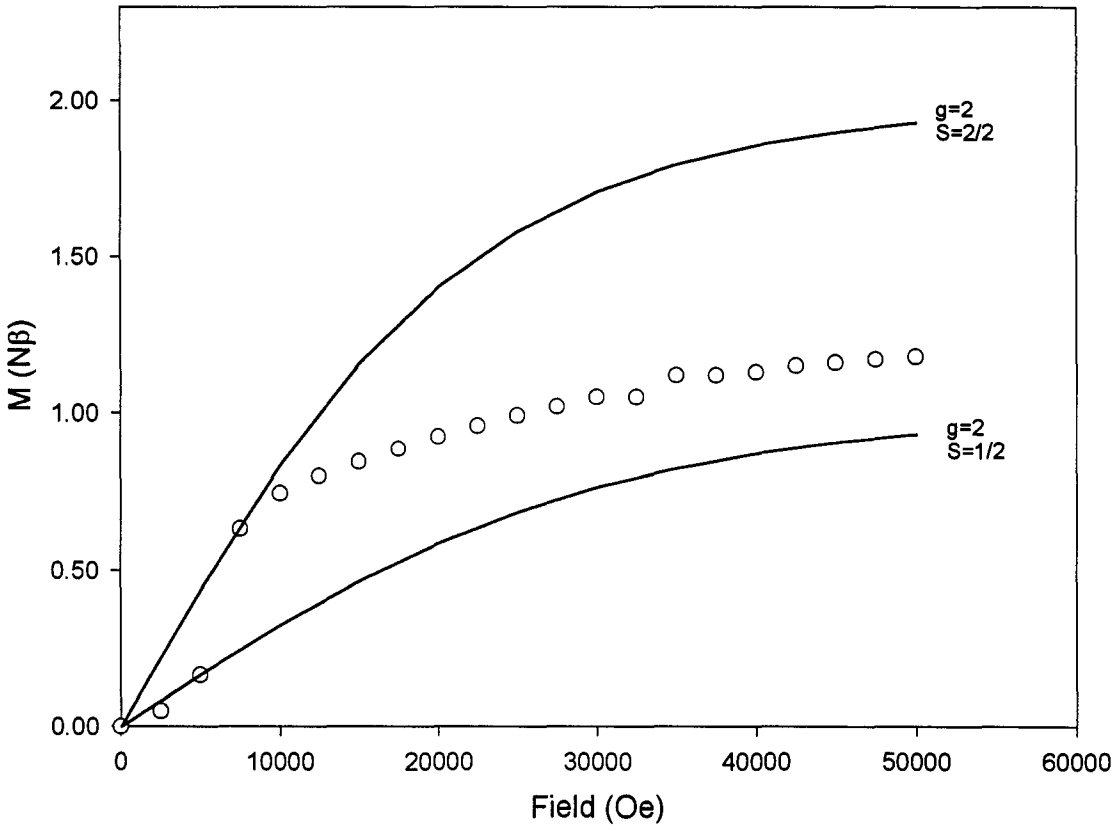

Fig. 46. Magnetization vs. field for **1** at 2 K.

A second measurement with a larger number of data points in the low field region is illustrated in Fig. 47 which allows one to more easily observe the point of inflection

which corresponds to the field-induced transition from an antiferromagnetic to a ferromagnetic state.

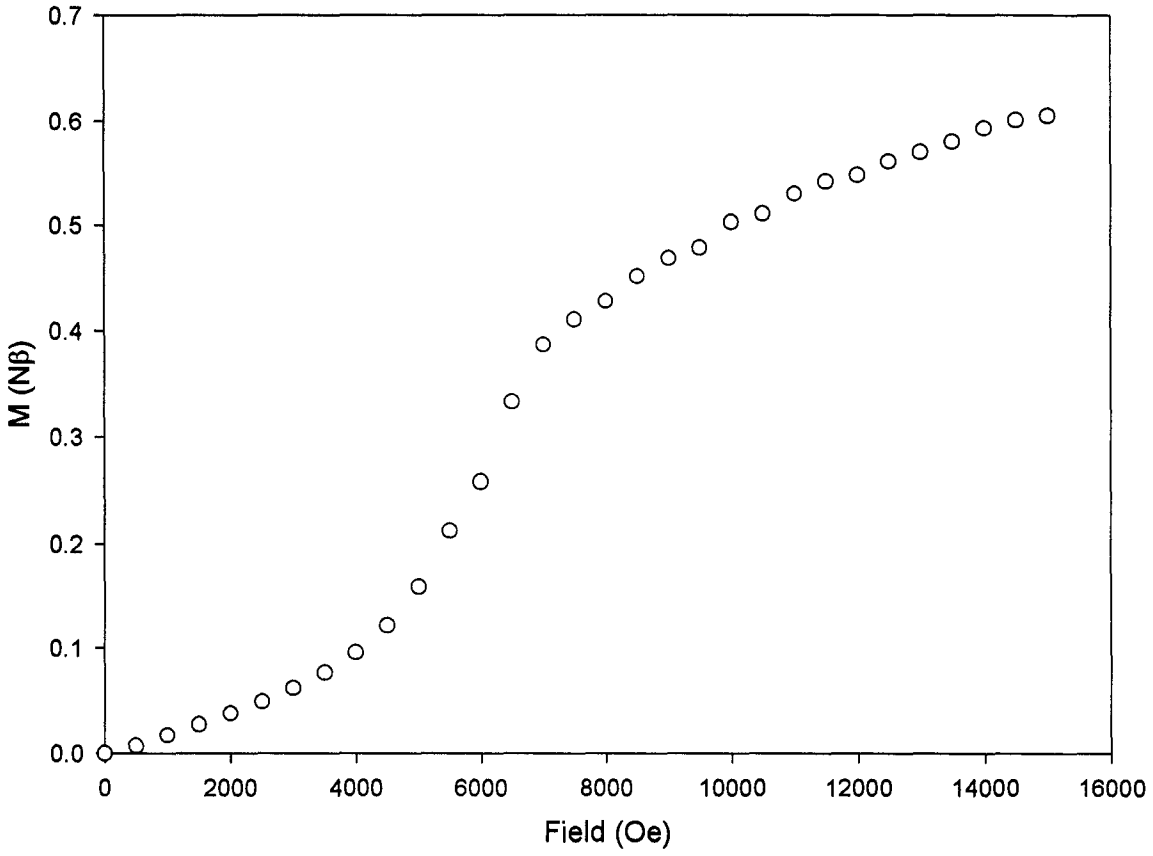

Fig. 47. Magnetization vs. field for **1** at 2 K in the low field region.

The crossover between states can be clearly seen in a plot of the first derivative (Fig. 48) δM/δH vs. Field (Oe) which clearly shows a maximum at 0.6 T corresponding roughly to the coercive field and is highly indicative of metamagnetic behavior in which both ferromagnetic and antiferromagnetic behavior is present.

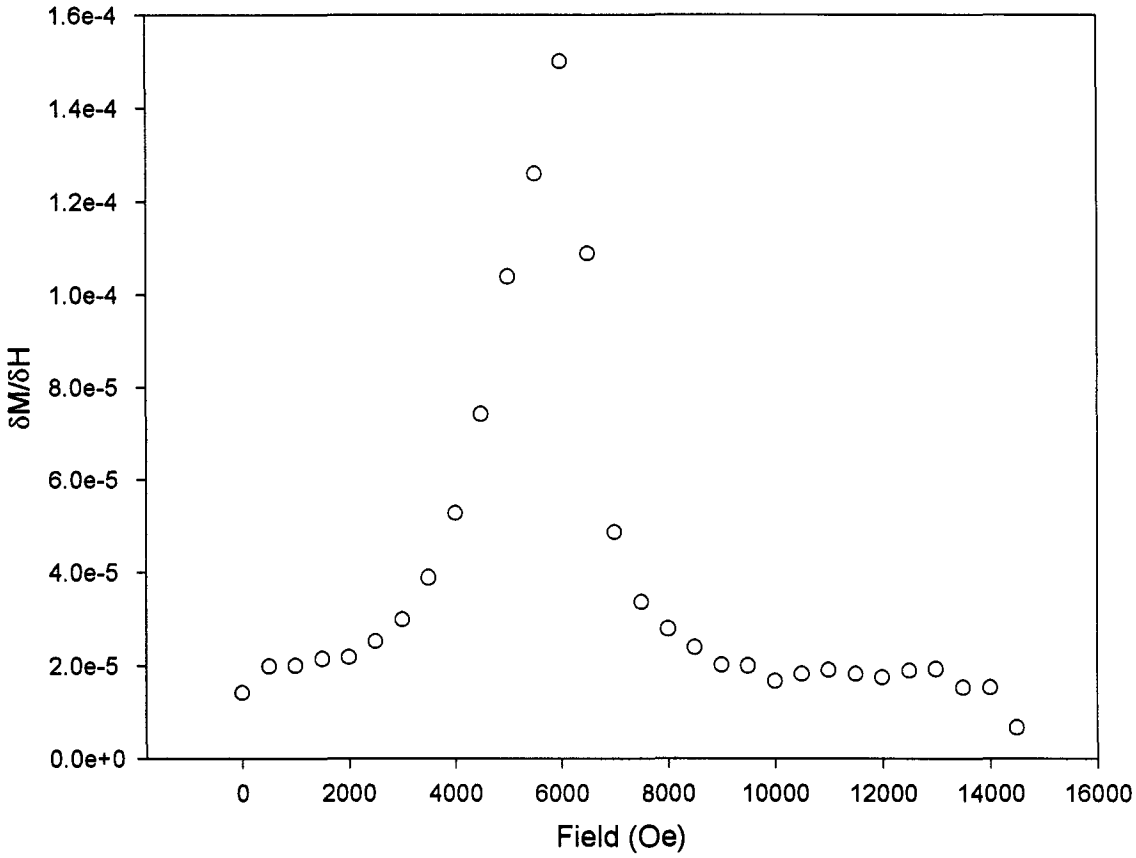

Fig. 48. δM/δH vs. Field (Oe) at 2 K for **1**.

This compound is easily identifiable as a molecular based magnet. Below the critical temperature it displays magnetic properties similar to a bulk magnet, with a hysteresis effect in the magnetization, and is of a molecular nature being composed of metal cations and ligands. That this compound is not a single-molecule magnet is obvious from the details of the hysteresis, being a smooth curve rather than a series of steps indicating quantum effects from single molecule hysteresis.[51] The reason for this in light of the proposed structure is obvious, the compound is not composed of discrete molecular clusters with no inter-cluster magnetic interactions, but is an extended chain of

Ni(II) cations interacting co-operatively, thus the overall magnetic properties do not reflect a single magnetically-active molecular magnetic property.

The variable temperature magnetic data were fit to the equation for an infinite chain of spins greater than S = ½, derived from work by Kahn[47] and Baldwin,[75] assuming no interaction between the chains where:

$$\chi_m = \frac{Ng^2\beta^2}{3kT} S(S+1)\frac{(1+u)}{(1-u)} \qquad (6)$$

$$u = \coth\left[\frac{(JS(S+1)}{kT}\right] - \frac{kT}{S(S+1)}$$

The fitting of the experimental data (Fig. 49) for **1** to eqn. (6) for T > 35 K gives

g = 2.1
J = 15.2 cm^{-1}
TIP = 200 × 10^{-6} emu
R = 0.040

Here J represents the intrachain exchange integral between Ni(II) cations along the chain and no interchain interaction has been modeled. The factor TIP (temperature independent paramagnetism) has been included in the calculation to account for temperature independent paramagnetism inherent to transition metals. The values of TIP and g are within the normal ranges expected for octahedral Ni(II)..

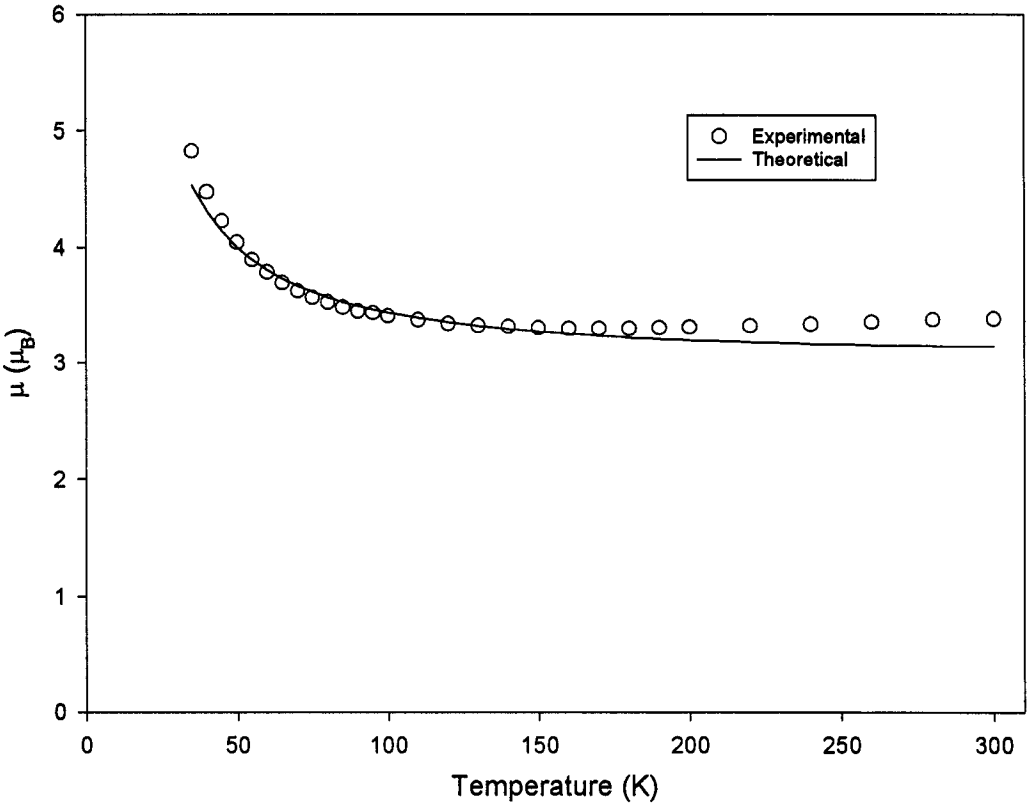

Fig. 49. Variable temperature data for **1** to T = 35 K. The solid line represents the best fit.

Attempts to fit the data to this model at a lower temperature than 35 K results in the experimental data rising much more quickly than the theoretical data (see Fig. 50). This suggests an additional ferromagnetic factor other than along the Ni(II) chains which becomes significant below 35 K. This is most likely a result of through-space ferromagnetic interchain coupling, which has not been accounted for in the initial attempt at modeling the magnetic situation. This through-space interchain coupling is a different effect than ligand-mediated coupling, which has already been discounted due to the lack of a suitable pathway through the ligands connecting the chains. As implied by the name

through-space coupling is not a quantum effect as is ligand mediated spin exchange, but is a classical effect of adjacent magnetic polarities interacting through space.

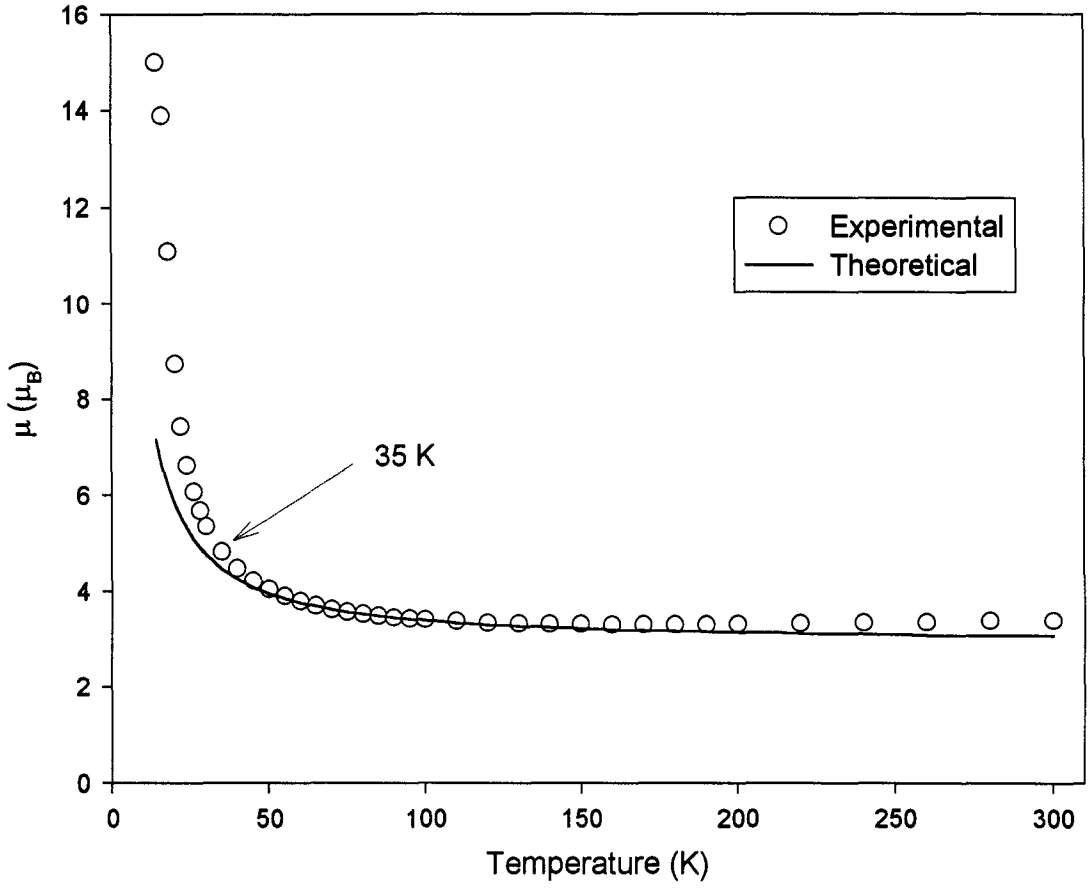

Fig. 50. Variable temperature data for **1** to T = 16 K. Note the deviation of the experimental data from the theoretical data.

In order to account for possible interchain coupling, a two-dimensional approach is called for, applying a chain model to the Ni(II) chains themselves.[76,77] This allows the calculation, at a given temperature, of an effective total spin, S_{eff}, which can be associated with the ferromagnetic chain. S_{eff} can be calculated from the equation

$$S_{eff}(S_{eff} + 1) = 2\chi_{FC}T \quad (7)$$

In which χ_{FC} is the susceptibility calculated for the ferromagnetic chain (FC) by equation (6). For $T < 35K$ the χT values are so large ($\chi T > 2.9$) that S_{eff} takes values large enough that it may be treated as a classical spin. Equation (6) was then used to describe the magnetic susceptibility (χ_{2D}) of this "chain of chains" model with $S_{eff} = 1.96$, the value at $T = 35K$. In this fitting, θ the Weiss-like correction term, represents an interlayer coupling term and will be used to model the low temperature antiferromagnetic term which is believed to be a result of adjacent layers coupling antiferromagnetically.

Fitting the data below 35 K using this approach has been unsuccessful thus far, since correctly modeling the antiferromagnetic term below 16 K has also not been satisfactory. This suggests that a Weiss-like correction is not an appropriate approximation of the antiferromagnetic interaction between layers in this case.

[(di-OAOP)$Cu_2(BF_4)_2(H_2O)_5$] (**2**)

Spectroscopy

Infrared data for **2** are informative, especially when compared with [(di-OAOPNi·2.5$H_2O)_n$]. The infrared spectrum shows a tetrafluoroborate band at 1040 cm^{-1} indicating the presence of tetrafluoroborate anion in the complex, a shift in the ligand carbonyl band from 1661 cm^{-1} in the free ligand to 1621 cm^{-1} in the complex, and the loss of the broad phenolic absorption at 3165 cm^{-1}. Unfortunately the presence of the tetrafluoroborate band obscures the area in which the pyridine breathing mode would be seen, so any potential binding of the pyridine group cannot be determined. The lack of the phenolic band suggests that the ligand behaves as an anion in addition to the tetrafluoroborate anions. Based on this evidence, it would appear that the carbonyl and the phenolic oxygen are involved in coordination to the metal cation.

The UV-VIS spectrum of **2** shows two bands, a more intense narrow band at 411 nm and a very broad less intense band at 691 nm. These bands can be assigned as a charge transfer band and as the result of *d-d* transitions respectively. The *d-d* band is consistent for six coordinate Cu(II) which usually shows bands due to *d-d* transitions around 625 nm.[72]

Proposed Structure

The proposed structure is a polymeric entity, pictured in Fig. 51.

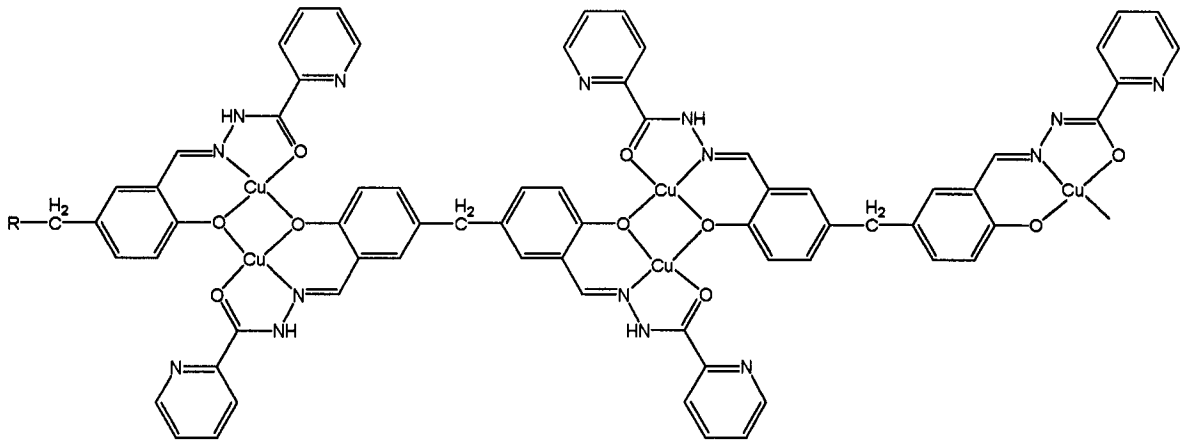

Fig. 51. Proposed structure of **2**.

In this proposed structure a single pseudo octahedral planar copper cation is bound by a tridentate pocket of each ligand, with the remaining bidentate pocket of the ligand being unoccupied. Bridging between pairs of copper cations would reasonably occur through the two phenolic oxygens, one from each ligand. As for the previous compound, **1**, there should be no ligand-mediated magnetic communication between copper cations bound to opposite sides of the same ligand, since they lack a suitable exchange pathway through the ligand.

The formula for **2** requires that each ligand be mono-anionic. Although diazine ligands are most often found in the enol form with deprotonation at the oxygen, the requirement for monoanionic ligands suggests that this site is not deprotonated. In this case the interaction between the Cu(II) cation and oxygen would appear to be through the keto form of the ligand.

Axial coordination sites at the copper cations could be provided either through coordination by solvent, or through the pairing of the polymeric strands allowing

bridging of the copper cations through either the carbonyl or phenolic oxygens. Occupation of these sites by solvent molecules seems the more likely structure however.

The magnetic profile of this complex is consistent for this proposed structure. The room temperature moment of 2.40 μ_B per dinuclear subunit is consistent with the spin only value for two copper(II) cations of 2.45 μ_B. The magnetic profile with respect to temperature shown in Fig. 52 clearly shows an antiferromagnetic interaction which would be expected for a compound with the proposed phenolic bridges between metals. From the situation presented above one would expect the magnetic profile to be quite simple, and fit to the Bleaney-Bowers equation for simple binuclear Cu(II) systems. Attempts to fit the data to this equation were unsuccessful suggesting that the structure and interpretation of the magnetic situation as an isolated binuclear system may not adequately describe the actual situation and that additional interactions may be present. At this point no completely successful magnetic model has been found for this compound.

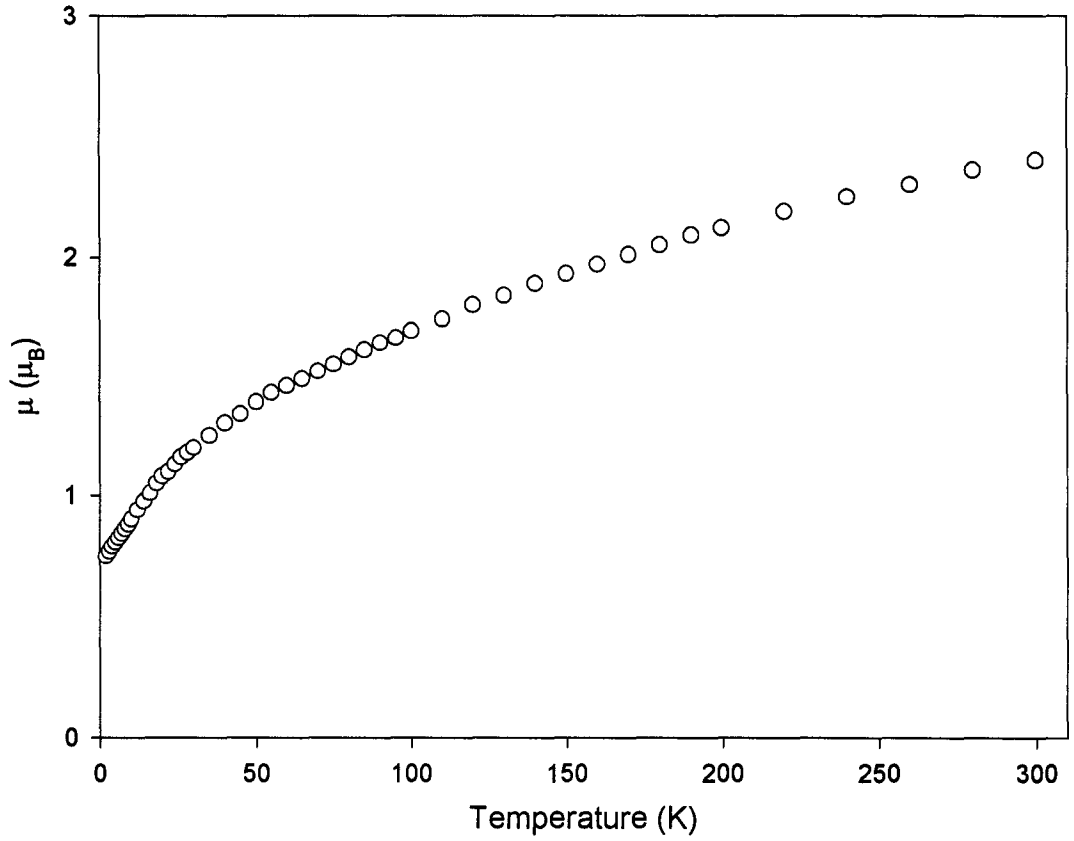

Fig. 52. Magnetic profile of **2** (H = 1000 Oe).

$[(Cl2POAP)_6Fe(II)_8Fe(III)](ClO4)_8 \cdot 23H_2O$ (**3**)

Spectroscopy

From the MALDI-TOF MS spectrum of **3** it is possible to estimate the oxidation states of the metals. The molecular ion peak at M/z = 3,111 corresponds to a singly-charged positive ion. The isotope splitting pattern can be successfully modeled (IsoPro[78]) and corresponds to the singly-charged species $[(Cl2POAP\text{-}3H)_6Fe(II)_8Fe(III)]^+$ indicating that one Fe centre is Fe(III). The modeled peak should appear at 3111.6 M/z, the very slight discrepancy being a result of instrumental calibration.

Crystallography

The X-ray crystal structure of the cation of **3** is shown in Fig. 53, and of the metal-oxygen core in Fig. 54. Crystallographic data are presented in Appendix B. Due to the poor refinement, comments on the structure will be restricted to the molecular cation which is clearly revealed.

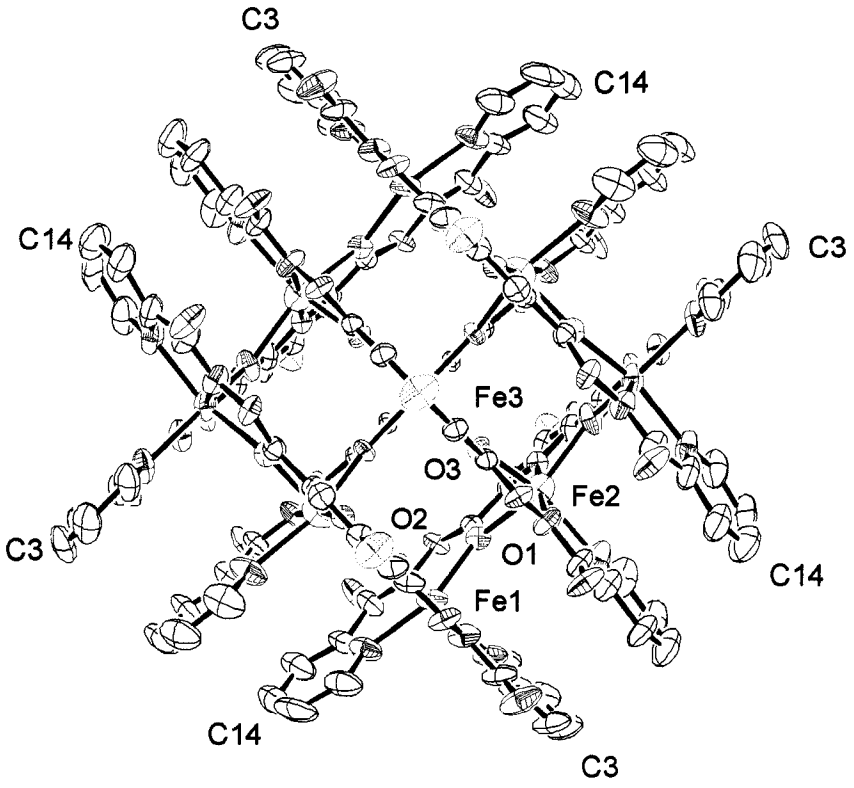

Fig. 53. Crystal structure of **3**.

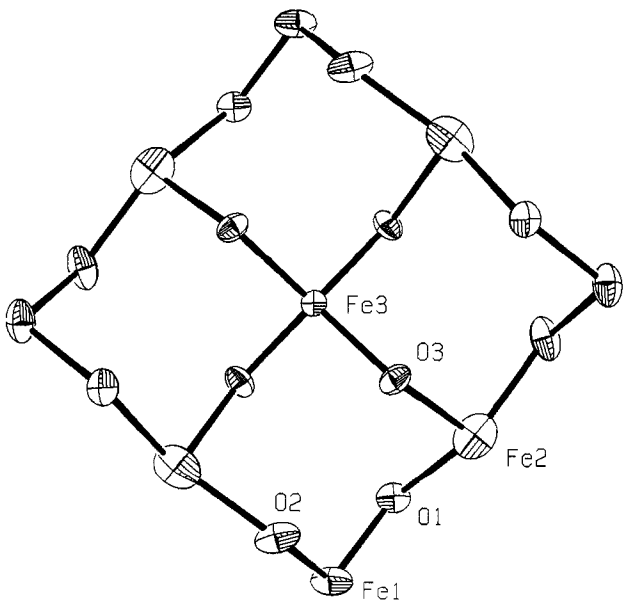

Fig. 54. [Fe_9 (μ-O)$_{12}$] core structure of **3**.

The structure of the cation is a [3×3] grid of nine, alkoxo-bridged pseudo-octahedral, Fe centers coordinated by two groups of three roughly parallel ligands arranged above and below the pseudo-plane described by the metals. There are 8 perchlorate anions identified in the structure, and so assuming a $Fe(II)_8Fe(III)$ charged arrangement, as indicated by MALDI/TOF mass spectrometry, the six ligands would contribute a total negative charge of 11^-. Therefore five of the ligands are assumed to have a charge of 2^-, and the remaining one 1^-.

Table 1 gives selected bond lengths and angles relevant to the iron coordination spheres. There are three distinct coordination environments in which iron cations reside. The corner iron atoms, Fe1, reside in a *cis*-FeN_4O_2 environment; along the sides, the Fe2 coordination environment is *mer*-FeN_3O_3, and the central iron atom, Fe3, resides in a *trans*-FeN_2O_4 environment. Due to the high symmetry of the cluster there are only three unique iron atoms corresponding to the three different coordination environments.

Table 1. Selected bond lengths (Å) and angles (°) for **3**.

Fe1	N3	2.004(7)		Fe2	N12	2.014(7)
Fe1	N8	2.016(8)		Fe2	N5	2.094(6)
Fe1	O2	2.017(5)		Fe2	O3	2.150(5)
Fe1	O1	2.030(5)		Fe2	O1	2.214(5)
Fe1	N1	2.166(8)		Fe2	O2	2.240(6)
Fe1	N6	2.174(7)		Fe2	N10	2.291(8)
				Fe3	N14	2.069(8)
				Fe3	O3	2.091(5)
Fe1	O1	Fe2	132.5(3)			
Fe1	O2	Fe2	132.0(3)	Fe1	Fe2	3.885(5)
Fe3	O3	Fe2	135.5(3)	Fe3	Fe2	3.926(4)

The metal ion geometries are controlled somewhat by the way in which the six ligands assemble as the grid is formed. The contiguous, linear arrangement of five-membered chelate rings associated with the three coordination pockets of each ligand causes some strain within the grid such that the terminal pyridine group Fe-N bond lengths are lengthened corresponding to N1, N6 and N10 in Table 1. Fe3, the central iron in the grid, occupies a smaller "pocket" within the ligands, with generally shorter bond lengths, compared to Fe2 and Fe1. The central disubstituted pyridine to iron (Fe3-N) distance is 2.069(5) Å, compared with the value of 2.094(6) Å for the comparable length involving Fe2.. The central Fe3-O3 bond length of 2.091(5) Å, is also short when compared with an average Fe-O bond length of 2.130(5) Å for the other Fe's present. These shorter bonds are consistent with the proposal of the central Fe cation being Fe(III) rather than Fe(II).

The iron-iron distances are consistent with other grids of this ligand type. For instance, in the complex $[Mn_9(Cl2POAP\text{-}2H)_6](ClO_4)_6 10H_2O$[70] the Mn-Mn distances in the outer ring of eight metal centres range from 3.88 Å to 4.06 Å while distances from the central Mn(II) to its immediate neighbors fall in the range of 3.94 – 4.03 Å. By comparison **3** has lengths consistent with the lower end of the range for $[Mn_9(Cl2POAP\text{-}2H)_6](ClO_4)_6 10H_2O$. The Mn-O-Mn bond angles however are all smaller than the Fe-O-Fe angles in **3**, ranging from 126.4° to 130.7°.

The aromatic rings of the ligands are roughly parallel to those on the neighboring ligand with separations between rings on the order of 3.9 Å. This suggests that there may be some level of interaction between the π-electron clouds, which may be a significant

interaction which aids in the formation of the grid by causing adjacent ligands to align parallel to one another.

The arrangement of the metals themselves is not perfectly planar, but is puckered, as can be seen in Fig. 55.

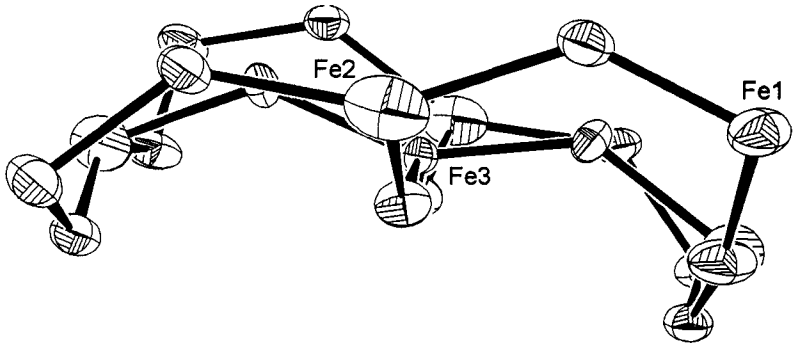

Fig. 55. Iron-alkoxo moiety of a single molecule seen along the xy-plane of **3**, illustrating ring "puckering".

In the crystal lattice the clusters themselves are arranged in layers in the xy-plane and stacked in the z-plane as can be seen in Fig. 56. The layers are offset from one another such that in every second layer the grids are aligned directly above one another.

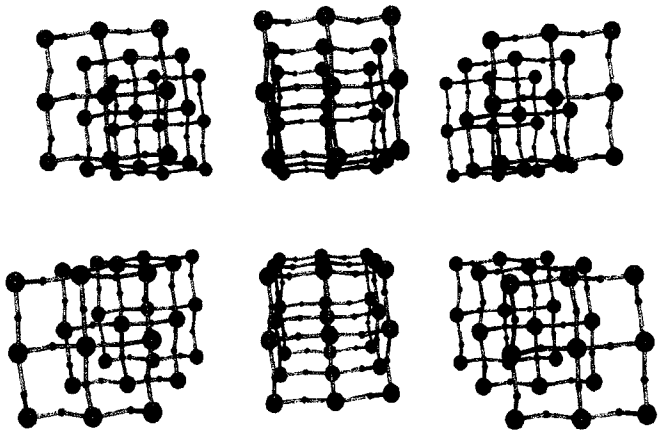

Fig. 56. Layers of grid molecules (core shown only) stacked in the 'z' direction..

The overall packing of grids within the crystal lattice shows a number of sites through which long range intermolecular magnetic interactions may occur. The nearest point of contact between adjacent rings in the xy layers is 3.64(5)Å between atoms C3 and C14 of adjacent grids. The hydrogen atoms bonded to these carbons are separated by 2.50(4) Å (Fig. 57).

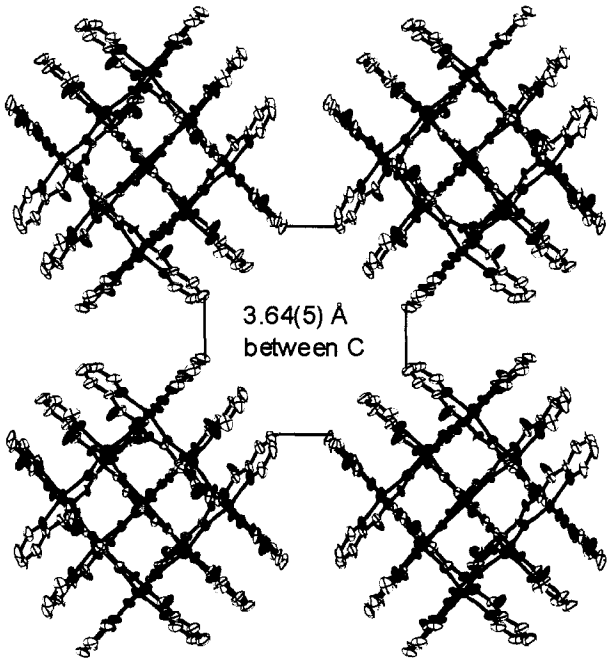

Fig. 57. Points of close contact between adjacent grids of a single layer of **3**.

In Fig. 58 we see the closest contact points between adjacent grids in adjacent layers. The distance marked "A" (9.37(4) Å) is the distance between Cl atoms on the central pyridine rings of the ligands of two grids directly above one another (and therefore measured through the "hole" of a layer between them since the layers are offset). The closest contact between grids in adjacent layers is the 3.65(6) Å separation marked "B", the distance between the Cl atom of one grid and a carbon atom on a terminal pyridine ring of a second grid molecule. A final point of close contact is that marked "C" on Fig. 58, between amines of adjacent clusters at a distance of 5.31(7) Å.

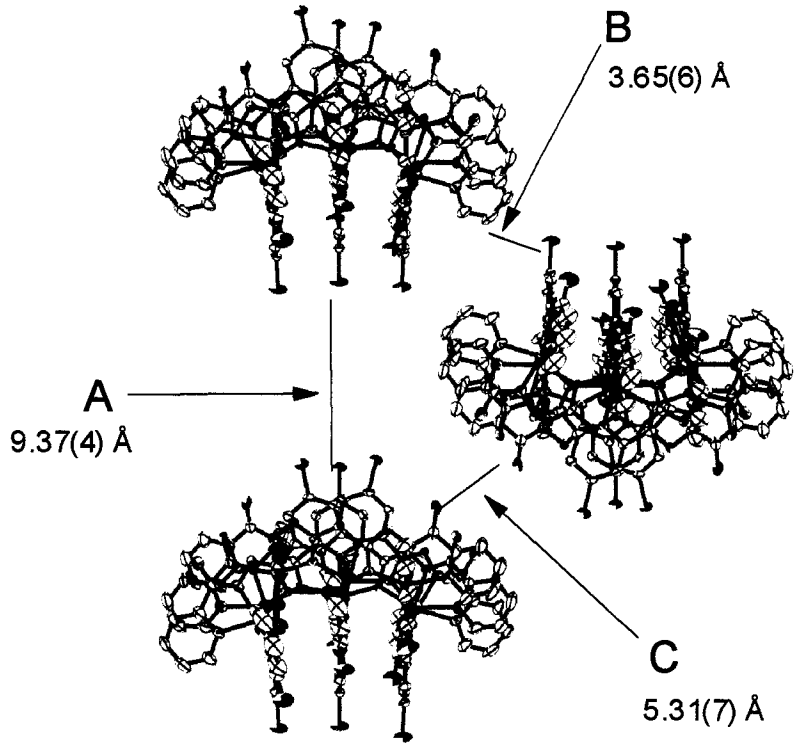

Fig. 58. Points of close contact between adjacent grids of **3**.

None of these points of close contact are likely to be involved in intermolecular magnetic interactions as the metal cations themselves are quite well insulated by the surrounding ligands and the metal cores of the clusters are quite distant from one another with Fe-Fe distances >10 Å.

Mössbauer Spectroscopy

Mössbauer spectra of **3** show the presence of three distinct types of iron cations at low temperature with the intensity ratio 1:4:4 (see Fig. 60 and Fig. 60), consistent with the ratio of the Fe cations in the grid (one central, four apical and four corner). The quadrupole splittings) corresponding to Fig. 60 (at 293 K) are 3.38 mm/s (1,6), 2.00

mm/s (2,5), and 0.30 mm/s (3,4) with isomer shifts (δ) of 1.0, 1.1, and 1.3 mm/s respectively, relative to iron metal. Typical isomer shifts for high spin Fe(II) appear around 1.3 mm/s, and for high spin Fe(III) are in the range of 0.5 – 0.7 mm/s. The splitting values are indicative of the Fe cations occupying a range of distorted octahedral environments.[79] Ideally the smallest value of ΔE_Q should correspond to the central iron of the grid as it is in the least distorted environment according to the crystal structure. Likewise, the next most distorted environment should be the four side Fe ions and finally, the most distorted is that of the corner cations of the grid. The Mössbauer spectra are consistent with this interpretation with the highly distorted signals (those with the larger quadrupole splitting values) being more intense while the least split signal is the least intense.

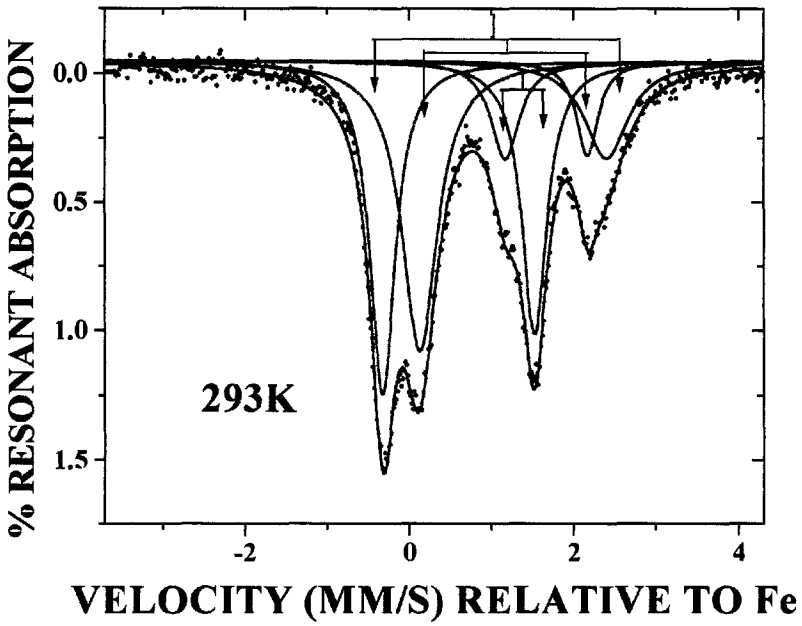

Fig. 59. Mössbauer spectra of **3** at 293 K.

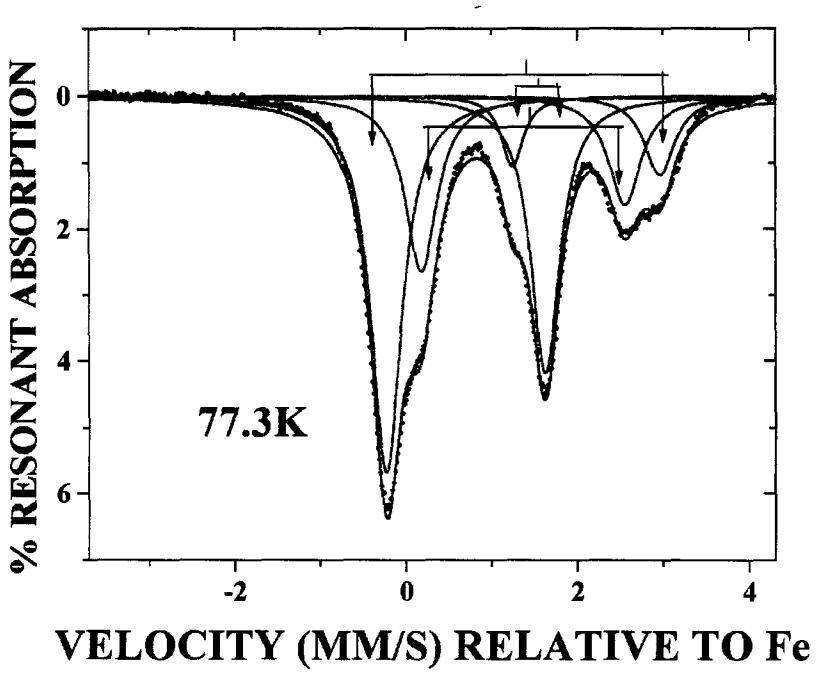

Fig. 60. Mössbauer spectra of **3** at 77.3 K.

Despite the fact that the Mössbauer spectrum at 293 K shows no signals in the 0.5 – 0.7 mm/s range, in which high spin Fe(III) signals are normally found, this is not necessarily evidence to indicate the absence of Fe(III). Chemical shift increases with an increase in the electron-withdrawing nature of the ligands, and these quoted ranges have been defined through observations on classical compounds.[79] In light of the complexity of the cluster, it is not unlikely that the HS Fe(III) signal may appear in a region more commonly associated with HS Fe(II).

As the temperature at which the spectra are taken is lowered the appearance changes, indicating a phase transition. The temperature at which this transition occurs corresponds to the beginning of the second antiferromagnetic interaction in the μ vs. T plot at 10K and would appear to be connected in some way (Fig. 61).

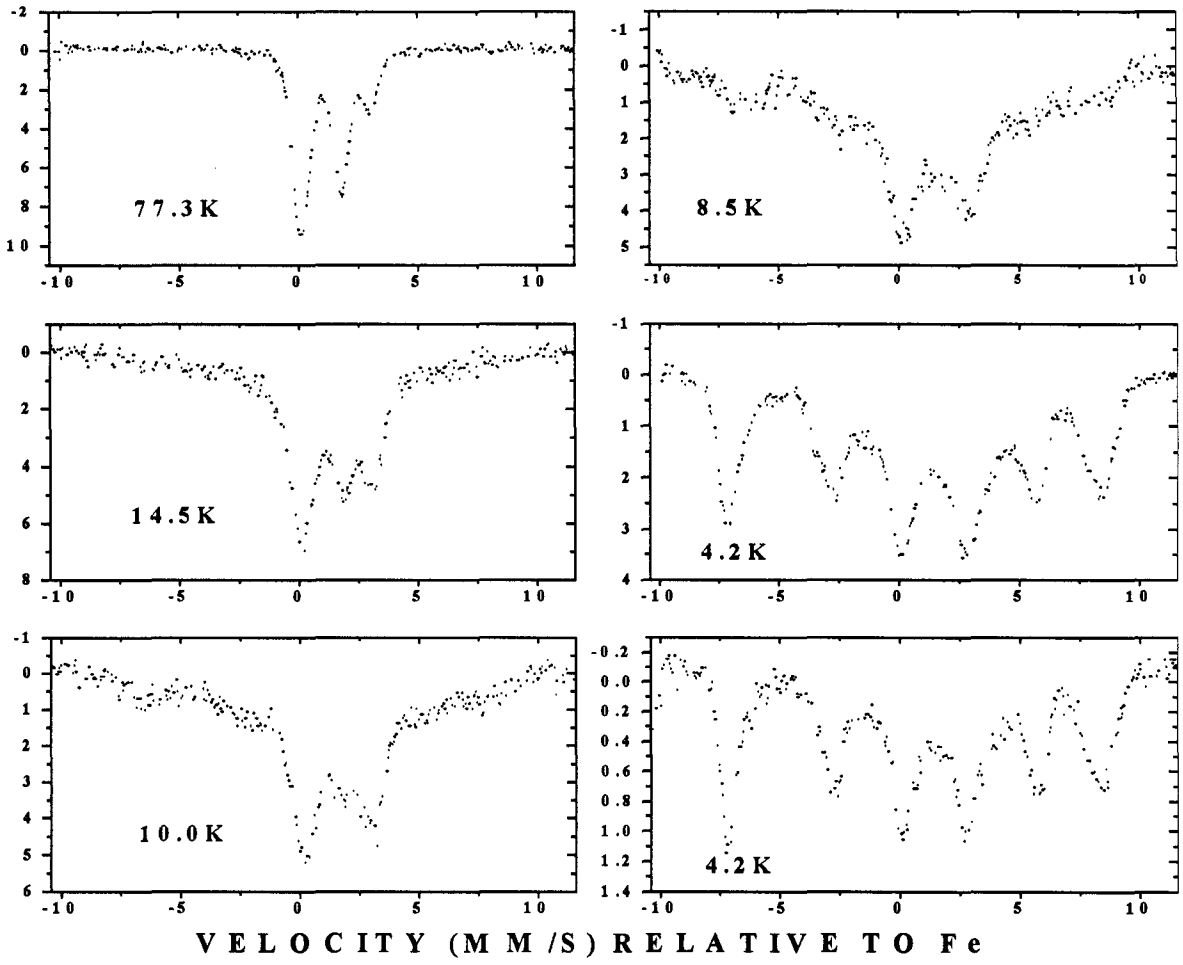

Fig. 61. Mössbauer spectra for **3** at 77.3, 14.5, 10.0, 8.5, and 4.2K.

ESR Spectrometry

Although the Mössbauer spectra do not conclusively confirm the presence of high spin Fe(III), due to the lack of a signal in the range in which HS Fe(III) cations typically appear, the presence of Fe(III) in **3** is confirmed through an ESR (electron spin resonance) spectrum taken at 120 K (Fig. 62).

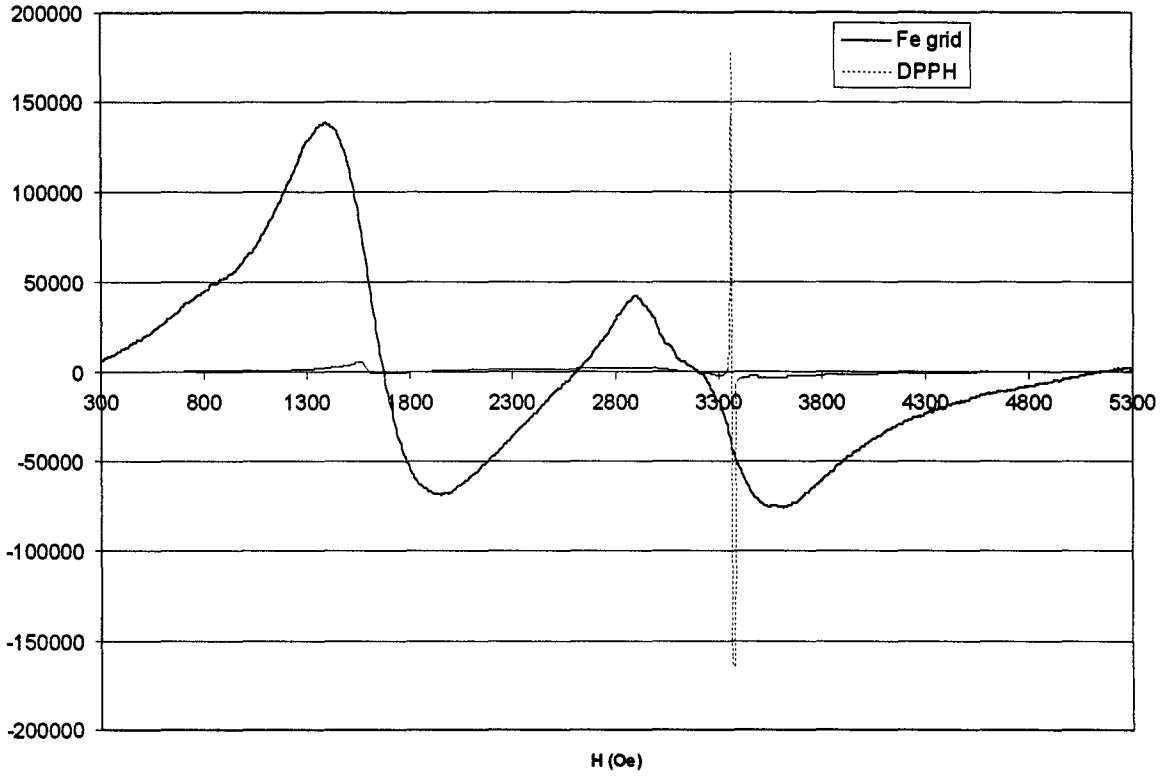

Fig. 62. X-Band ESR spectrum of **3** taken at 300 K.

The ESR spectrum is consistent with HS Fe(III), showing two signals with g_z = 2.08 and g_{xy} = 4.2. The first signal appears at H = 3300 Oe and the second, larger signal appears at H = 1670 Oe. Fe(II) cations are ESR silent and so do not appear in the spectrum.

Considering this evidence in terms of Hard Soft Acid Base Theory (HSABT) we see that the placement of the two types of iron cations is reasonable. Fe(III), a harder acid than Fe(II), will prefer to bind in the metal binding pocket of the arrangement of the six ligands which has the hardest environment. The central pocket in the complex with

an O_4-N_2 coordination environment is the hardest, and will therefore prefer to bind to Fe(III). The remaining softer sites being O_2-N_4 and O_3-N_3 will be preferred by the softer Fe(II) cations.

Magnetism

The variable temperature magnetic data for **3** are shown in Fig. 63 as a plot of μ_{mol} as a function of temperature. The room temperature moment of 14.5 μ_B is consistent with the presence of eight high spin Fe(II) cations and one high spin Fe(III) cation (μ_{SO} = 15.07 μ_B). The drop in magnetic moment as temperature is lowered is indicative of intramolecular antiferromagnetic exchange within the grid. This continues to a temperature of about 45 K, at which point the moment rises from 11.5 to 13.0 μ_B at 8.5 K, suggesting the presence of a ferromagnetic interaction as well. The drop in moment below 8.5K may signal additional antiferromagnetic exchange or possibly the effect of zero field splitting.

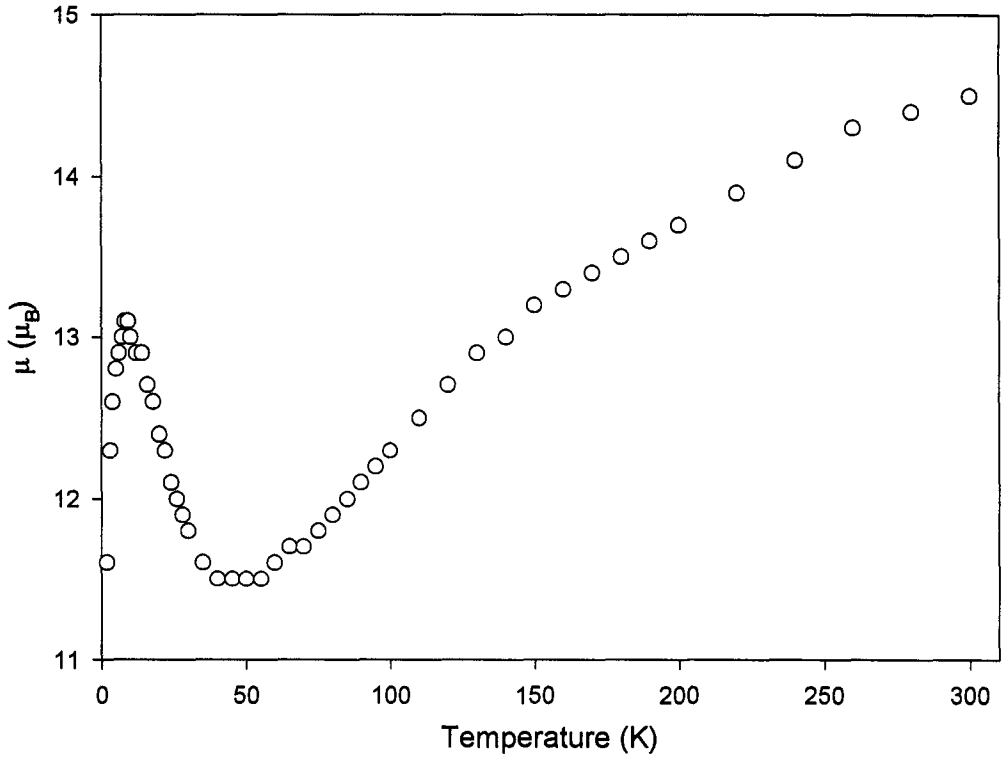

Fig. 63. Variable temperature magnetic profile of **3** (H = 0.1T).

This profile with its apparent ferromagnetic exchange at low temperatures is quite unusual since in comparable Mn(II) grid complexes with this and related ligands, only antiferromagnetic interactions are observed. This magnetic behavior is very similar to the Fe(III) complex of 2POAP, $[Fe_9(2POAP\text{-}2H)_6](NO_3)_{15}\cdot 18H_2O$ (**6**)[70] which also shows a similar mixture of ferromagnetic and antiferromagnetic effects at varying temperatures. In **6** this ferromagnetism has also been attributed to non-participation of the t_{2g} orbitals in direct magnetic exchange, and the observed magnetization at the temperature of the maximum in moment is consistent with the presence of residual t_{2g} electrons.[70]

The magnetic properties of **3** may be explained in a similar manner to **6** by considering the electronic structure of the Fe(II) and Fe(III) cations according to Crystal

Field Theory (See Fig. 64). In an octahedral cation in which six ligands are placed along the Cartesian axes, the d-orbitals go from being electronically degenerate, as in the case of the free cation, to being split into two roughly degenerate sets of orbitals. Of these two sets the e_g, consisting of the d_z^2 and $d_{x^2-y^2}$ orbitals, lie along the Cartesian axis while the t_{2g}, consisting of the d_{yz} d_{zx} and d_{xy} orbitals lie between them. Thus the e_g orbitals are aligned with the oxygen groups which mediate the magnetic interactions in the cluster while the t_{2g} orbitals do not. If the orbitals are highly anisotropic, as is the case for Fe, exchange of electrons between the e_g and t_{2g} orbitals might not be possible, resulting in only the electrons of the e_g orbitals undergoing magnetic interactions, in this case antiferromagnetic coupling. The drop in moment from 300 K to 50 K is therefore a result of this antiferromagnetic coupling.

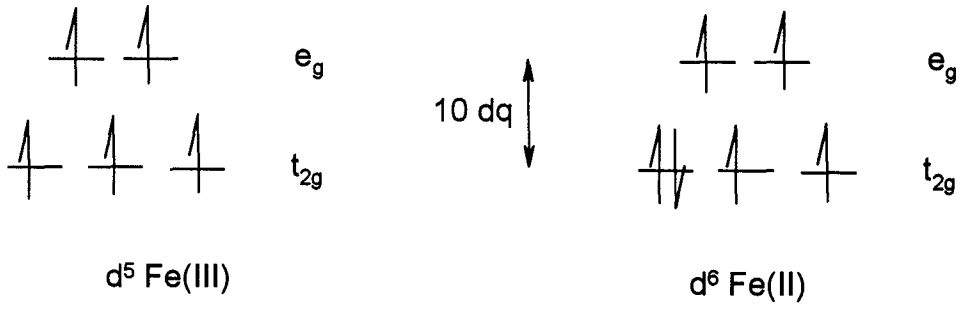

Fig. 64. Electronic configuration of Fe(II) and Fe(III).

The ferromagnetic interaction at lower temperatures may be a result of the residual unpaired electrons in the t_{2g} interacting with one another in a through space intramolecular ferromagnetic interaction. Eventually the ferromagnetic interaction is diminished at the lowest temperatures through additional antiferromagnetic interactions, or possibly zero-field splitting.

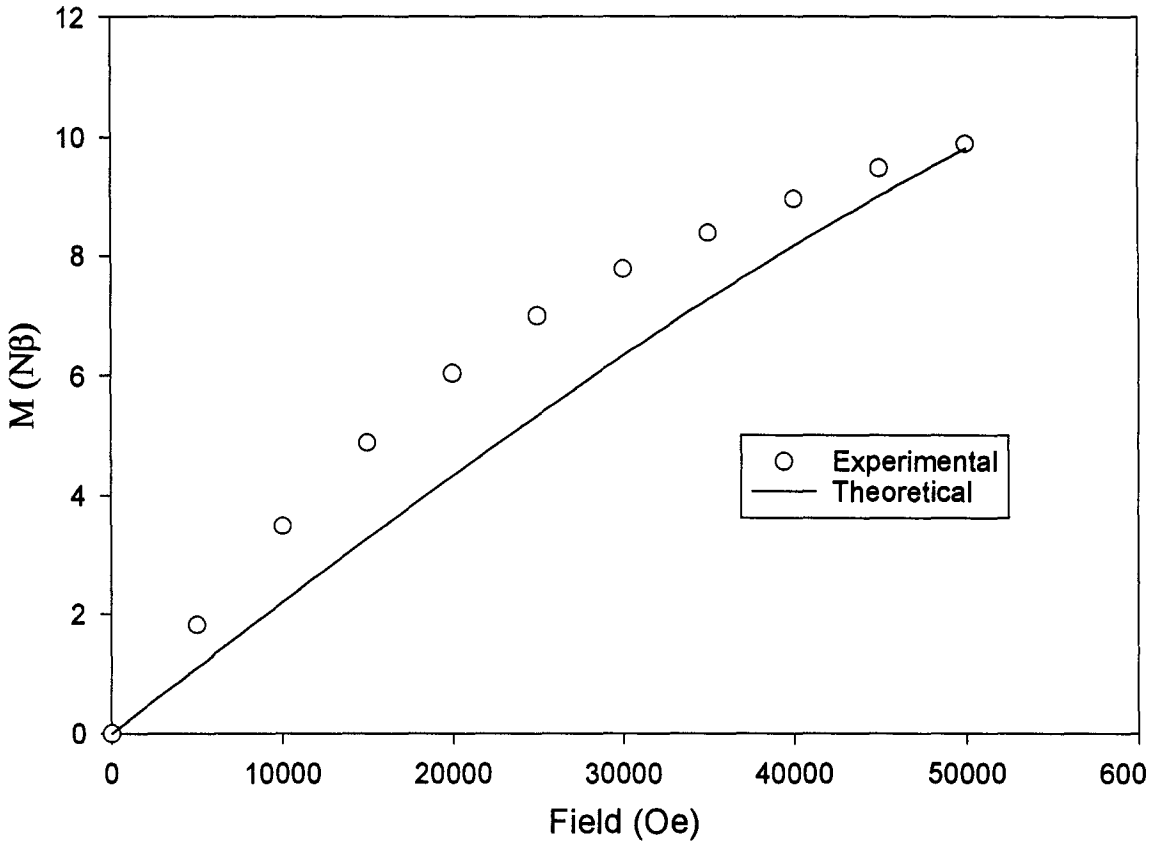

Fig. 65. Magnetization vs. Field for **3** at 10 K.

The magnetization vs. field data for **3** at 10 K are also consistent with this interpretation of anisotropic orbital interactions. The solid line in Fig. 65 represents the magnetization of a collection of eight S = 2/2 spin centers and one S = 5/2 center (assuming g = 2), and is consistent with the experimental data. This situation corresponds to one in which the electrons within the e_g orbitals have paired antiferromagnetically resulting in the external Fe(II) cations having a residual S = 2/2 spin state and the internal Fe(III) cation having a full S = 5/2 spin state. This interpretation assumes that the coupling between the central and peripheral metal cations

is very small, which is a which is a characteristic feature of the grids formed by the 2POAP family of ligands with Mn(II).[70]

The deviation of the experimental data from the theoretical may be the result of a situation in which $g \neq 2$, in addition to weak ferromagnetic coupling between the residual spins of the e_g orbitals.

In the case of **6** the magnetization at 2 K appears to be consistent with an assembly of nine independent S = 3/2 centers. At 2 K the magnetization of **3** does not show this behavior, the experimental data are smaller than the theoretical function for eight S = 2/2 (Fe(II)) and one S = 5/2 (Fe(III)) centers (Fig. 66) indicating that the magnetic interactions for **3** are not the same as those in **6**, despite the similarity of their μ vs. T plots.

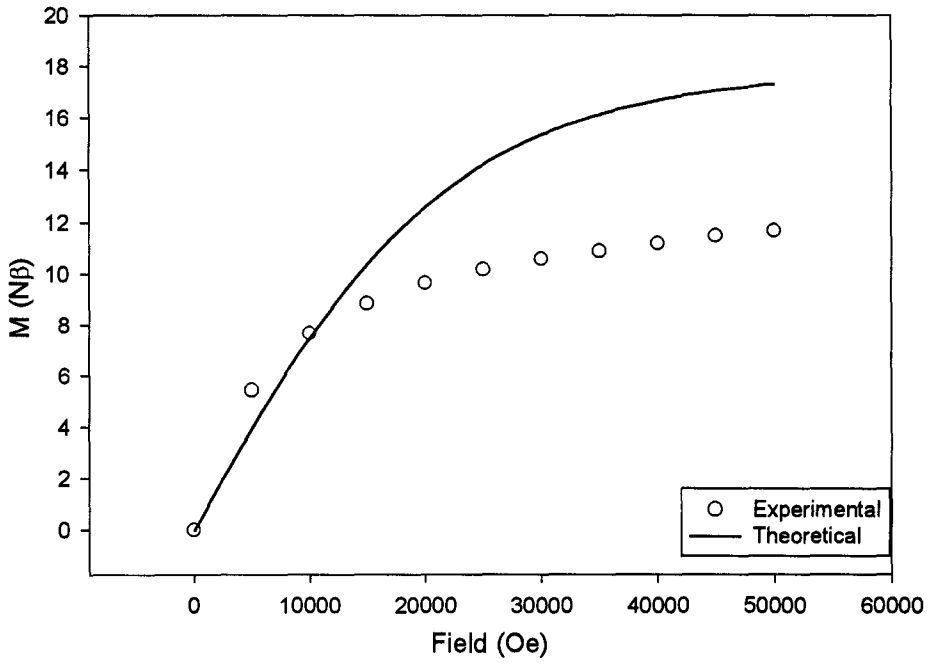

Fig. 66. Magnetization vs. Field for **3** at 2 K.

$[(P2OAP)_4Ni_4]\cdot 12H_2O$ (4)

Spectroscopy

FT-IR evidence in the case of complex **4** is informative, since the CO and CN stretches have shifted to lower values, compared with the free ligand, indicating the complexation of these groups to the metal cations. The absence of a BF_4^- band in the spectrum indicates that the ligand, and possibly solvent, is the sole source of anionic charge to balance the metal cation charge. Finally the pyridine breathing mode vibration at 1002 cm^{-1} in the ligand has split into two peaks in the complex spectra at 1022 and 1002 cm^{-1}, indicating that both complexed and uncomplexed pyridine rings are present in the structure.

The red colour of the complex suggests that square planar Ni(II) is present. The UV-VIS spectrum of **4** shows a number of very broad bands, the most intense being a sharp band at 330 nm, accompanied by broader bands at 490 nm, 714 nm, and the broadest band at 1109 nm. The 330 nm band is most likely a charge-transfer transition. Characteristic bands of square planar spectra are usually found in the range 400 – 670 nm, and their spectra are notable in the lack of any bands above 1000 nm. The bands at 490 and 714 nm are consistent with square planar Ni(II). The existence of a band at 1109 nm suggests that this is not an exclusively square planar complex as a band in the range of 770 to 1400 nm is typically seen in octahedral Ni(II) spectra. The broadness of the bands at 490 nm and 714 nm could be explained by overlapping of peaks associated with other octahedral Ni(II) (usually two additional peaks at 370-525 nm and 500-900 nm are

found in octahedral Ni(II) spectra) with nearby bands from the square planar Ni(II) centres.

Proposed Structure

Although the empirical formula of one metal per ligand is inconsistent with that of a [3×3] L_6M_9 grid, it is consistent with a [2×2] grid. The formation of "pin-wheel" like Cu(II) clusters[i] (see Fig. 1) from symmetrical tritopic ligands (e.g. 2POAP) with three pockets suitable to bind metals has been observed. In these cases, the central pocket and one external pocket of the ligands are occupied by a pair of metals which form a central [2 × 2] square grid arrangement. The remaining pocket of each ligand binds a single metal which fills its additional coordination sites through interactions with solvent molecules or anions. The complex $(Cl2POMP)_4Cu_8(NO_3)_8 \cdot 12H_2O$[ii] for instance is a typical example of a molecular "pin-wheel".

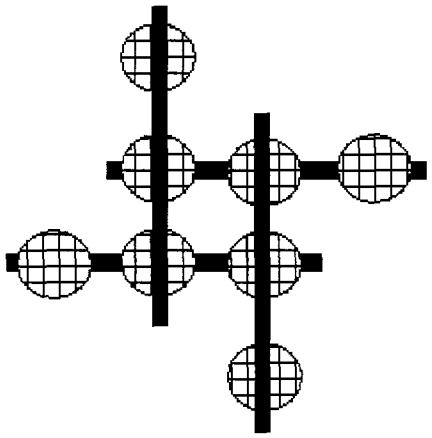

Fig. 1. Schematic of a fully occupied molecular "pin-wheel", metal-ligand moiety only.

If the secondary metals on the periphery are excluded, the four core metals with four ligands would be a good potential model structure for the complex **4**. Despite the fact that the metal cation was added in excess, occupation of the peripheral pockets appears not to have occurred. This may be due to acidity effects, a phenomenon seen in the ligand POAP. In the complex $[(POAP)Fe(III)(NO_3)_2(H_2O)_2]$[82] in which $Fe(NO_3)_3$ is reacted with POAP, protonation of a pyridine ring occurs and hydrogen bonding interactions with solvent water molecules have the effect of blocking the bidentate pocket of the ligand, preventing the building of a polynuclear cluster and resulting in the formation of a mononuclear complex (see Fig. 68).

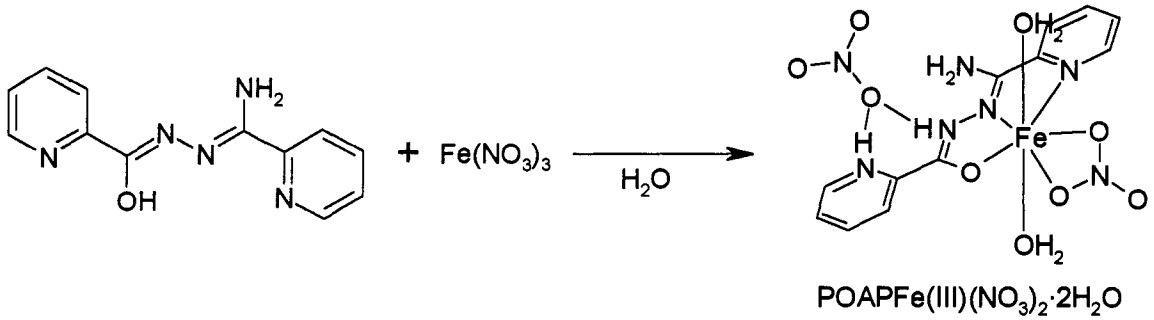

Fig. 68. Synthesis of and structure of $[(POAP)Fe(III)(NO_3)_2(H_2O)_2]$.

The proposed structure for **4** based on the evidence presented, is of an incompletely occupied molecular "pin-wheel" in which four Ni(II) cations each occupy tridentate pockets on two separate ligands, leaving the bidentate pocket empty. In bonding in this manner, the ligands completely satisfy the coordination requirements of the Ni(II) cations without the need for additional donors.

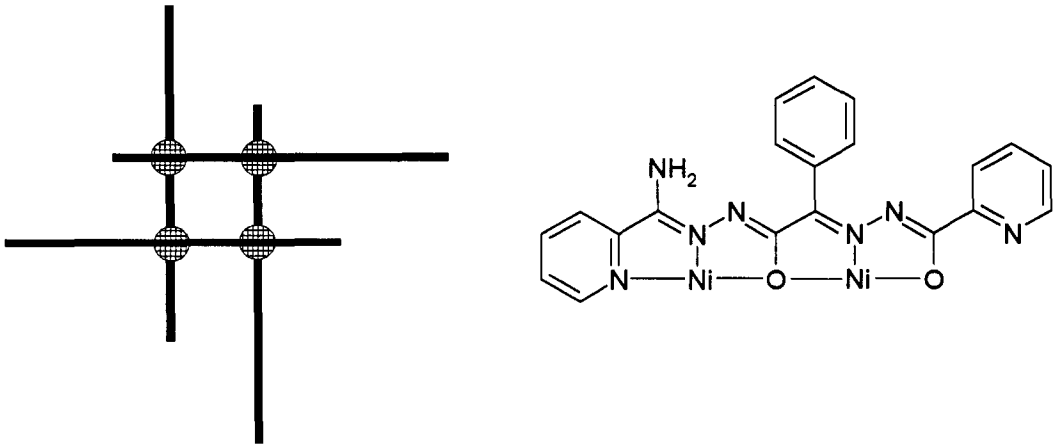

Fig. 69. Proposed structure of **4** showing Ni(II) binding mode of P2OAP.

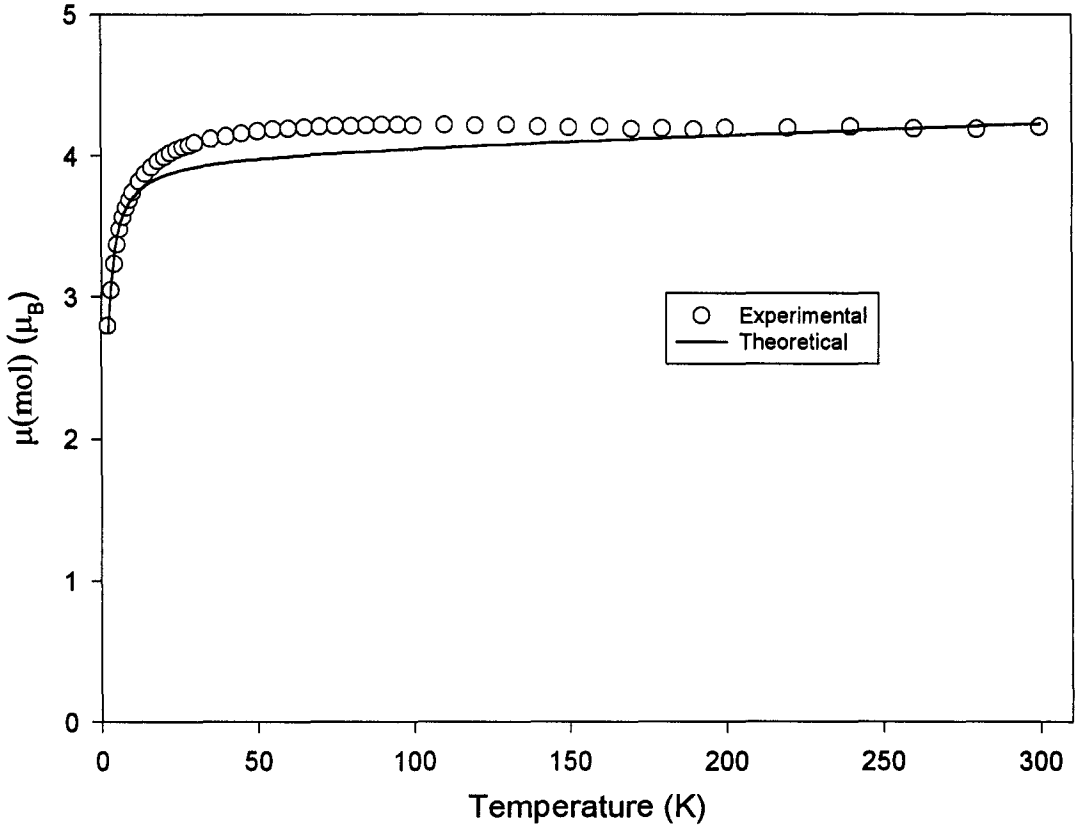

Fig. 70. Variable temperature magnetic data for **4**. The solid line represents the best fit data to the parameters given in the text.

The magnetic profile for **4** shows a room temperature moment of 4.10 μ_B per mole, which is much lower than the spin-only moment of 5.66 μ_B for four octahedral nickel(II) cations. Below 85 K a drop in the moment occurs as the temperature falls resulting in a final value of 2.79 μ_B at 2 K, suggesting an intramolecular antiferromagnetic interaction.

In light of the magnitude of the magnetic moment, it is obvious that not all of the Ni(II) cations are magnetically active but must instead be diamagnetic. If some Ni(II) cations are in either a square planar or a strongly distorted tetragonal environment, approaching a square planar form, the electronic structure of the complex would be altered. In an octahedrally coordinated high spin Ni(II) cation the eight d-electrons are arranged such that there are two unpaired electrons, which are the source of its magnetic properties. In a square planar d^8 (low spin) system there are no residual unpaired electrons and the cation is diamagnetic (see Fig. 71).

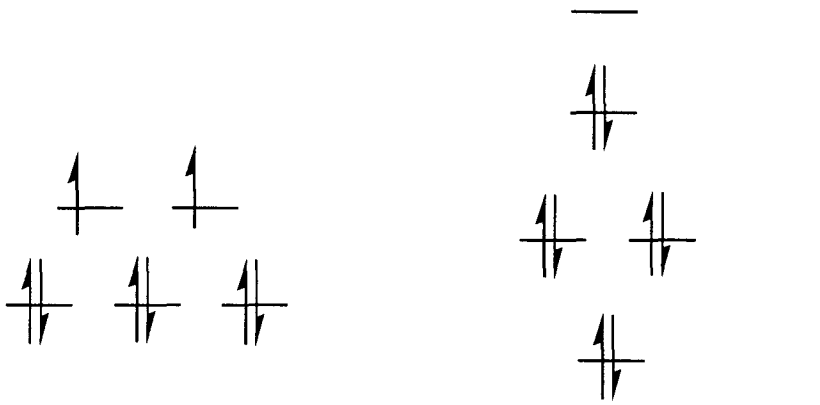

Fig. 71. Electron configurations of octahedral and square planar d^8 cations.

With this in mind, if two of the four nickel cations were in highly distorted elongated tetragonal environments and diamagnetic, the magnetic properties would resemble those of a simple binuclear system. In this case the spin only magnetic moment for two octahedral nickel(II) cations is 4.00 μ_B, a value much more in line with the observed room temperature moment of the complex of 4.10 μ_B. In this light a reasonable magnetic model would be that of a binuclear system (see Fig. 72), with two distant S = 2/2 Ni(II) centres interacting over four bonds in which case a very weak interaction is expected.

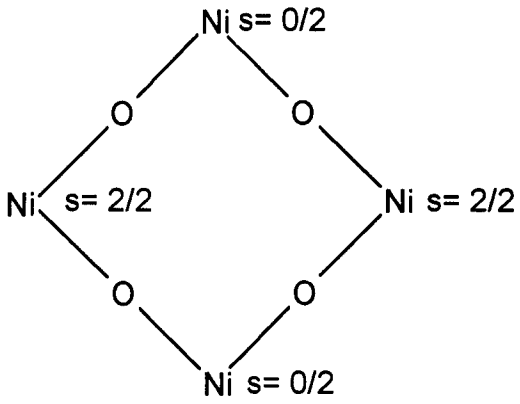

Fig. 72. Exchange diagram for **4**.

For binuclear systems the exchange Hamiltonian is given by :

$$H_{ex} = -2J_{12}\{S_1 \cdot S_2\} \tag{8}$$

and the energy per spin state is given by:

$$E(S') = -J_{12}[S'(S'+1) - 2S(S+1)] \tag{9}$$

Fitting using equation (9) and the Van Vleck equation for a binuclear case:

$$\chi_M = \frac{Ng^2\beta^2}{3kT} \frac{\sum S'(S'+1)(2S'+1)e^{(-E(S')/kT)}}{\sum (2S'+1)e^{(-E(S')/kT)}} \tag{10}$$

we obtain values of:

$g = 2.00$
$J = -0.6\ cm^{-1}$
$TIP = 809 \times 10^{-6}\ emu.mol^{-1}$
$\rho = 0.006$
$\theta = -1$
$R = 0.0387$

The theoretical line generated with these parameters is shown in Fig. 70.

The value of g is somewhat lower than that expected for Ni(II), which typically shows g values slightly higher than 2. Temperature-independent paramagnetism (TIP) is consistent for four Ni(II) cations which typically have a TIP of approximately 200×10^{-6} $emu.mol^{-1}$ each. J is quite small, indicating that the exchange interaction is antiferromagnetic and very weak, as is expected for an exchange occurring over four bonds and through three bridging atoms.

The value of J is so small that there is the possibility that the low temperature drop observed may be a result of zero field splitting (ZFS) of the Ni(II) and not due to an antiferromagnetic exchange interaction at all. Fitting using the MAGMUN program (see Appendix A) to a formula involving a ZFS term instead of an exchange integral between octahedral Ni(II) cations results in a much poorer fit to the experimental data and therefore the zero field splitting is a less likely explanation than very weak exchange.

Chapter 5. Conclusions

A variety of ligands have been synthesized using a general method producing Schiff-base like linkages between ester, ketone, and other suitable groups of appropriately designed precursors. Using this general approach it has been demonstrated that ligands can be synthesized which possess linear pockets of metal binding groups, with potential oxygen bridges, which are correctly arranged to complex metals such that they may interact magnetically.

Incorporating a "molecular spacer" molecule with the proper geometry, or by "doubling" a ligand through the use of a 2,6-disubstituted pyridine group, for example, in the place of a mono-substituted pyridine group allows the extension of the ligand, with the introduction of a tridentate metal binding pocket in the place of a bidentate pocket. These strategies can result in the creation of *n*-topic ligands capable of forming [$n \times n$] molecular grids.

Ligands such as di-OAOP and 2PAOP have variations in their structure which can result in a non-linear series of metal binding pockets, or in forming a ligand which has two di-topic sections linked through a flexible spacer such as a $-CH_2-$ group.

Using the ligand di-OAOP, two compounds were synthesized and assigned structures based on their physical and magnetic properties. The nickel complex, [(di-OAOPNi·2.5H_2O)$_n$] (1), is of particular interest since it behaves as a molecular-based magnet, showing a particularly strong hysteresis of the magnetization and a spontaneous magnetization below 15 K, the result of a cooperative effect between adjacent ferromagnetic chains.

The magnetic properties of the copper (II) complex, $[(di\text{-}OAOP)Cu_2(BF_4)_2(H_2O)_5]$ (**2**) are much less interesting, with no long distance ferromagnetic ordering of magnetic properties. However this compound does not behave as a "typical" isolated binuclear system raising the possibility that some extended intermolecular interaction may be occurring.

The grid complex $[(Cl2POAP)_6Fe(II)_8Fe(III)](ClO4)_8 \cdot 23H_2O$ (**3**) shows a less common low temperature ferromagnetic effect in addition to the typical antiferromagnetic coupling usually observed in the grids of the 2POAP family of ligands. Interestingly this compound also has metals in two different oxidation states with eight Fe(II) centres and a single Fe(III) centre. The magnetic properties have been rationalized based on comparison with the $Fe(III)_9$ complex of 2POAP which shows a similar behavior.

Finally the Ni(II) complex $[(P2OAP)_4Ni_4 \cdot 12H_2O]$ (**4**) is interesting since the Ni(II) cations present are apparently in two different spin states perhaps as a result of the distortion from an octahedral coordination geometry of some of the Ni(II) cations present. This has had important magnetic ramifications resulting in the system behaving as a weakly coupled binuclear Ni(II) system in which two of the Ni(II) cations are diamagnetic and appear to be functioning as a bridge between the magnetically active cations.

Appendix A. Modeling Magnetic Exchange

There are three mathematical methods for calculating the effect of a Heisenberg Hamiltonian and therefore the magnetic susceptibilities in clusters. These are vector coupling (VC), irreducible tensor operators (ITO) and full matrix diagonalization (FMD). FMD has the major disadvantage that it can result in very large matrices which require long diagonalization, and therefore computing times. The ITO method reduces the size of the matrices involved and therefore the computing times dramatically. The downside is that using the ITO method is more difficult to set up and requires a considerable degree of sophisticated mathematics.

Of these methods the easiest to set up and use is the Vector Coupling approach originally developed by Kambe[83] and extended by others, for instance Martin.[84] The complexity of these coupling schemes increases quickly with the number of metals involved and is also highly dependent on the symmetry of the cluster in order to simplify them to a manageable level. One must be able to obtain appropriate and unique combinations of spin operators in order to use this simplification.

The Van Vleck equation is used to calculate χ_M, the molar magnetic susceptibility, over a temperature range and is given below.

$$\chi_M = \frac{Ng^2\beta^2}{3kT} \frac{\sum S'(S'+1)(2S'+1)\omega(S')e^{(-E(S')/kT)}}{\sum (2S'+1)\omega(S')e^{(-E(S')/kT)}} \qquad (12)$$

E(S') is the energy of the spin state given by S'. The function $\omega(S')$ gives the degeneracy of each state having a particular value of S'. For a binuclear cluster $\omega(S') = 1$ for all values of S', however for any cluster larger than two this will not be the case. This

$\omega(S')$ factor complicates the situation when computers are used to evaluate this equation, as incorporating the $\omega(S')$ function is not easy. An alternate approach, is to simply write a computer program that evaluates the summation of the numerator and denominator for all possible states, along with their energies, as expressed in the Van Vleck equation. The problem of defining a degeneracy term is not encountered as all possible states are generated and summed, not merely all possible energy states. Therefore degenerate energy states are generated and included in the calculation and degeneracy need not be explicitly defined.

Additional parameters are often introduced into (12) as needed in order to account for additional factors. The most common factors include θ, the Weiss-like correction term allowing for weak through space coupling of adjacent metal clusters. TIP (temperature independent paramagnetism), is a paramagnetic term associated with first row transition metals. It is a result of second order Zeeman coupling between the ground state and some excited state, which remains populated due to the small energy difference, and is independent of temperature. The final term ρ is the fractional paramagnetic impurity term, which represents the fractional amount of all uncoupled paramagnetic impurities in the sample.

When all of these factors are included in the Van Vleck equation we obtain

$$\chi_{M'} = \frac{Ng^2\beta^2}{3k(T-\theta)} \frac{\sum S'(S'+1)2S_T + 1)e^{-E(S')/kT}}{\sum S'(2S'+1)e^{-E(S')/kT}} \tag{13}$$

$$\chi_M = \chi_{M'}(1-\rho) + \frac{2Ng^2\beta^2}{3kT} + TIP \tag{14}$$

Thus the normal situation for generating the exchange equation for a particular arrangement of metals requires the calculation of the total spin state combinations, via a spin vector coupling approach, along with an equation for the energy of each state $E_{(S)}$ derived from the spin Hamiltonian. These are substituted into the modified Van Vleck equation.

The software package MAGMUN[85,86] has been developed which generates the exchange equation internally, allowing the calculation of theoretical susceptibility data for a given set of parameters and allowing non-linear regression fittings of experimental data as a function of temperature. This removes the necessity for the user to develop the exchange equations them self, allowing large clusters to be modeled without having to calculate the summation of the magnetic spin vectors separately. One needs only to define the magnetic exchange model, and allow the program OW01.exe[85] to generate a table of spin states and corresponding energy levels. These are then used by MAGMUN to calculate theoretical χ_M vs. T data. The user merely defines the spin quantum number of the metals involved and sets an arbitrary coupling strength between them strength between them. -1 cm^{-1} is chosen so that the non-linear regression of the data gives a multiple of unity as the J value. The modeling of situations with more than one J can be approached by defining one "J" as a fraction of the other, a ratio which is a constant during the fitting process.

Appendix B. Crystal Structural Data

Crystal Structure of $[(Cl2POAP)_6Fe_9](ClO_4)_8 \cdot 23H_2O$

Empirical Formula	$C_{132}H_{142}N_{60}O_{52}Cl_{14}Fe_9$
Formula Weight	4399.91
Crystal System	tetragonal
Space Group	$P4_2/n$ (#86)
A(Å)	20.2231(8)
B(Å)	22.415(2)
V(Å^3)	9167.2(7)
Z value	2
D_{calc} (g/cm^3)	1.594
λ(Å)	0.71073
Temperature (K)	193(1)
R_1 (R)	0.133
wR_2 (R_w)	0.412

Crystal Structure of POMeO

Empirical Formula	$C_{10}H_{11}N_3O_3$
Formula Weight	221.22
Crystal System	monoclinic
Space Group	$P2_1/c$ (#14)
A(Å)	7.9282(2)
B(Å)	17.321(3)
C(Å)	7.948(2)
β (°)	104.17(2)
V(Å^3)	1058.2(4)
Z value	4
D_{calc} (g/cm^3)	1.388
λ(Å)	0.71069
Temperature (K)	299(1)
R_1 (R)	0.059
wR_2 (R_w)	0.054

Bonds lengths (Å) and angles (°) for POMeO.

O(1)	C(6)	1.210(4)	C(8)	O(3)	C(10)	115.9(2)
O(2)	C(8)	1.208(3)	C(1)	N(1)	C(5)	116.3(3)
O(3)	C(8)	1.328(3)	N(3)	N(2)	C(6)	119.0(3)
O(3)	C(10)	1.453(4)	N(2)	N(3)	C(7)	119.6(3)
N(1)	C(1)	1.336(4)	N(1)	C(1)	C(2)	123.9(3)
N(1)	C(5)	1.335(4)	C(1)	C(2)	C(3)	118.7(3)
N(2)	N(3)	1.366(3)	C(2)	C(3)	C(4)	118.7(3)
N(2)	C(6)	1.368(4)	C(3)	C(4)	C(5)	118.6(3)
N(3)	C(7)	1.284(4)	N(1)	C(5)	C(4)	123.8(3)
C(1)	C(2)	1.382(5)	N(1)	C(5)	C(6)	117.3(3)
C(2)	C(3)	1.368(5)	C(4)	C(5)	C(6)	118.9(3)
C(3)	C(4)	1.381(4)	O(1)	C(6)	N(2)	124.6(3)
C(4)	C(5)	1.382(4)	O(1)	C(6)	C(5)	123.1(3)
C(5)	C(6)	1.506(4)	N(2)	C(6)	C(5)	112.4(3)
C(7)	C(8)	1.496(4)	N(3)	C(7)	C(8)	124.2(3)
C(7)	C(9)	1.496(4)	N(3)	C(7)	C(9)	117.0(3)
			C(8)	C(7)	C(9)	118.8(3)
			O(2)	C(8)	O(3)	124.0(3)
			O(2)	C(8)	C(7)	125.4(3)
			O(3)	C(8)	C(7)	110.6(3)

Appendix C. χ_M vs. Temperature Data

$(P2OAP)_4Ni_4 \cdot 12H_2O$			$di\text{-}OAOPCu_2(BF_4)_2(H_2O)_5$		
T(K)	χ_M	esd	T(K)	χ_M	esd
2.00	4.8678E-01	2.43E-05	2.00E+00	3.5023E-02	1.50E-05
3.00	3.8720E-01	2.27E-04	3.00E+00	2.4582E-02	2.27E-05
4.00	3.2657E-01	1.10E-04	4.00E+00	1.9375E-02	8.21E-06
5.00	2.8390E-01	2.28E-04	5.00E+00	1.6243E-02	1.94E-05
6.00	2.5184E-01	2.04E-04	6.00E+00	1.4157E-02	1.24E-05
6.99	2.2663E-01	1.24E-04	7.00E+00	1.2685E-02	9.82E-06
8.00	2.0617E-01	1.08E-04	8.00E+00	1.1608E-02	5.83E-06
9.00	1.8935E-01	5.87E-05	9.00E+00	1.0789E-02	1.61E-06
10.00	1.7497E-01	5.87E-05	1.00E+01	1.0179E-02	1.58E-06
12.00	1.5166E-01	1.10E-05	1.20E+01	9.2090E-03	4.52E-08
14.00	1.3432E-01	4.61E-05	1.40E+01	8.5334E-03	9.44E-07
16.00	1.2036E-01	2.82E-05	1.60E+01	8.0061E-03	2.12E-06
18.00	1.0899E-01	2.98E-05	1.80E+01	7.5873E-03	2.66E-06
20.00	9.9580E-02	1.19E-05	2.00E+01	7.2346E-03	3.07E-06
22.00	9.1715E-02	1.26E-05	2.20E+01	6.9304E-03	2.01E-06
24.00	8.4990E-02	2.19E-05	2.40E+01	6.6582E-03	3.95E-06
26.00	7.9173E-02	1.16E-05	2.60E+01	6.4172E-03	2.36E-06
28.00	7.4119E-02	2.14E-05	2.80E+01	6.1965E-03	3.30E-06
30.00	6.9654E-02	1.04E-05	3.00E+01	5.9985E-03	1.76E-06
35.00	6.0556E-02	3.80E-05	3.50E+01	5.5783E-03	5.97E-06
40.00	5.3547E-02	1.56E-05	4.00E+01	5.2503E-03	4.73E-07
45.00	4.8002E-02	1.31E-05	4.50E+01	5.0010E-03	5.52E-06
49.99	4.3518E-02	2.06E-05	5.00E+01	4.8116E-03	5.79E-06
54.99	3.9808E-02	3.06E-05	5.50E+01	4.6327E-03	4.55E-06
60.00	3.6634E-02	3.10E-05	6.00E+01	4.4406E-03	5.12E-06
64.99	3.3882E-02	3.15E-05	6.50E+01	4.2554E-03	4.88E-06
69.99	3.1564E-02	1.21E-07	7.00E+01	4.1061E-03	3.38E-06
74.99	2.9525E-02	3.40E-05	7.50E+01	3.9818E-03	4.52E-06
79.99	2.7731E-02	4.72E-05	8.00E+01	3.8835E-03	3.33E-06
84.99	2.6133E-02	2.39E-05	8.50E+01	3.7961E-03	2.54E-06
89.99	2.4695E-02	3.03E-05	9.00E+01	3.7208E-03	2.29E-06
94.99	2.3413E-02	3.71E-05	9.50E+01	3.6394E-03	6.53E-06
99.99	2.2236E-02	2.62E-05	1.00E+02	3.5780E-03	1.14E-06
109.97	2.0235E-02	3.27E-06	1.10E+02	3.4569E-03	2.45E-06
119.98	1.8490E-02	3.00E-05	1.20E+02	3.3634E-03	1.73E-06
129.99	1.7050E-02	2.30E-05	1.30E+02	3.2676E-03	3.59E-07
139.98	1.5801E-02	7.87E-08	1.40E+02	3.1813E-03	2.64E-06
149.98	1.4741E-02	2.05E-05	1.50E+02	3.1076E-03	1.40E-06
159.98	1.3773E-02	2.26E-05	1.60E+02	3.0433E-03	7.79E-07
169.98	1.2933E-02	2.11E-05	1.70E+02	2.9749E-03	3.34E-06
179.98	1.2212E-02	1.47E-05	1.80E+02	2.9180E-03	3.70E-06
189.97	1.1509E-02	1.62E-05	1.90E+02	2.8619E-03	1.42E-06

199.98	1.1037E-02	1.65E-05	2.00E+02	2.8141E-03	3.04E-06
219.97	1.0047E-02	1.72E-05	2.20E+02	2.7159E-03	2.20E-06
239.97	9.2119E-03	7.05E-07	2.40E+02	2.6293E-03	2.14E-06
259.98	8.4527E-03	6.79E-06	2.60E+02	2.5478E-03	3.94E-07
279.99	7.8285E-03	5.91E-06	2.80E+02	2.4770E-03	4.75E-07
299.99	7.3698E-03	6.55E-06	3.00E+02	2.3948E-03	8.71E-07

$(di\text{-}OAOPNi\cdot 2.5H_2O)_n$ $[(Cl2POAP)_6Fe_9](ClO_4)_8\cdot 23H_2O$

T(K)	χ_M	esd	T(K)	χ_M	esd
1.99	8.9251E-01	3.42E-05	2.00	8.4522E+00	2.28E-02
3.00	9.9253E-01	4.19E-05	3.00	6.2763E+00	2.22E-02
4.00	9.8800E-01	3.57E-05	4.01	4.9486E+00	6.67E-03
5.00	1.1419E+00	7.27E-04	5.00	4.0874E+00	8.18E-03
6.00	1.5799E+00	2.12E-03	6.00	3.4896E+00	1.31E-02
7.00	2.0355E+00	8.57E-04	7.00	3.0404E+00	6.06E-03
8.00	2.2479E+00	3.68E-04	8.00	2.6632E+00	4.12E-03
9.00	2.3243E+00	8.12E-05	9.00	2.3679E+00	3.30E-03
10.00	2.3344E+00	3.04E-04	10.00	2.1182E+00	1.33E-04
12.00	2.2397E+00	2.25E-04	12.00	1.7336E+00	6.29E-03
14.00	2.0053E+00	2.92E-04	14.00	1.4802E+00	6.50E-03
16.00	1.5025E+00	4.58E-04	16.00	1.2683E+00	2.92E-03
18.00	8.5112E-01	3.35E-04	18.00	1.1022E+00	1.14E-03
20.00	4.7809E-01	2.29E-04	20.00	9.6682E-01	8.01E-04
22.00	3.1335E-01	5.73E-05	22.00	8.5665E-01	3.04E-04
24.00	2.2852E-01	3.21E-05	24.00	7.6658E-01	1.05E-04
26.00	1.7759E-01	5.11E-05	26.00	6.9239E-01	5.04E-05
28.00	1.4384E-01	1.98E-06	28.00	6.3052E-01	3.55E-04
30.00	1.1995E-01	4.05E-05	30.00	5.7845E-01	2.46E-04
35.00	8.2996E-02	2.85E-05	35.00	4.8131E-01	1.57E-04
40.00	6.2380E-02	1.16E-06	40.00	4.1368E-01	5.73E-04
45.00	4.9484E-02	3.29E-05	45.00	3.6485E-01	2.62E-04
50.00	4.0767E-02	3.88E-05	50.00	3.2864E-01	2.39E-04
55.00	3.4438E-02	1.17E-06	55.00	3.0078E-01	1.65E-06
60.00	2.9787E-02	3.37E-05	60.00	2.7891E-01	5.49E-05
65.00	2.6227E-02	3.60E-05	65.00	2.6132E-01	1.57E-05
69.99	2.3435E-02	3.20E-05	69.99	2.4634E-01	6.41E-05
75.00	2.1201E-02	3.05E-05	75.00	2.3348E-01	2.04E-04
79.99	1.9380E-02	2.68E-05	80.00	2.2254E-01	1.91E-04
85.00	1.7848E-02	2.55E-05	85.00	2.1303E-01	3.02E-05
89.98	1.6533E-02	6.44E-06	90.00	2.0466E-01	3.91E-05
94.99	1.5454E-02	2.34E-05	95.00	1.9709E-01	1.14E-04
99.99	1.4494E-02	2.35E-05	99.98	1.9019E-01	5.45E-06
109.98	1.2869E-02	1.51E-05	109.99	1.7854E-01	1.25E-04

119.99	1.1623E-02	1.52E-05	119.99	1.6819E-01	1.01E-04
129.98	1.0610E-02	1.14E-05	129.99	1.5926E-01	6.16E-05
139.98	9.7888E-03	1.09E-05	139.98	1.5138E-01	8.82E-06
149.98	9.0786E-03	1.02E-05	149.98	1.4472E-01	7.14E-05
159.98	8.4861E-03	1.08E-05	159.98	1.3823E-01	9.02E-05
169.98	7.9876E-03	1.27E-05	169.98	1.3254E-01	8.60E-05
179.98	7.5351E-03	7.56E-06	179.98	1.2748E-01	7.69E-05
189.97	7.1643E-03	3.13E-06	189.98	1.2257E-01	5.76E-05
199.98	6.8268E-03	8.70E-06	199.98	1.1820E-01	6.92E-05
219.97	6.2452E-03	7.03E-06	219.97	1.1048E-01	8.82E-05
239.98	5.7839E-03	7.14E-06	239.98	1.0389E-01	8.78E-05
259.98	5.3955E-03	4.75E-06	259.99	9.8268E-02	1.94E-05
279.99	5.0774E-03	4.81E-06	279.99	9.2834E-02	2.94E-05
299.99	4.7586E-03	8.16E-09	299.99	8.7292E-02	5.53E-07

References

1. Thompson, L. K.; Xu, Z.; Matthews, C. J.; Miller, D. O.; Goeta, A. E.; Wilson, C.; Howard, J. A. K.; Ohba, M.; Ōkawa, H., *J. Chem. Soc., Dalton Trans.*, **2000**, 69-77.

2. Thompson, L. K.; Matthews, C. J.; Avery, K.; Xu, Z.; Zhao, L.; Miller, D. O.; Biradha, K.; Poirier, K.; Zaworotko, M. J.; Wilson, C.; Goeta, A. E.; Howard, J. A. K., *J. Chem. Soc., Dalton Trans.*, **2001**, 1706-1710.

3. Thompson, L. K.; Matthews, C. J.; Avery, K.; Xu, Z.; Zhao, L.; Miller, D. O.; Birhadha, K.; Poirier, K.; Zaworotko, M. J.; Wilson, C.; Goeta, A. E.; Howard, J. A. K., *Inorg. Chem.* **1999**, *38*, 5266-5276.

4. Xu, Z.; Thompson, L. K.; Matthews, C. J.; Miller, D. O.; Goeta, A. E.; Howard, J. A. K., *Inorg. Chem.* **2001**, *40*, 2446-2449.

5. Thompson, L. K.; Tandon, S. S.; Manuel, M. E., *Inorg. Chem.*, **1995**, *34*, 2356.

6. Xu, Z., *Ph. D. Thesis*, Memorial University of Newfoundland, 1998.

7. (a) Stratton, W. J.; Busch, D. H., *J. Am. Chem. Soc.*, **1960**, *82*, 4834, (b) Stratton, W. J.; Busch, D. H., *J. Am. Chem. Soc.*, **1958**, *80*, 1286, (c) Stratton, W. J.; Busch, D. H., *J. Am. Chem. Soc.*, **1958**, *80*, 3191.

8. Stratton, W. J.; Ogren, P. J., *Inorg. Chem.*, **1970**, *9*, 2588.

9. Boyd, P. D. W.; Gerloch, M.; Sheldrick, G. M., *J. Chem. Soc., Dalton Trans.*, **1974**, 1097.

10. Saroja, J.; Manivanan, PV.; Chakraborty, P.; Pal, S., *Inorg. Chem.*, **1995**, *34*, 3099.

11. O'Connor, C. J.; Romananch, R. J.; Robertson, D. M.; Eduok, E. E.; Fronczek, F. R., *Inorg. Chem.*, **1983**, *22*, 449.

12. Woon, T. C.; Thompson, L. K.; Robichaud, R., *Inorg. Chem. Acta.*, **1984**, *90*, 201.

13. Souza, P.; Matesanz, A. I.; Fernández, *J. Chem. Soc., Dalton Trans.*, **1996**, 11.

14. García-Jojal, J.; García-Jaca, J.; Cortés, R.; Rojo, T.; Urtiaga, M. K.; Arriortua, M. I., *Inorg. Chem. Acta.*, **1996**, *249*, 25.

15. Ainscough, E. W.; Brodie, A. M.; Ranford, J. D.; Waters, J. M., *Inorg. Chim. Acta,* **1995**, *236*, 83.

16. Chen, X.; Zhan, S.; Hu, C.; Meng, Q.; Liu, Y., *J. Chem. Soc., Dalton Trans.*, **1997**, 245.

17. Van Koningbruggen, P. J.; Muller, E.; Haasnoot, J. G.; Reedijk, J., *Inorg. Chim. Acta,* **1993**, *203*, 37.

18. Xu, Z.; Thompson, L. K.; Miller, D. O., *Inorg. Chem.*, **1997**, *36*, 3985.

19. Thompson, L. K.; Xu, Z.; Goeta, A. E.; Howard, J. A. K.; Clase, H. J.; Miller, D. O., *Inorg. Chem.*, **1998**, *37*, 3215.

20. Xu, Z.; Thompson, L. K.; Matthews, C. J.; Miller, D. O.; Goeta, A. E.; Wilson, C.; Howard, J. A. K.; Ohba, M.; Okawa, H., *J. Chem. Soc., Dalton trans.*, **2000**, 69.

21. Matthews, C. J.; Xu, Z.; Mandal, S.; Thompson, L. K.; Biradha, K.; Poirier, K.; Zaworotko, M. J., *Chem. Commun.*, **1999**, 347-348.

22. Zhao, L; Matthews, C. J.; Thompson, L. K.; Heath, S. L., *Chem. Commun.*, **2000**, 265-266.

23. Zhao, L.; Xu, Z.; Thompson, L.K.; Heath, S. L.; Miller, D. O.; Ohba, M., *Angew. Chem. Int. Ed.*, **2000**, *39*, 3114.

24. Baxter, P. N. W.; Lehn, J-. M.; Fischer, J.; Youinou, M-. T., *Angew. Chem.*, **1994**, *33*, **22**, 2284.

25. Lehn, J. –M., *Chem. Eur. J.*, **1999**, *5*, **6**, 1803.

26. J. –M. Lehn, Supramolecular Chemistry – Concepts and Perspectives, VCH, Weinheim, **1995**.

27. Baxter, P. N. W.; Lehn, J-. M.; Kneisel, B. O.; Fenske, D., *Angew. Chem.*. **1997**, *36*, **18**, 1978.

28. Rojo, J.; Lehn, J-. M.; Baum, G.; Fenske, D.; Waldman, O.; Müller, P., *Eur. J. Inorg. Chem.*, **1999**, 517.

29. Fujita, M.; Kwon, Y. J.; Washizu, S.; Ogura, K., *J. Am. Chem. Soc.*, **1994**, *116*, 1151.

30. Stang, P. J.; Olenyuk, B., *Angew. Chem. Int. Ed.*, **1995**, *35, 372.*

31. Drain, C. M.; Lehn, J. –M., *J. Chem. Soc., Chem. Commun.*, **1994**, *116*, 616.

32. Holger, Hillgeris, E. C.; Erxleben, A.; Lippert, B., *J. Am. Chem. Soc.*, **1994**, *116*, 616.

33. Stang, P. J.; Chen, K., *J. Am. Chem. Soc.*, **1995**, *117*, 1667.

34. Youinou, M. –T.; Nahmouni, N.; Fischer, J.; Osborn, J. A., *Angew. Chem. Int. Ed.*, **1992**, *31*, 733.

35. Rojo, J.; Romero-Salguero, F. J.; Lehn, J. –M.; Baum, G.; Fenske, D., *Eur. J. Inorg. Chem.* **1999**, 1421.

36. Hanan, G. S.; Volkmer, D.; Ulrich, S. S.; Lehn, J. –M.; Baum, G.; Fenske, D., *Angew. Chem. int. Ed.*, **1997**, *36*, 1842.

37. Mann, K. L. V.; Psillakis, E.; Jeffery, J. C.; Rees, L. H.; Harden, N. M.; McCleverty, J. A.; Ward, M. D.; Gatteschi, D.; Totti, F.; Mabbs, F. E.; McInnes, E. J. L.; Riedi, P. C.; Smith, G. M., *J. Chem. Soc., Dalton Trans.*, **1999**, 339.

38. Campos-Fernández, C. S.; Clérac, R.; Dunbar, K. R., *Angew. Chem. Int. Ed.*, **1999**, *38*, **23**, 3477.

39. Bu, X. –H.; Morishita, H.; Tanaka, K; Biradha, K.; Furusho, S.; Shionoya, M., *Chem. Comm.*, **2000**, 971.

40. Gelasco, A.; Askenas, A.; Percoraro, V. L., *Inorg. Chem.*, **1996**, *35*, 1419

41. Duan, C. –Y.; Liu, Z. –H.; You, X. –Z.; Xue, F.; Mak, T. C. W., *Chem. Commun.*, **1997**, 381.

42. Murray, K.S. *Advances in Inorganic Chemistry*, **1995**, *43*, 261-358 and references therein.

43. Piguet, C.; Bemardinelle, G.; Hopfgartner, G., *Chem. Rev.*, **1997**, *97*, 2005 and references thereis.

44. Parsons, W.; Winpenny, R. E. P., *Acc. Chem. Res.*, **1997**, *30*, 89.

45. For instance see: Sessoli, R. C.; Tsai, H-. L.; Schake, H. R.; Wang, S.; Vincent, J. B.; Folting, K.; Gatteschi, D.; Christou, G.; Hendrickson, D. N., *J. Am. Chem. Soc.*, **1993**, *115*, 1804.

46. Müller, A., Krickemeyer, E.; Meyer, J.; Bögge, H.; Peters, F.; Plass, W.; Diemann, E.; Dillinger, S.; Nonnenbruch, F.; Randerath, M.; Menke, C., *Angew. Chem. Int. Ed. Engl.*, **1995**, *34*, 2122.

47. Kahn, O., Molecular Magnetism, VCH Publishers Inc., **1993**.

48. Miller, J. S.; Calabrese, J. C.; Epstien, A. J.; Bigelow, R. W.; Zhang, J. H.; Reiff, W. M., *Chem Commun.*, **1986**, 1026,

49. Pei, Y; Verdaguer, M. V.; Kahn, O; Slatten, J.; Renard, J. -P., *J. Am. Chem. Soc.*, **1986**, *108*, **23**, 7428.

50. Verdaguer, M. V., Bleuzen, A.; Train, C.; Garde, R.; Fabrizi De Biani, F.; Desplanches, C., *Phil. Trans. R. Soc. Lond. A*, **1999**, *357*, 2959-2976.

51. Caneschi, A.; Gatteschi, D.; Sessoli, R.; Barra, A. –L.; Brunel, L. C.; Guillot, M., *J. Am. Chem. Soc.*, **1991**, *113*, 5873.

52. Lehn, J. –M, Möller, M.; Semenov, A.; Sbatz, J. P.; Sell, B.; Schubert, D.; Weidl, C. H.; Schubert, U. S., *Angew. Chem. Int. Ed.*, **1999**, *38*, 17, 2547.

53. SIR92: Altomare, A.; Cascarano, M.; Giacovazzo, C.; Guagliardi, A., *J. Appl. Cryst.*, **1993**, *26*, 343.

54. DIRDIF94: Beurskens, P. T.; Admiraal, G.; Beurskens, G.; Bosman, W. P.; de Gelder, R.; Israel, R.; Smits, J. M. M., **1994**. The DIRDIF-94 program system, Technical Report of the Crystallography Laboratory, University of Nijmegen, The Netherlands.

55. Cromer, D. T.; Waber, J. T., "International Tables for X-ray Crystallography", Vol. IV, The Kynoch Press, Birmingham, England, Table 2.2A (1974).

56. Ibers, J. A.; Hamilton, W. C.; *Acta Crystallogr.*, **1964**, *17*, 781.

57. Creagh, D. C.; McAuley, W. J., "International Tables for Crystallography", Vol C, (A. J. C. Wilson, ed.), Kluwer Academic Publishers, Boston, Table 4.2.6.8, 219-222 (1992).

58. teXsan for Windows version 1.06: Crystal Structure Analysis Package, Molecular Structure Corporation (1997-9).

59. SHELX97: Sheldrick, G. M. (1997).

60. Mössbauer, R. L.; *Z. Physik,* **1958**, *151*, 124.

61. Kwak, B.; Rhee, H.; Park, S.; Lah, M. S., *Inorg. Chem.*, **1998**, *37*, 3599-3602.

62. Liu., S. –l.; Lin, S.; Lin, B. Z.; Lin, C. –C.; Huang, J. Q., *Angew. Chem. Int. Ed.*, **2001**, *40*, 1084-1087.

63. Langrenée, M.; Sueur, S.; Wignacourt, *Acta Crystallogr.*, **1991**, *C47*, 1158-1160.

64. Castle, R. N. (ed.), "PYRIDAZINES" An Interscience Publication, J. Wiley and Sons Inc., 1973.

65. Waldman, O.; Koch, R.; Schromm, S.; Müller, P.; Zhao, L.; Thompson, L. K.; *Chem. Phys. Lett.*, **2000**, *332*,73.

66. Zhao, L.; Xu, Z.; Thompson, L. K.; Miller, D. O.; *Polyhedron,* **2001**, *20*, 1359.

67. Belicchi Ferrari, M., *Inorg. Chim. Acta.*, **1994**, *223*, 77.

68. Parsons, S., unpublished results.

69. Thompson, L. K.; Xu, Z.; Miller, D. O.; Clase, H. J.; Howard, J. A. K.; Goeta, A. E., *Inorg. Chem.*, **1998**, *37*, 3620.

70. Thompson, L. K.; Zhao, L.; Xu, Z.; Miller, D. O.; Reiff, W. M., *Inorg. Chem.*, **2003**, *42*, 128-139.

71. Sakamoto, M.; Itose, S.; Ishimori, T., *J. Chem. Soc. Dalton Trans.*, **1989**, 2083.

72. Lever, A. B. P., Inorganic Electronic Spectroscopy, Elsevier Publishing Company, 1968.

73. Thompson, L. K.; Nanda, K. K.; Bridson, J. N.; Nag, K., *Chem. Comm.*, **1994**, 1337.

74. Rouba, S.; Rabu, P.; Ressouche, E.; Regnault, L. –P.; Drillon, M., *Journal of Magnetism and Magnetic Materials*, **1996**, *163*, 365-372.

75. Baldwin, M. J.; Kampf, J. W.; Kirk, M. L.; Pecoraro, V. L., *Inorg. Chem.*, **1995**, *34*, 5252.

76. Lloret, F.; Ruiz, R.; Julve, M.; Faus, J.; Journaux, Y.; Castro, I.; Verdaguer, M., *Chem. Mater.*, **1992**, *4*, 1150.

77. Caneshi, A.; Gatteschi, D.; Melandri, M. C.; Rey, P.; Sessoli, R., *Inorg. Chem.*, **1990**, *29*, 4228.

78. ISOPRO, Version 3.0, by Senko, M., (http://members.aol.com/msmssoft)

79. Greenwood, N. N.; Gibb, T. C., Mössbauer Spectroscopy, Chapman and Hall: London, **1971**.

80. Xu, Z.; Thompson, L. K.; Miller, D. O., *Chem. Commun.*, **2001**, 1170-1171.

81. Milway, V.; Niel, V.; Xu, Z.; Thompson, L. K.; Grove, H.; Miller, D. O.; Parsons, S. R., Octa-nuclear and

nona-nuclear copper(II) complexes with linear 'tritopic' ligands - structural and magnetic studies., *Inorg. Chem.*; Awaiting Publication.

82. Xu, Z.;Thompson, L. K.; Miller, D. O.; Clase, H. J.; Howard, J. A. K.; Goeta, A. E., *Inorg. Chem.*, **1998**, *37*, 3620.

83. Kambe, K., *J. Phys. Soc., Japan*, **1950**, *5*, 48.

84. Martin, R. L., in "New Pathways in Inorganic Chemistry", Eds. E. A. V. Ebsworth, A. G. Maddock, A. G. Sharpe, Cambridge Univ. Press, **1968**, 175.

85. Program ow01.exe, Version 19.6.00, by Oliver Waldman, 2000.

86. MAGMUN, Version 2.0, by Xu,; Z., 2001. (http://www.ucs.mun.ca/~lthomp)